Numerical solution of linear transport equations with scattering operators of integral and differential type

by

Kevin Gregory Phillips

B.S. Rutgers University, 2003

M.A. The City College of New York, 2006

A dissertation submitted to the Graduate Faculty in Physics in partial fulfillment of the requirements for the degree of Doctor of Philosophy,

The City University of New York

2008

This manuscript has been read and accepted for the
Graduate Faculty in Physics in satisfaction of the
dissertation requirement for the degree of Doctor of Philosophy.

Dr. Carlo Lancellotti

Date — Chair of Examining Committee

Dr. Sultan Catto

Date — Executive Officer

Dr. Andrew Poje

Dr. Tobias Shaefer

Dr. William Schreiber

Dr. Min Xu

Supervisory Committee

The City University of New York

Abstract

Numerical solution of linear transport equations with scattering operators of integral and differential type

by

Kevin G. Phillips

Advisor: Professor Carlo Lancellotti

We revisit the P_N-method and demonstrate its ability to provide accurate and timely solutions to transport equations with scattering operators whose only restriction is having spherical harmonics as eigenfunctions. Such operators include the integral scattering operator characterized by a scattering kernel and forward-scattering approximations thereto involving functions of the Laplacian restricted to the unit sphere. Solutions obtained with the P_N-method are shown to converge exponentially as the number, N, of Legendre polynomials used to approximate the solution is increased. The computation time is shown to grow slowly with increased number of polynomials used. Moreover the solution technique is shown to be stable as N increases. The primary result of this work is the use of the P_N-method to carry out prompt side-by-side comparisons of radiative transport equations with different tissue-light interactions. Comment is made on the ability of the forward-scattering approximations to describe the transport properties of light in biological media as determined by the radiative transfer equation with Henyey-Greenstein phase function.

Dedication

To my WONDERFUL! family

Acknowledgements

I would like to thank Dr. Carlo Lancellotti for being a very kind, understanding, supportive and flexible dissertation advisor. Your level-headed mentorship and friendliness is an inspiration. I am indebted to Dr. William Schreiber for facilitating my transition to the College of Staten Island. I would also like to the thank Dr. Gayen, Dr. Alfano and especially Dr. Min Xu for getting me started in radiative transport theory during our work together at City College. I thank Dr. Timothy Boyer for guidance in the early stages of my graduate career and for teaching the best classes I have ever attended in my time as a student. Thanks to Dr. Poje and Dr. Schaefer for helpful discussions along the way.

I thank my parents Donna, Lance, Arend-Jan, and Ann who convinced me on a continual basis to keep going with my studies. You all provided me more hope and inspiration than you know!

A very special thanks to Donna and A.J. for subsidizing my trip to Photonics West 2006 and for flying me home in the Spring of 2008 to finish off my research. These contributions were pivotal in my career and scientific development, thank you so much! In addition, I extend a special thanks to Lance, Ann, and Elaine who provided copious amounts of advice and support via phone and in person be it in NJ, AR, MO, OR. Thanks as well for helping facilitate the early planning of the move out west. Thanks to Ann for the cereal-filled care packages that helped fuel the early stages of my writing. Thanks most of all to Owl Software for the shiny laptop upon which the final pages of this dissertation were written!

I thank my grandparents Twilah June, Rex, June and Jim-Bill and my extended family (be they blood relatives or contractually obligated) for their encouragement and love.

I also extend a very special thanks to my in-laws who took me into their home (along with their daughter) where they fed me, provided me many kWh of electricity and Internet access during my year long stay. Thank you for your love and support in all aspects of my life. Thanks to Grandma "A" for all of the great food and love. Hopefully the facts presented here are as robust (abundanza!) as your sausage rolls at super-bowl time. And a special thanks to Aunt Donna and Uncle Donald for all the wonderful food and good times spent on the boat and in the best of the best restaurants around NJ and NYC.

I must also acknowledge the wonderful friendship of my classmates Jia-ju Ma, Sébastien Cormier, Henry Stzul and Sean McHugh- you guys made graduate life a joy, even on the tough days! If only we could be as good at Physics as we are at playing ping pong, drinking beer, eating at Golden Great Wall, etc.

And lastly, April. Thank you for paying the rent and supporting me emotionally during my ups and (more prevalent) downs over the course of my studies!

Contents

Chapter

1 Introduction 1

2 Derivation of the Radiative Transfer Equation 7

2.1 Basic Definitions 7

2.2 Particle Conservation in an Arbitrary Volume 11

2.3 Specialization to Plane-Parallel Geometries 14

2.3.1 RTE for Infinite Plane-Wave Illumination of a Half-Space . 15

2.4 Fluence and Flux 15

2.5 Characteristic Length Scales and the Diffusion Approximation . . 17

2.5.1 Scattering and Transport Mean Free Path 17

2.5.2 The Diffusion Approximation 18

2.6 Summary 20

3 Forward Scattering Approximations of the Radiative Transfer Equation: Generalized Fokker-Planck Equations 22

3.1 The Case for Forward Scattering Approximations 22

3.2 What are generalized Fokker-Planck equations? 24

3.3 Approximating the spectrum of the integral scattering operator . 25

3.3.1 High order Fokker-Planck operators 27

3.3.2 The standard Fokker-Planck equation 28

3.3.3 A standard Fokker-Planck operator in combination with a pseudo-differential operator 29
3.3.4 The modified Leakeas-Larsen equation 30
3.3.5 The second modified Leakeas-Larsen equation 31
3.4 Comparison of scattering operator spectra 32
3.5 Summary 41

4 The P_N-Method 42
4.1 Introduction to Spectral Methods 42
4.2 The Galerkin Spectral Method in Detail 44
4.3 P_N-Method Applied to the General Transport Problem 47
4.3.1 Normal mode expansion in z 48
4.3.2 Expansion in (spherical harmonics) Legendre polynomials . 48
4.3.3 Imposing boundary conditions 50
4.3.4 Summary of the P_N-method: Numerical Procedure 51
4.4 Summary 52

5 Convergence Properties of the P_N-method 54
5.1 Introduction 54
5.2 Definition of the Relative Error 54
5.3 Convergence of the Relative Error in Truncation Order, n 56
5.4 Dependence of the Relative Error Convergence on Anisotropy Factor, g 61
5.5 Optimal Truncation Order, n^*, for each g 80
5.6 Computation Time 80
5.7 Condition Number of Boundary Condition Matrix 86
5.7.1 Definition of the Condition Number 88
5.8 Summary 89

6 Accuracy of Generalized Fokker-Planck Equations in Tissue Optics 92

6.1 Introduction 92

6.2 Solutions: Backscattered and Transmitted Radiance 92

6.3 L_2-Error of RTE and GFPE Solutions: Radiance 93

6.4 Relative Error of RTE and GFPE Solutions: Surface Currents . . 104

6.5 Solutions: Depth-dependent Fluence 109

6.6 L_2-Error of RTE and GFPE Solutions: Fluence 109

6.7 Summary 118

7 Summary and Outlook 121

Appendix

A Incompatibility of the Henyey-Greenstein phase function and Fokker-Planck equations 123

B Derivation of the eigenvalue relation $\mathcal{L}_{3/2}Y_{nm}(\omega) = -nY_{nm}(\omega)$ 125

C `OneDrtePn.m`: A Matlab M-file Implementation of the P_N-method 127

Bibliography 133

Tables

Table

5.1 Reflected Flux: Convergence rate, α, with 95% confidence bounds, of the exponential decay of the relative error. The value n denotes the point at which the convergence rate becomes sub-exponential. 60

5.2 Transmitted Flux: Convergence rate, α, with 95% confidence bounds, of the exponential decay of the relative error. The value n denotes the point at which the convergence rate becomes sub-exponential. 60

Figures

Figure

2.1 Representative Phase Functions 10

2.2 Particle Conservation in an Arbitrary Volume 12

2.3 Plane-Parallel Geometry 16

3.1 Comparison of GFP and RTE spectra for $g = 0.9$, $\sigma_s = 100$ cm^{-1}. 34

3.2 Error in GFP Spectra, $N = 10$. 35

3.3 Error in GFP Spectra, $N = 20$. 36

3.4 Error in GFP Spectra, $N = 50$. 37

3.5 Error in GFP Spectra, $N = 100$. 38

3.6 Error in HOFP Spectra, $N = 10$, 15, 20, 30. 39

5.1 Fitting for the Convergence Rate of the Relative Error of RTE Transmitted Current, for g=0.9 59

5.21 Convergence of F.P. + $\mathcal{L}_{3/2}$ Transmitted Current vs. g, for $N = 20, 40, 60, 80$. 61

5.2 Convergence of the RTE Reflected Current vs. N, for $g = 0.9$, 0.99, 0.999 62

5.3 Convergence of the RTE Transmitted Current vs. N, for $g = 0.9$, 0.99, 0.999 63

5.4 Convergence of the standard Fokker-Planck Reflected Current vs. N, for $g = 0.9, 0.99, 0.999$ 64
5.5 Convergence of the standard Fokker-Planck Transmitted Current vs. N, for $g = 0.9, 0.99, 0.999$ 65
5.6 Convergence of the Modified Leakeas-Larsen Reflected Current vs. N, for $g = 0.9, 0.99, 0.999$ 66
5.7 Convergence of the Modified Leakeas-Larsen Transmitted Current vs. N, for $g = 0.9, 0.99, 0.999$ 67
5.8 Convergence of the Second Modified Leakeas-Larsen Reflected Current vs. N, for $g = 0.9, 0.99, 0.999$ 68
5.9 Convergence of the Second Modified Leakeas-Larsen Transmitted Current vs. N, for $g = 0.9, 0.99, 0.999$ 69
5.10 Convergence of the Fokker-Planck + $\mathcal{L}_{3/2}$ Reflected Current vs. N, for $g = 0.9, 0.99, 0.999$ 70
5.11 Convergence of the Fokker-Planck + $\mathcal{L}_{3/2}$ Transmitted Current vs. N, for $g = 0.9, 0.99, 0.999$ 71
5.12 Convergence of the RTE Reflected Current vs. g, for $N = 20, 40, 60, 80$. 72
5.13 Convergence of the RTE Transmitted Current vs. g, for $N = 20, 40, 60, 80$. 73
5.14 Convergence of the standard Fokker-Planck Reflected Current vs. g, for $N = 20, 40, 60, 80$. 74
5.15 Convergence of the standard Fokker-Planck Transmitted Current vs. g, for $N = 20, 40, 60, 80$. 75
5.16 Convergence of the Modified Leakeas-Larsen Reflected Current vs. g, for $N = 20, 40, 60, 80$. 76
5.17 Convergence of the Modified Leakeas-Larsen Transmitted Current vs. g, for $N = 20, 40, 60, 80$. 77

5.18 Convergence of the Second Modified Leakeas-Larsen Reflected Current vs. g, for $N = 20, 40, 60, 80$. 78

5.19 Convergence of the Second Modified Leakeas-Larsen Transmitted Current vs. g, for $N = 20, 40, 60, 80$. 79

5.22 Optimal Truncation Order, n^*, of the RTE Determined for $g \in [0.7, 0.99]$ 81

5.23 Optimal Truncation Order, n^*, of the Fokker-Planck Equation Determined for $g \in [0.7, 0.99]$ 82

5.24 Optimal Truncation Order, n^*, of the Modified Leakeas-Larsen Equation Determined for $g \in [0.7, 0.99]$ 83

5.25 Optimal Truncation Order, n^*, of the Second Modified Leakeas-Larsen Equation Determined for $g \in [0.7, 0.99]$. 84

5.26 Optimal Truncation Order, n^*, of the Fokker-Planck + $\mathcal{L}_{3/2}$ Operator Determined for $g \in [0.98, 0.999]$. 85

5.27 Computation Times for the RTE , standard FP, and Modified Leakeas-Larsen Equations. 87

5.28 Condition Number of the Boundary Condition Coefficient Matrix. 90

6.1 Backscattered Radiance, $g = 0.7$, N = 100. 94

6.2 Backscattered Radiance, $g = 0.8$, N = 100. 95

6.3 Backscattered Radiance, $g = 0.9$, N = 100. 96

6.4 Backscattered Radiance, $g = 0.99$, N = 100. 97

6.5 Backscattered Radiance, $g = 0.999$, N = 100. 98

6.6 Transmitted Radiance, $g = 0.7$, N = 100. 99

6.7 Transmitted Radiance, $g = 0.8$, N = 100. 100

6.8 Transmitted Radiance, $g = 0.9$, N = 100. 101

6.9 Transmitted Radiance, $g = 0.99$, N = 100. 102

6.10 Transmitted Radiance, $g = 0.999$, N = 100. 103

6.11 L_2-error of the RTE and GFPE Backscattered Solutions vs. g, $N = 100$ 105

6.12 L_2-error of the RTE and GFPE Backscattered Solutions near $g = 1$, $N = 100$ 106

6.13 L_2-error of the RTE and GFPE Transmitted Solutions vs. g, $N = 100$107

6.14 L_2-error of the RTE and GFPE Transmitted Solutions near $g = 1$, $N = 100$ 108

6.15 Relative Error of the Reflected Current vs. g, $N = 100$ 110

6.16 Relative Error of the Reflected Current near $g = 1$, $N = 100$ . . . 111

6.17 Relative Error of the Transmitted Current vs. g, $N = 100$ 112

6.18 Relative Error of the Transmitted Current near $g = 1$, $N = 100$. 113

6.19 Fluence, $g = 0.7$, N = 100. 114

6.20 Fluence, $g = 0.8$, N = 100. 115

6.21 Fluence, $g = 0.9$, N = 100. 116

6.22 Fluence, $g = 0.99$, N = 100. 117

6.23 L_2-error of the Fluence vs. g, $N = 100$ 119

6.24 L_2-error of the Fluence near $g = 1$, $N = 100$ 120

Chapter 1

Introduction

The radiative transfer equation (RTE) is a linear transport equation of Boltzmann type [15] that describes the propagation of light in a scattering media on a mesoscopic scale. Depending on the specification of the underlying microscopic dynamics of light, different transport equations can be derived. Those depending on the Maxwell equations are more recent [53] and use variations of the refractive index of the background medium to describe the microscopic scattering process. In this study we shall adopt a phenomenological point of view [27, 16] in which electromagnetic wave propagation is approximated by the flow of neutral particles we refer to as photons, though no quantum or classical wave effects shall be considered. In this approximate model, photons undergo straight line motion through the scattering media until they are either absorbed or scattered into another straight line trajectory.

Scattering in this picture is determined by an *ad hoc* specification of the probability density, termed phase function in the optics literature [27], to scatter from one direction into another. The exact form of the probability density is typically derived from experiment, eg. the Henyey-Greenstein phase function [28], or heuristic arguments, eg. the exponential phase function [48]. While it may seem that a theory of mesoscopic light propagation based on first principles would be better than a phenomenological theory, we make no argument to the

contrary, the phenomenological theory is more accessible to numerical studies with computer and analytical methods with pencil and paper. Most importantly, the phenomenological RTE has been shown to accurately reproduce the intensity distributions observed in biomedical applications [18, 1, 51], the scenario in which this study rests.

Light propagation through scattering media using a transport equation based on a phenomenological viewpoint was first studied at the beginning of the twentieth century by Schuster [54]. Since that time, linear transport equations have been studied extensively in diverse fields such as neutron transport [14, 21], electronic transport in semiconductors [56], the energy density of acoustic and electromagnetic waves in random media [53], and tissue optics [58]. The present study concerns the application of the RTE to tissue optics in which non-ionizing near-infra-red (NIR) photons are used to optically probe tissues for the diagnosis of pathologies, such as cancer, and the monitoring of functional properties such as oxygenation and hemodynamics [19, 1, 24]. Our specific aim will be the prediction of backscattered and transmitted light intensities from scattering materials.

Due to the low energies of the NIR photons, scattering events with the underlying media strongly influence the trajectories of the photons. The tissue-light interaction is believed to be dominated by forward scattering in which the trajectories of the photons are changed only slightly during each scattering event. Due to the large number of such events, the collective effect of multiple scattering has drastic effects on photon propagation by essentially randomizing the photon trajectories. As a result, NIR photons provide very poor spatial resolution and are not easily used to form images like their x-ray counterparts. NIR photons can, however, distinguish absorption characteristics of tissues which other modalities, such as x-ray, cannot. Absorption characteristics of tissues are a key parameter in the non-invasive diagnosis of tissue pathologies and the monitoring of functional

properties such as oxygenation and hemodynamics [19, 1, 24]. Typically tissue health is determined by comparing transmission and backscatter of light in normal and diseased tissues. Theoretical studies of light propagation are important in aiding future diagnostic developments using NIR light. It is hoped that numerical solutions of the RTE can be used to guide experiments and clinical applications of NIR light as well as aid in the continuing endeavor to accurately describe the tissue-light interaction.

Studying NIR photon propagation numerically is a difficult task. In typical calculations, complicated tissue geometries are approximated as finite slabs: sections of scattering media with finite depth and infinite width. Both deterministic and nondeterministic studies of the RTE and linear transport models in general; primarily in neutronic applications, have been pursued vigorously since the 1940's. A simple heuristic argument [47] shows why both deterministic and nondeterministic methods are difficult to apply in practical situations: as photons propagate through a scattering media, the average distance a particle travels between scattering events, l_s, is very small, ie. $l_s \ll 1$. Each scattering event tends to change the propagation direction of the photons only slightly on the average (as mentioned earlier biological tissues scatter strongly in the forward direction), thus for any appreciable changes in the propagation direction of a photon to be observed, an $O(1)$ distance in the material must be considered. To apply deterministic numerical methods to the RTE one must consider mesh sizes on the same scale as l_s, a daunting computational task. In non-deterministic methods, such as Monte Carlo simulations, a large number of iterations updating the trajectory of scattered photons must be considered to achieve statistically stable, realistic results. These methods are widely used in spite of their inherent difficulty [60, 39, 4, 2]

To circumvent these computational problems, the time-asymptotic diffusion limit of the RTE is commonly studied [36, 20]. In this macroscopic picture, pho-

tons undergo a great many scattering events taking on a random walk behavior in the material, ie. on the scale of $O(1)$ distances. Diffusion is computationally cheaper with regard to deterministic numerical methods than the RTE. The major drawback of diffusion theory is that it fails in the presence of clear layers, embedded objects, and small source-detector separations. Adjustments to the diffusion theory in these situations has been addressed through domain decomposition methods [6, 5] in which the transport equation is coupled to the diffusion equation.

Another class of approximations to simplify the numerical treatment of the RTE consist of forward-scattering models in which the strong forward scattering of light in biological media is utilized to formulate alternatives to the integral scattering operator. The majority of such efforts have resulted in generalized Fokker-Planck equations in which differential operators in the angular variables [32] describe scattering. Roughly, these models can be said to describe diffusive behaviors in the direction space variation of the photon density. These models were first developed in the neutron and electron transport communities [47, 48, 49, 37, 38] where forward-scattering is pervasive at high energies. These models allow one to simplify the methods used for angular desensitizations of the RTE while at the same time accounting for the dominant physical behavior.

Previous deterministic studies of the RTE have centered around two different numerical schemes regarding the angular dependence of the radiance: the discrete ordinates method and the P_N-method. In the discrete ordinates method [39], the radiance is evaluated at discrete angular points in the direction space (collocation). The integral term in the RTE is evaluated through Gauss quadrature and as a result the unknowns, ie. the photon density ψ evaluated at discrete points in the direction space, are all coupled. If the integral term can be replaced with a differential operator in the direction space variables, based on some forward-

scattering approximation, then finite-differences can be brought to bear which couple at most three terms [42] . The trade off is that one obtains less computational troubles at the expense of having to develop model-specific finite-difference methods for the scattering approximation considered.

In contrast, the P_N-method treats the angular dependence of the radiance and scattering operator by approximating the exact angular dependence with a truncated sum of Legendre polynomials. The treatment of the integral scattering operator, and any scattering operator whose eigenfunctions are the spherical harmonics, leads to de-coupled expansion coefficients. Two-term coupling does occur however, as a result of the presence of the direction space variables as pre-factors to the spatial differential operators in the RTE. The P_N-method provides the same amount of coupling regardless of the scattering operator used. For this reason, the P_N-method can be used as a tool to explore different tissue-light interactions without recourse to model-specific numerical methods.

The goal of this dissertation will be the appraisal of forward-scattering models that currently exist in the transport literature by assessing their ability to provide accurate replacement of models with integral scattering operators. We do this in the slab geometry, in which a scattering media occupies a semi-infinite half space composed of discrete spherical scatterers characterized by a single-scattering phase function. Infinite plane wave illumination is considered.

The organization of the dissertation is structured as follows: in Chapter 2 the RTE is deduced by considering the conservation of photons in an arbitrary volume of scattering media, Chapter 3 presents the derivation of the Fokker-Planck and generalized Fokker-Planck type forward-scattering approximations to the RTE. In Chapter 4 a development of the P_N-method is presented for transport equations with general scattering operators whose eigenfunctions are the spherical harmonics.

In Chapter 5 the convergence of the relative error of numerical solutions obtained with the P_N-method is investigated. The presentation highlights the ability of the P_N-method to obtain converged solutions in the presence of anisotropy for each of the forward scattering operators considered in Chapter 3. In Chapter 6 numerical results for the infinite plane wave illumination of a semi-infinite slab are presented. The forward-scattering models are compared to the integral scattering operator with Henyey-Greenstein phase function in predicting: steady-state angularly resolved backscatter and transmitted radiance, backscattered and transmitted flux, and depth-dependent fluence. We conclude in Chapter 7 with a summary of the main results along with an outlook for future work.

Chapter 2

Derivation of the Radiative Transfer Equation

2.1 Basic Definitions

Radiative transport theory provides a mesoscopic description of multiply scattered light propagating in a random media using a linear Boltzmann-type equation for the specific intensity. The specific intensity, also called the radiance, is a fundamental quantity in tissue optics and is defined as the radiant power per unit of solid angle about a unit direction vector ω and per unit area perpendicular to ω. The specific intensity is denoted by $I(t, \omega, \mathbf{r})$ where $t \in (0, \infty)$ is the time, $\mathbf{r} \in R^3$ is the spatial position, and $\omega \in S^2$ is the direction of propagation. The units of radiance are watts per meter squared per steradian (units of solid angle). To aid in the development of the RTE through particle conservation arguments the correspondence between the density of photons and the radiance is introduced.

The density of photons, $\psi(t, \omega, \mathbf{r})$, is the number of photons in the volume element d$\mathbf{r}$ about $\mathbf{r}$ whose propagation directions lay in the solid angle dω about ω at time t. Assuming the photons propagate with frequency ν, assumed to be unchanged during scattering events with the underlying media, the radiance and photon density are related through:

$$I(t, \omega, \mathbf{r}, \nu) = ch\nu\psi(t, \omega, \mathbf{r}, \nu), \tag{2.1}$$

where c is the speed of light in vacuum and h is Planck's constant. A transport

equation for the density will be developed in the following section.

The interaction of light with the underlying media is modeled through three mechanisms: streaming, absorption, and scattering. In radiative transfer theory, light is treated as a stream of non-interacting photons (quantum effects are assumed negligible) that travel along straight lines until they are either scattered (with no change in frequency) or absorbed by the underlying material (resulting in heating).

The absorption cross section, $\sigma_a(t, \mathbf{r})$, defines the probability, p_a, that in traveling a distance $\mathrm{d}s$, a particle will be absorbed

$$p_a = \sigma_a(t, \mathbf{r})\mathrm{d}s. \tag{2.2}$$

Similarly, in traveling a distance $\mathrm{d}s$ particles have a probability, p_s, of being scattered given in terms of the scattering cross section, σ_s, by

$$p_s = \sigma_s(t, \mathbf{r})\mathrm{d}s. \tag{2.3}$$

In both definitions, the cross sections have dimensions inverse length and are assumed to be independent of any directional dependence on ω. This implies that the interaction of photons with the underlying material is isotropic- photons interact in the same way with the material regardless of their propagation direction. As well, we assume that the spatial and temporal variations of the cross sections are sufficiently small so as to treat these interaction coefficients as constants independent of $(t, \mathbf{r})$.

The scattering cross section can be further defined in terms of the scattering kernel, $f(\omega \cdot \omega')$, also known as the phase function, which expresses the probability density that in traveling a distance $\mathrm{d}s$ a photon with propagation direction ω' before the collision scatters into the direction ω after the collision. Because it is a probability density, the phase function is a non-negative function of its argument

and is normalized to either one or σ_s. In most theoretical discussions, the phase function is taken to depend only on the cosine, $\omega \cdot \omega'$, of the scattering angle as opposed to depending on ω and ω' separately. This is a result of the isotropic, in space, nature of the scattering material taken to be composed of spherical, on average, medium constituents. Throughout we normalize the phase function to σ_s such that

$$\sigma_s = \int_{S^2} f(\omega \cdot \omega') \mathrm{d}(\omega \cdot \omega'). \tag{2.4}$$

The scattering process determined by the phase function can be characterized by the anisotropy factor, g, defined as the average cosine of the scattering angle for each scattering event. g has the following definition

$$g = 2\pi \int_{-1}^{1} (\omega \cdot \omega') f(\omega \cdot \omega') \mathrm{d}(\omega \cdot \omega'). \tag{2.5}$$

g ranges from zero, for isotropic scattering, to 1, for completely forward scattering. In biological media the anisotropy factor ranges [17] from 0.7 to 0.95.

The phase function is specified based on either empirical grounds, as in the case of widely used Henyey-Greenstein phase function [28],

$$f_{\mathrm{HG}}(\omega \cdot \omega') = \frac{\sigma_s (1 - g^2)}{4\pi (1 - 2g(\omega \cdot \omega') + g^2)^{3/2}}, \tag{2.6}$$

or on physical arguments [35] as in the case of the exponential phase function,

$$f_{\exp}(\omega \cdot \omega') = \frac{\sigma_s}{2\pi\epsilon} \frac{\exp(-(1 - (\omega \cdot \omega'))/\epsilon)}{1 - \exp(-2/\epsilon)}. \tag{2.7}$$

The parameter ϵ is related to the anisotropy factor through [35] $g = \coth(\epsilon^{-1}) - \epsilon$. For reference, the isotropic phase function $f_{\mathrm{iso}}(\omega \cdot \omega') = \sigma_s / 4\pi$, Henyey Greenstein, and exponential phase functions are plotted on a semi-log scale in Figure 2.1.

A glaring omission from the above definitions of the scattering and absorption coefficients in the context of tissue optics is their non-trivial frequency dependence. It is well known that different cell structures scatter light differently depending upon the frequency of the illuminating beam. The underlying

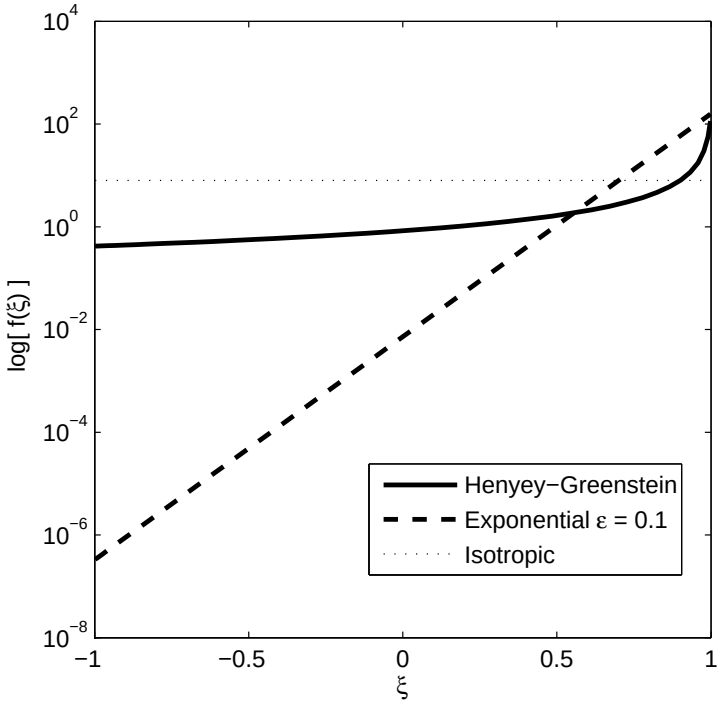

Figure 2.1: Plot of exponential, Henyey-Greenstein and isotropic phase functions for $g = 0.9$ ($\epsilon = 0.1$) and $\sigma_s = 100[\text{cm}^{-1}]$. Here $\xi = \omega \cdot \omega'$. The isotropic phase function treats all scattering angles with the same likelihood of occurrence while the Henyey-Greenstein and exponential phase functions favor forward scattering. The exponential phase function severely limits the possibility of large angle scattering events near $\xi = -1$.

assumption regarding frequency dependence that will pervade the remaining discussion is that light illumination and detection takes place at the same frequency and that scattering events are elastic in that they do not change the frequency of the propagating light. Hence our discussion is limited to monochromatic light propagation.

2.2 Particle Conservation in an Arbitrary Volume

We now employ the assumptions of the previous section concerning the basic mechanisms that influence photon propagation in a scattering media to derive the RTE. Consider the number, N, of photons with propagation direction in the solid angle $\mathrm{d}\omega$ about ω located in the volume element, V, about point $\mathbf{r}$, see Figure 2.2. Denote the surface of V by S. The number of photons propagating in direction ω at time t in the volume V is related to the photon density, $\psi(t, \omega, \mathbf{r})$, through the integral relation

$$N(t, \omega) = \mathrm{d}\omega \int_V \psi(t, \omega, \mathbf{r}) \mathrm{d}\mathbf{r}. \tag{2.8}$$

The differential change in the number of photons in volume V, $\mathrm{d}N(t, \omega)$ in time $\mathrm{d}t$ is

$$\mathrm{d}N(t, \omega) = \mathrm{d}\omega \, \mathrm{d}t \int_V \frac{\partial \psi(t, \omega, \mathbf{r})}{\partial t} \mathrm{d}\mathbf{r}. \tag{2.9}$$

The change in the photon density inside V is accounted for physically by taking account of, one, photons streaming out of V by traveling along straight-line trajectories without scattering or absorption, two, photons scattered out of V entirely, three, photons absorbed within V, and lastly four, photons in V scattered from direction ω' to ω as governed by the phase function. We cast these contributions into the following meta equation

$$\mathrm{d}N(t, \omega) = \quad - \quad (\#\text{ of photons streaming out of } S \text{ in } \mathrm{d}t)$$

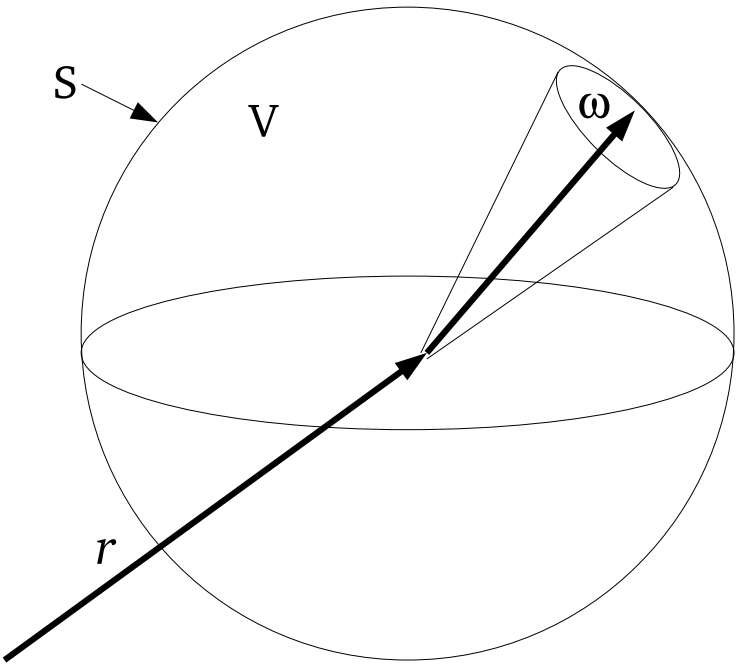

Figure 2.2: An arbitrary volume, V, of scattering material in which photon conservation is considered. S denotes the boundary of V while $\mathbf{r}$ denotes the position in space and ω denotes the propagation direction.

$$
\begin{aligned}
&- \quad (\#\text{ of photons scattered out of } V \text{ in } \mathrm{d}t) \\
&- \quad (\#\text{ of photons absorbed in } V \text{ in } \mathrm{d}t) \\
&+ \quad (\#\text{ of photons scatt. from } \omega' \text{ to } \omega \text{ in } V \text{ in } \mathrm{d}t). \qquad (2.10)
\end{aligned}
$$

Equation (2.9) is used to replace $\mathrm{d}N(t,\omega)$ above, and each of the terms on the right hand side above are represented mathematically as follows

$$
\begin{aligned}
\mathrm{d}\omega\mathrm{d}t \int_V \frac{\partial\psi(t,\omega,\mathbf{r})}{\partial t}\mathrm{d}\mathbf{r} = \quad &- \quad \mathrm{d}\omega\mathrm{d}t \int_S \mathbf{j}(t,\omega,\mathbf{r}) \cdot \hat{n}\, \mathrm{d}S \\
&- \quad c(\sigma_s+\sigma_a)\mathrm{d}\omega\mathrm{d}t \int_V \psi(t,\omega,\mathbf{r})\mathrm{d}\mathbf{r} \\
&+ \quad c\mathrm{d}\omega\mathrm{d}t \int_V \int_{S^2} f(\omega\cdot\omega')\psi(t,\omega',\mathbf{r})\mathrm{d}\omega'\mathrm{d}\mathbf{r}. \qquad (2.11)
\end{aligned}
$$

In the above $\mathbf{j}(t,\omega,\mathbf{r}) \equiv c\,\omega\psi(t,\omega,\mathbf{r})$ is the current density of photons, $c\,\sigma_s\psi(t,\omega,\mathbf{r})\mathrm{d}t$ represents the photon density scattered out of V as photons travel length $c\,\mathrm{d}t$, and $c\,\sigma_a\psi(t,\omega,\mathbf{r})\mathrm{d}t$ represents the photon density absorbed in V as photons travel length $c\,\mathrm{d}t$. Lastly, $f(\omega\cdot\omega')\psi(t,\omega,\mathbf{r})\mathrm{d}\omega$ denotes the photon density scattered from direction ω' to ω at time t.

To obtain the RTE from equation (2.11) we apply the divergence theorem to the surface integral of the current, drop the integration over V, as V was arbitrary. We also drop the arbitrary angle-time volume $\mathrm{d}\omega\mathrm{d}t$ from both sides of (2.11), divide by c, and with a slight rearrangement of terms obtain the RTE

$$
\frac{1}{c}\frac{\partial}{\partial t}\psi(t,\omega,\mathbf{r}) + \nabla\cdot\Big(\,\omega\,\psi(t,\omega,\mathbf{r})\,\Big) + \sigma_a\psi(t,\omega,\mathbf{r}) = \int_{S^2} f(\omega\cdot\omega')\psi(\omega',\mathbf{r})\mathrm{d}\omega' - \sigma_s\psi(t,\omega,\mathbf{r}). \qquad (2.12)
$$

We verify that the RTE for the photon *density*, ψ, can easily be transformed into an RTE for the *specific intensity*, I, by scaling both sides by $ch\nu$ as governed by equation (2.1). Boundary and initial conditions for the RTE will be considered in the next section.

One aspect concerning the general appearance of the RTE we bring attention to is the presence of the divergence operator in (2.12). In Cartesian coordinates it

is customary to employ the identity $\nabla \cdot \mathbf{j} = \nabla \cdot (\omega\, \psi) = \omega \cdot \nabla\psi + \psi \nabla \cdot \omega = \omega \cdot \nabla\psi$. However, in general curvilinear systems $\nabla \cdot \omega \neq 0$, and the form of the RTE presented in (2.12) should be kept in mind, ie. the presence of the divergence instead of the gradient.

For convenience, we will write the RTE as

$$\frac{\partial}{\partial t}\psi(t,\omega,\mathbf{r}) + \nabla \cdot (\,\omega\,\psi(t,\omega,\mathbf{r})\,) + \sigma_a\psi(t,\omega,\mathbf{r}) = \mathcal{L}[\psi(t,\omega,\mathbf{r})], \tag{2.13}$$

where $\mathcal{L}[\cdot]$ represents the scattering operator and we have taken $c = 1$. For now we take the scattering operator to be the integral scattering operator in (2.12), though in Chapter 3 we will consider approximate scattering operators characterized by the presence of differential operators in the direction-space variable ω.

2.3 Specialization to Plane-Parallel Geometries

Throughout the presentation to follow we focus on the plane-parallel problem in which the RTE is used to model light propagation in a random media bounded by two infinite planes a distance L apart. A *normally* incident probing beam is used to illuminate the scattering media, entering the plane at $z = 0$ and exiting through the plane at $z = L$, see Figure 2.3. This scenario is of special significance as the plane-parallel picture is commonly used to approximate the geometry of tissue samples studied in biomedical optics applications. The scattering media is further assumed to be index-matched to the surrounding vacuum so that reflection, and hence the application of Snell's law at the boundaries, can be omitted.

Steady-state infinite plane-wave illumination will be investigated. This corresponds to the boundary condition in which an infinitely wide beam illuminates the entirety of the surface at $z = 0$. Infinite plane wave boundary conditions impose planar symmetry on the solutions of the RTE. In the next section this

symmetry will be exploited to re-write the RTE in a reduced number of variables.

2.3.1 RTE for Infinite Plane-Wave Illumination of a Half-Space

Due to the infinite extent of the normally incident light source, the radiance will exhibit dependence only on the depth, z, and the cosine, μ, of the angle between the direction vector ω of propagation and the $\hat{z}$ direction, ie. $\mu = \omega \cdot \hat{z}$. To develop a transport equation in this scenario, one need only eliminate the x and y derivatives in the divergence operator of equation (2.13) and replace ω with $\mu = \omega \cdot \hat{z}$. This results in

$$\left(\frac{\partial}{\partial t} + \mu\frac{\partial}{\partial z} + \sigma_a\right)\psi(t,\mu,z) = \mathcal{L}[\psi(t,\mu,z)], \tag{2.14}$$

with the following steady-state angular boundary data on the faces of the slab

$$\psi(\mu, z=0) = \psi_0\delta(\mu-1), \quad \text{for } \mu \in [0,1], \tag{2.15}$$

$$\psi(\mu, z=L) = 0, \quad \text{for } \mu \in [-1,0]. \tag{2.16}$$

2.4 Fluence and Flux

The quantities we determine from a knowledge of the steady-state photon density, $\psi(\mu, z)$ include the backscattered and transmitted integrated flux at the boundaries of the slab, along with the fluence rate. Each is defined in the case of infinite plane-wave illumination. Here W stands for Watts.

Backscattered and transmitted flux

$$R = -\int_{-1}^{0} \mu\psi(\mu,0)\mathrm{d}\mu \ \ [\mathrm{W/cm^2}], \tag{2.17}$$

$$T = \int_{0}^{1} \mu\psi(\mu,L)\mathrm{d}\mu \ \ [\mathrm{W/cm^2}]. \tag{2.18}$$

The fluence rate

$$F(z) = 2\pi\int_{-1}^{1} \psi(\mu,z)\mathrm{d}\mu \ \ [\mathrm{W/cm}]. \tag{2.19}$$

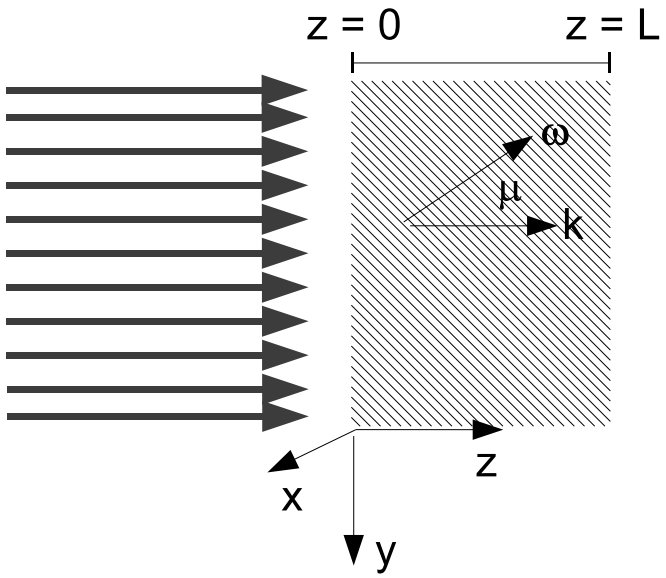

Figure 2.3: The plane-parallel problem. The scattering material extends infinitely in the x and y directions and is bounded in z. Due to normal incidence of the infinite plane-wave illumination, the radiance depends on depth, z, and cosine, $\mu = \omega \cdot \hat{k}$, of the scattering angle.

These quantities will all be compared and contrasted as the tissue-light interaction in the radiative transport equation is varied to incorporate large-angle scattering (Henyey-Greenstein) to small-angle scattering (generalized Fokker-Planck equations). In Chapter 3 all of the different scattering models to be studied are introduced.

2.5 Characteristic Length Scales and the Diffusion Approximation

In an effort to further reduce the complexity of the transport equation, researchers have considered transport on "large" length and time scales to utilize the diffusion approximation. In the next sections we qualify the term "large" by introducing the characteristic length scales, the scattering and transport mean free paths, used to describe transport and diffusive behaviors of light propagation in scattering materials, respectively.

2.5.1 Scattering and Transport Mean Free Path

There are two characteristic length scales that are used to describe light propagation in random media. The first is l_s, known as the scattering mean free path (mfp). It is defined as

$$l_s = \frac{1}{\sigma_s} \quad [\text{cm}]. \tag{2.20}$$

The scattering mfp is the average distance photons travel before being scattered. Media in which $l_s \ll 1$ are termed "optically thick", while those in which $l_s \gg 1$ are considered transparent (for sufficiently small absorption). The scattering mfp is the length scale upon which the transport equation is valid as particles travel along straight lines until scattered or absorbed. This scale is mesoscopic as l_s ranges from 0.001 to 0.01 [cm].

The second characteristic length scale is known as the transport mean free

path though it describes the length scale of the diffusion approximation to be discussed. The transport mfp is given by

$$l_t = \frac{l_s}{(1-g)} = \frac{1}{\sigma_s(1-g)} \quad [\text{cm}]. \tag{2.21}$$

As a comparison, we consider the following example characteristic of tissue optics: if $g = 0.99$ and $l_s = 0.01$ [cm], then $l_t = 1$ [cm]. Hence l_t and l_s can easily differ by several orders of magnitude. In the presence of absorption, some authors define the transport mfp as

$$l_t = \frac{1}{\sigma_s(1-g) + \sigma_a} \quad [\text{cm}]. \tag{2.22}$$

The transport mfp is the distance photons must travel so that their initial trajectories are completely randomized. As an example, if $g = 0.99$, $\sigma_s = 100$ [cm^{-1}], and $\sigma_a = 1$ [cm^{-1}], $l_t = 50\ l_s$. Note that as the scattering becomes more anisotropic, l_t increases. This is as result of the forward scattering delaying the onset of the diffusive behaviors so that diffusion takes place on a large scale.

2.5.2 The Diffusion Approximation

In the limit of long propagation times without extinction of the photon distribution due to absorption, photons scatter numerous times giving rise to a random walk-like behavior in space. For this time-asymptotic picture to hold, the photon density must be far from sources and boundaries, though perturbations to the diffusion approximation have been analyzed when these requirements are not satisfied [20, 6, 5, 50].

As a result, the diffusion equation is used to describe the photon density far from sources. "Far" in this case depends intimately on the scattering media at hand. For suspensions of latex beads suspended in water, Alfano and researchers [61] have shown that the diffusion approximation is valid for distances beginning at 7 l_t.

The diffusion approximation is typically derived in two ways: either as a sum of the first d + 1 spherical harmonics of the projection of the photon density on the spherical harmonics in the direction space variables [14] (here d is the number of spatial dimensions) or as an asymptotic expansion in the limit of vanishing scattering mfp [36]. Here we give a brief exposition using the asymptotic argument as $l_s \to 0$. To ensure scattering dominates absorption we define the scaling parameter ϵ (scattering mfp) and the total scattering cross section, σ_{tot}, as

$$\epsilon = \frac{1}{\sigma_s}, \quad \sigma_{tot} = \sigma_s + \epsilon^2 \sigma_a. \tag{2.23}$$

Hence, as ϵ tends to zero, $\sigma_s \gg \sigma_a$. In addition we define the macroscopic variables $(t', \mathbf{r}') = (\epsilon^2 t, \epsilon \mathbf{r})$. The scaled transport equation is

$$\epsilon \partial_{t'} \psi + \epsilon \nabla' \cdot (\omega \psi) + \epsilon \sigma_a \psi = \frac{1}{\epsilon} \mathcal{L}[\psi], \tag{2.24}$$

and we simplify the treatment by considering the above with angularly independent boundary conditions. Otherwise, a treatment of the initially angularly dependent radiance would have to be accounted for [20]. Next, the asymptotic expansion

$$\psi_\epsilon = \psi_0 + \epsilon \psi_1 + \mathcal{O}(\epsilon^2) \tag{2.25}$$

is substituted into the scaled transport equation. Equating like powers of ϵ we find that at $\mathcal{O}(1/\epsilon)$, ψ_0 is independent of the direction space variable, ω. At $\mathcal{O}(1)$

$$\nabla' \cdot (\omega \psi_0) = \mathcal{L}[\psi_1] = \int_{S^2} f(\omega \cdot \omega') \psi_1 \mathrm{d}\, \omega' - \sigma_s \psi_1. \tag{2.26}$$

We use the identity [14], pg. 198,

$$\int_{S^2} \omega' f(\omega \cdot \omega') \mathrm{d}\, \omega' = g\, \omega \tag{2.27}$$

with g given by (2.5), to express the solution to (2.26) as

$$\psi_1 = \frac{-1}{\sigma_s (1 - g)} \nabla' \cdot (\omega \psi_0) \quad \text{or} \quad = -l_t \nabla' \cdot (\omega \psi_0). \tag{2.28}$$

The solution obtained can be verified by direct substitution, though we refer to [20] for rigorous details of its determination. Lastly the $\mathcal{O}(\epsilon^2)$ equation is integrated over S^2 to give

$$\partial_t \psi_0 - l_t \nabla' \cdot \int_{S^2} \omega (\nabla' \cdot (\omega \psi_0)) \frac{\mathrm{d}\omega}{4\pi} = 0. \tag{2.29}$$

The identity [14], pg. 198,

$$\int_{S^2} \omega (\mathbf{A} \cdot \omega) \mathrm{d}\omega = \frac{4\pi}{3} \mathbf{A} \tag{2.30}$$

allows

$$\nabla' \cdot \int_{S^2} \omega (\nabla' \cdot (\omega \psi_0)) \frac{\mathrm{d}\omega}{4\pi} = \frac{1}{3} \nabla' \cdot \nabla' \psi_0 \tag{2.31}$$

in (2.29) to yield the diffusion equation

$$(\partial_{t'} + \sigma_a) \psi_0 = \nabla' \cdot (D \nabla' \psi_0), \tag{2.32}$$

with diffusion constant

$$D = \frac{1}{3\sigma_s (1 - g)}. \tag{2.33}$$

The diffusion approximation is widely used in tissue optics given its relatively cheap computational costs in large complex domains compared to the radiative transport equation. The primary use of the diffusion equation is its use in optical tomography [1] as a forward model to predict the radiance at detector locations. The inverse problem is then solved to determine the absorption and scattering properties of the medium. Inverse models of this type are being pursued to infer tissue pathologies [1] using NIR light sources.

2.6 Summary

The radiative transport equation was derived from a phenomenological point of view based on particle conservation in an absorbing and scattering media. All wave and quantum aspects of light propagation were ignored. The tissue-light

interaction is determined by the phase function in the integral scattering operator. The phase function is specified *ad hoc* based on empirical arguments. The diffusion approximation of the radiative transport equation was derived as an asymptotic expansion of the photon density in the limit of vanishing scattering mean free path.

In the next chapter we introduce forward scattering approximations to (2.13) and (2.14) developed in the neutron and electron transport literature. These approximations give rise to generalized Fokker-Planck type equations in which the integral scattering operator is replaced by a differential operator in the direction space variables given by ω.

Chapter 3

Forward Scattering Approximations of the Radiative Transfer Equation: Generalized Fokker-Planck Equations

3.1 The Case for Forward Scattering Approximations

Forward scattering occurs when the trajectories of particles injected into a material are nearly unchanged during a single scattering event with the fixed background material through which the particles propagate. Examples of this can be seen in high energy neutron and electron transport as well as light propagation in biological media [17]. Researchers have attempted to exploit this phenomena to simplify the general transport equation (2.12) to account for the dominating forward scattering behavior as $g \to 1$. These considerations were begun in the neutron transport literature [47, 48, 49, 8, 37, 38] and recently adapted by Arnold Kim and researchers to study light propagation in tissues [32, 34, 31, 35]. We expand on Kim's work by considering a wider range of forward scattering models from the neutron transport literature. In addition we focus on the ability of the forward scattering models to approximate the integral scattering operator with Henyey-Greenstein phase function and not on numerical simplifications. The P_N-method, as discussed in the introduction, affords the same amount of computational ease regardless of the scattering theory employed.

Forward scattering approximations serve two roles: first, to describe the dominating forward scattering behavior and second, to simplify the RTE. The

simplification is drastic if one is intent on solving the RTE through the use of collocation methods. For instance, if one considers the use of collocation methods in the direction space, known as the discrete ordinates method [39], the integral term in the RTE is evaluated through Gaussian quadrature. Then the vector of unknowns, ie. the photon density ψ evaluated at discrete points in the direction space, are all coupled. If the integral term can be replaced with a differential operator in the direction space variables, then finite differences can be brought to bear which couple at most three terms [42] . The trade off is that one obtains less computational trouble at the expense of having to develop model-specific finite difference methods for the scattering approximation considered.

In contrast we employ a spectral method, known as the P_N-method, in which the photon density is expanded in Legendre polynomials to solve the RTE and the forward scattering approximations to be considered. The main result of this dissertation is the discovery that the P_N-method leads to uncoupled expansion coefficients for any scattering operator provided the scattering operator has spherical harmonics as eigenfunctions. The forward scattering approximations introduced in this chapter all satisfy this requirement. We remark that the direction space angle dependent pre-factors of the spatial derivatives do lead to coupling-though they couple only two coefficients at a time, see Chapter 4. Using the P_N-method we may shift our perspective of forward scattering approximations from one of computational shortcuts to a study of the ability of the different forward scattering models to reproduce the physics determined by the integral scattering operator with Henyey-Greenstein phase function.

The degree to which the forward scattering approximations are accurate in predicting all aspects of light propagation, including backscatter, transmission and fluence rate, will be assessed in Chapter 5. In the next section we provide an introduction to Fokker-Planck type equations and go on to consider the

generalized Fokker-Planck equations which arise naturally in forward scattering approximations.

3.2 What are generalized Fokker-Planck equations?

The Fokker-Planck equation [52] arose as a means to describe the time evolution of the single particle phase space density function for a particle immersed in a heat bath of fixed temperature. In one dimension, the Fokker-Planck equation is of the form

$$\frac{\partial}{\partial t} f(t,x) = \left(\frac{\partial}{\partial x} D_1(x) + \frac{\partial^2}{\partial x^2} D_2(x) \right) f(t,x). \tag{3.1}$$

The coefficients $D_1(x),\ D_2(x)$ characterize the drift and diffusive properties, respectively, of the stochastic particle trajectory described probabilistically by $f(t,\ x)$. We take Fokker-Planck type equations to be PDE or ODE that describe diffusive behaviors with or without the presence of drift. Hence the familiar diffusion equation is a "Fokker-Planck" equation.

In the coming discussion we will discover equations that describe diffusive behaviors of the photon density, $\psi(t,\omega,\mathbf{r})$, in the direction space variable ω. These equations are generalized Fokker-Planck equations. The term "generalized" is used because diffusion takes place in the direction coordinates and does not correspond to the description of an underlying random process taking place in the spatial coordinates as in say, the diffusion equation. It is possible as well to describe diffusive behaviors of the photon density in the position space variables, see [14, 36, 20] and § 2.5.

The forward scattering approximations to be presented can all be represented generically as

$$\frac{\partial}{\partial t}\psi(t,\omega,\mathbf{r}) + \nabla \cdot (\,\omega\,\psi(t,\omega,\mathbf{r})) + \sigma_a \psi(t,\omega,\mathbf{r}) = F(\triangle_\omega)\psi(t,\omega,\mathbf{r}). \tag{3.2}$$

This is an example of a generalized Fokker-Planck equation (GFPE) due to the

presence of the second order differential operator $\triangle_\omega$, known as the Laplace-Beltrami operator[1] ,

$$\triangle_\omega = \frac{\partial}{\partial\mu}(1-\mu^2)\frac{\partial}{\partial\mu} + (1-\mu^2)^{-1}\frac{\partial^2}{\partial\varphi^2}. \tag{3.3}$$

$F(\cdot)$ is a continuous function defined on the spectrum of $\triangle_\omega$. The eigenfunctions of the Laplace-Beltrami operator are the spherical harmonics [25]

$$Y_{nm}(\theta,\varphi) = (-1)^{(1/2)(m+|m|)}\left(\frac{2n+1}{4\pi}\frac{(n-|m|)!}{(n+|m|)!}\right)^{\frac{1}{2}} P_{n|m|}(\cos\theta)e^{im\varphi}, \tag{3.4}$$

and the eigenvalues of $\triangle_\omega$ are

$$\lambda_n = -n(n+1) \quad \text{for} \quad n = 0,1,2,\ldots. \tag{3.5}$$

The development of a precise form of $F(\cdot)$ such that

$$F(\triangle_\omega)\psi(t,\omega,\mathbf{r}) \approx \int_{S^2} f(\omega\cdot\omega')\psi(\omega',\mathbf{r})\mathrm{d}\omega' - \sigma_s\psi(t,\omega,\mathbf{r}), \tag{3.6}$$

will be the goal of the various forward scattering approximations we consider in the ensuing sections. Mathematically, the ability to define such an $F(\cdot)$ is supported by the spectral mapping theorem for linear operators, see §6.2 of [43], and references therein.

3.3 Approximating the spectrum of the integral scattering operator

Researchers have pursued the approximation of the eigenvalues of the integral scattering operator to devise forward scattering operators that retain the spectral behavior but are computationally less expensive alternatives to integral scattering operators.

The eigenvalue relation of the integral scattering operator with arbitrary phase function $f(\omega\cdot\omega')$, is

$$\mathcal{L}[Y_{nm}(\omega)] = \int_{S^2} f(\omega\cdot\omega')Y_{nm}(\omega')\mathrm{d}\omega' - \sigma_s Y_{nm}(\omega) = -(\sigma_s - \hat{f}_n)Y_{nm}(\omega), \tag{3.7}$$

[1] Also known as the restriction of the Laplacian to the unit sphere or spherical Laplacian.

with

$$\hat{f}_n = 2\pi\sigma_s \int_{-1}^{1} f(\omega\cdot\omega')P_n(\omega\cdot\omega')\mathrm{d}(\omega\cdot\omega'). \tag{3.8}$$

In practice, $\hat{f}_n$ can be computed using Gauss-Legendre quadrature[12] when closed-form formulas are not available. For the case in which $f(\omega\cdot\omega')$ is the Henyey-Greenstein phase function, $\hat{f}_n = \sigma_s g^n$. Letting $\xi = \omega\cdot\omega'$, this can be seen by inserting the Legendre polynomial series representation

$$\frac{\sigma_s(1-g^2)}{4\pi(1-2g\xi+g^2)^{3/2}} = \sigma_s\sum_{n=0}^{\infty}\frac{2n+1}{4\pi}g^nP_n(\xi). \tag{3.9}$$

into (3.8). The eigenvalue relation for integral scattering with Henyey Greenstein phase function is thus

$$\mathcal{L}_{\mathrm{HG}}[Y_{nm}(\omega)] = -\sigma_s(1-g^n)Y_{nm}(\omega). \tag{3.10}$$

Five approximations of the spectrum will be considered in the ensuing sections. The first is the development of the high order Fokker-Planck equation, devised by Pomraning [48]. As a by-product the standard Fokker-Planck equation, (3.2) with $F(\triangle_\omega) = \triangle_\omega$, can be obtained by truncating the high order Fokker-Planck operator. Next, two approximations due to Larsen [37, 38] are developed. The first is the expansion of g^n in (3.10) about $g = 1$, and the second is the approximation of the spectrum of the general integral scattering operator, ie. without a specific choice of $f(\omega\cdot\omega')$, using a rational approximation, $F(\triangle_\omega) = \alpha\triangle_\omega(1-\beta\triangle_\omega)^{-1}$. The rational approximation is considered here in the context of tissue optics in which Kim's modification [32] enters. Lastly, we make a further modification of the rational approximation useful for numerical applications using the P_N-method developed in the next chapter.

All of the approximate spectra will be compared to the spectra of the integral scattering operator with Henyey-Greenstein phase function. This will provide insight into their success in approximating the exact formulation of scattering in tissue optics.

3.3.1 High order Fokker-Planck operators

With an eye on approximating the spectra of the integral scattering operator, the development of the high order Fokker-Planck equation starts from the assumption that scattering events only slightly change the trajectories of particles. This assumption can be formalized by assuming that the phase function, $f(\xi)$, satisfies

$$\text{for } \xi \in [-1,1),\ f(\xi) \ll f(1) \text{ and } f(\xi) \ll 1. \tag{3.11}$$

The utilization of this assumption is made in the expression of the Legendre moments of the phase function by noting the integrand in (3.8) is roughly zero except near $\xi = 1$. The ξ dependence of the Legendre Polynomials in the definition of $\hat{f}_n$ is expanded in a Taylor series about $\xi = 1$,

$$P_n(\xi) = \sum_{l=0}^{\infty} \frac{(-1)^l}{l!} \left(\frac{d^l}{d\xi^l} P_n(\xi = 1) \right) (1-\xi)^l. \tag{3.12}$$

We remark that because the Legendre polynomial of order n only possesses n-derivatives, the sum above can really only be carried out to $l = n$. Pomraning [48] showed that for $1 \leq l \leq n$,

$$\frac{d^l}{d\xi^l} P_n(\xi = 1) = \frac{1}{2^l l!} \prod_{i=0}^{l-1} \Big(n(n+1) - i(i+1) \Big). \tag{3.13}$$

For $l = 0$, $P_n^{(0)}(1) = 1$. Equation (3.13) is substituted into (3.12). This expression is in turn substituted into the definition of $\hat{f}_n$ which is placed in (3.7) to give

$$\mathcal{L}[\psi] = 2\pi \sum_{n=0}^{\infty} \sum_{m=-n}^{+n} \hat{\psi}_{nm}(t,\mathbf{r}) Y_{nm}(\omega) \sum_{l=0}^{n} \frac{(-1)^l}{2^l (l!)^2} \prod_{i=0}^{l-1} \Big(n(n+1) - i(i+1) \Big) \int_{-1}^{1} (1-\xi)^l f(\xi) \mathrm{d}\xi - \sigma_s \psi. \tag{3.14}$$

At this point we have approximated the spectrum of the integral scattering operator. An important question to ask is what operator gives rise to this approximation? The answer is arrived at by recognizing that the product of $n(n+1)$ and $Y_{nm}(\omega)$ can be replaced by -$\triangle_\omega Y_{nm}(\omega)$. The final high order Fokker-Planck

equation can be written succinctly with the definitions

$$H_l = \begin{cases} 1, & l = 0, \\ \frac{(-1)^{l+1}}{2^l (l!)^2} \prod_{i=0}^{l-1} \Big(\triangle_\omega + i(i+1) \Big), & 1 \leq l \leq n. \end{cases}$$

and

$$T_l = 2\pi \int_{-1}^{1} (1-\xi)^l f(\xi) \mathrm{d}\xi \tag{3.15}$$

allowing

$$\mathcal{L}[\psi] = \sum_{l=0}^{\infty} H_l T_l \psi(t, \omega, \mathbf{r}) - \sigma_s \psi \tag{3.16}$$

The use of equation (3.16) in the RTE results in a GFPE of high order. For reference we list the high order Fokker Planck equation (HOFP)

$$\frac{\partial}{\partial t}\psi(t, \omega, \mathbf{r}) + \nabla \cdot (\omega \, \psi(t, \omega, \mathbf{r})) + \sigma_a \psi(t, \omega, \mathbf{r}) = \sum_{l=0}^{\infty} H_l T_l \psi(t, \omega, \mathbf{r}), \tag{3.17}$$

with H_l and T_l given by (3.3.1) and (3.15), respectively.

3.3.2 The standard Fokker-Planck equation

Asymptotic arguments concerning the value of T_l based on the degree of forward scattering, ie. the value of g, can be employed to truncate the sum in (3.16) at some finite value of l. We verify that $T_0 = \sigma_s$, $T_1 = \sigma_s(1-g)$, $H_0 = 1$ and $H_1 = \triangle_\omega / 2$. Defining $\epsilon = 1 - g$, we can expand (3.16) to order ϵ assuming $\epsilon \ll 1$

$$\begin{aligned} \mathcal{L}[\psi] &= \sigma_s \Big(1 + \frac{\epsilon}{2} \triangle_\omega + \mathcal{O}(\epsilon^2) \Big) \psi - \sigma_s \psi \\ &= \frac{\sigma_s \epsilon}{2} \triangle_\omega \psi. \end{aligned} \tag{3.18}$$

This scattering operator substituted into the RTE gives the "standard" Fokker-Planck equation

$$\frac{\partial}{\partial t}\psi(t, \omega, \mathbf{r}) + \nabla \cdot (\omega \, \psi(t, \omega, \mathbf{r})) + \sigma_a \psi(t, \omega, \mathbf{r}) = \frac{\sigma_s (1-g)}{2} \triangle_\omega \psi(t, \omega, \mathbf{r}). \tag{3.19}$$

In Appendix A the compatibility of the HOFP and the standard Fokker-Planck equations with the integral scattering operator using the Henyey-Greenstein phase function is assessed. It is found that neither the HOFP nor the standard Fokker-Planck equation are valid in the limit $\epsilon \to 0$ for the integral scattering operator determined by the Henyey-Greenstein phase function. This is a result of the violation of (3.11) by the Henyey-Greenstein phase function. Nonetheless, we explore the predictive power of these equations for tissue optics in Chapter 5. We remark that the exponential phase function (2.7) does satisfy (3.11).

3.3.3 A standard Fokker-Planck operator in combination with a pseudo-differential operator

The end product of this particular treatment will be the development of an equation that captures the spectral properties of the integral scattering operator in the limit of high optical thickness and forward-peaked scattering.

Optically thick media are those in which the average distance between scattering events, given by l_s, see §2.5, tends to zero. Forward scattering here refers to the limit that the anisotropy, g, tends to one. No assumption of the form (3.11) is made. Let: $\epsilon = 1 - g$ and $\sigma_s = \sigma/\epsilon$. Then in the limit $\epsilon \to 0$ the following situations occurs: $l_s = \sigma_s^{-1} \to 0$ and $g \to 1$. The eigenvalues of the integral scattering operator with Henyey-Greenstein phase function are

$$\mathcal{L}_{\mathrm{HG}}[Y_{nm}(\omega)] = -\sigma_s(1 - g^n)Y_{nm}(\omega) \tag{3.20}$$

Replacing g and σ_s with the new definitions above gives

$$\mathcal{L}_{\mathrm{HG}}[Y_{nm}(\omega)] = -\frac{\sigma}{\epsilon}(1 - (1 - \epsilon)^n)Y_{nm}(\omega). \tag{3.21}$$

Expanding the rhs in a Taylor series about $\epsilon = 0$ and retaining only quadratic terms in ϵ yields

$$\mathcal{L}_{H.G.}[Y_{nm}(\omega)] = \Big(\sigma(1 + \epsilon)[-n] - \frac{\epsilon\sigma}{2}[-n(n + 1)] + \mathcal{O}(\epsilon^2)\Big)Y_{nm}(\omega). \tag{3.22}$$

Lastly, the eigenvalue relation, $\triangle_\omega Y_{nm} = -n(n+1)Y_{nm}$, is employed to introduce the Laplace-Beltrami operator in the direction space variable, ω. The product $-nY_{nm}(\omega)$ is replaced with the pseudo-differential operator, $\mathcal{L}_{3/2}$, defined in Appendix B, owing to

$$\mathcal{L}_{3/2}[Y_{nm}(\omega)] = \frac{1}{4\pi\sqrt{2}} \int_{S^2} \frac{Y_{nm}(\omega')}{(1-\omega\cdot\omega')^{3/2}} \mathrm{d}\omega' = -nY_{nm}(\omega). \tag{3.23}$$

We remark that the above equation is to be interpreted as a principal value for the integral to exist. The steady-state GFPE involving the pseudo-differential operator to first order in ϵ is

$$\nabla\cdot(\,\omega\,\psi(t,\omega,\mathbf{r})\,)+\sigma_a\psi(t,\omega,\mathbf{r}) = \sigma_s(1-g)(2-g)\mathcal{L}_{3/2}[\psi(t,\omega,\mathbf{r})] - \frac{\sigma_s(1-g)^2}{2}\triangle_\omega\psi(t,\omega,\mathbf{r}). \tag{3.24}$$

This equation is a linear combination of the standard Fokker-Planck operator and the pseudo-differential operator $\mathcal{L}_{3/2}$. The term $\mathcal{L}_{3/2}$ incorporates large angle scattering while the standard Fokker-Planck term describes forward scattering. Note that the eigenvalues of this operator can become positive for $1-g$ sufficiently greater than zero. See Figure 3.1.

3.3.4 The modified Leakeas-Larsen equation

To approximate the spectrum of the integral scattering operator, Leakeas and Larsen [38] proposed a rational function of the Laplace-Beltrami operator with two free parameters α and β of the form

$$F(\triangle_\omega)Y_{nm}(\omega) = \alpha\triangle_\omega(1-\beta\triangle_\omega)^{-1}Y_{nm}(\omega) \tag{3.25}$$

$$= -\alpha[n(n+1)](1+\beta[n(n+1)])^{-1}Y_{nm}(\omega). \tag{3.26}$$

α and β are chosen such that $-(\alpha n(n+1))(1+\beta n(n+1))^{-1}$ approximates the RTE eigenvalues $-(\sigma_s - \hat{f}_n)$ as well as possible.

Kim and Keller noted [32] that for the Henyey-Greenstein phase function, $\hat{f}_n = \sigma_s g^n$ tends to zero as $n \to \infty$. Then in the limit $n \to \infty$, it is desirable that $\alpha/\beta = \sigma_s$, so that the asymptotic behavior of the eigenvalues can be captured by the parameters α and β. This is the "modification" that specializes the work of Leakeas and Larsen to tissue optics, hence the name "modified Leakeas-Larsen equation". If in addition the parameters α and β are forced to capture the $n = 1$ eigenvalue $-(\sigma_s - \hat{f}_1)$, as $n = 0$ is implicitly satisfied by construction, two equations for α and β are obtained allowing for their determination. This results in [2]

$$\alpha = \frac{\sigma_s(1-g)}{2g}, \quad \beta = \frac{1-g}{2g}. \tag{3.27}$$

The modified Leakeas-Larsen equation (MLLE) is thus

$$\frac{\partial}{\partial t}\psi(t,\omega,\mathbf{r}) + \nabla\cdot(\,\omega\,\psi(t,\omega,\mathbf{r})\,) + \sigma_a\psi(t,\omega,\mathbf{r}) = \alpha\triangle_\omega(1-\beta\triangle_\omega)^{-1}\psi(t,\omega,\mathbf{r}). \tag{3.28}$$

3.3.5 The second modified Leakeas-Larsen equation

In the next chapter, the P_N-method will be developed to solve the RTE with Henyey-Greenstein phase function as well as the GFPE's developed in the present chapter. One feature of the P_N-method that will become evident is the use of the first N-eigenvalues of the scattering operator under consideration to generate solutions. Computationally, one would never be able to use the full infinite set of eigenvalues of the scattering operator at hand. With $N = 46$, it has been shown that six digit accuracy can be obtained for solutions of the RTE in the semi-infinite slab subject to plane wave illumination, see [44] as well as Figure 5.1 of § 5.3. With this in mind, the asymptotic properties of the integral scattering operator eigenvalues used to determine the parameters α and β of the Leakeas-Larsen rational approximation should be adjusted.

[2] We remark that these expressions are different than those obtained by Kim and Keller [32] but we assume that (14) is what they had in mind.

For a given calculation using the P_N-method, in which N-eigenvalues of the scattering operator are used, the highest order eigenvalue of the integral scattering operator to be approximated in the Leakeas-Larsen equation is

$$\lambda_N = -\sigma_s(1 - g^N). \tag{3.29}$$

This is of importance as for specific values of g it will *not* be the case that $g^N = 0$. An example of this is $g = 0.9$ with $N = 100$, so that $(0.9)^{100} \approx 0.366$. Thus, for a given calculation, a more accurate approximation of the first N eigenvalues of the integral scattering operator with Henyey-Greenstein phase function by the rational approximation of Leakeas and Larsen can be obtained by requiring that

$$\frac{\alpha}{\beta} = \sigma_s(1 - g^N). \tag{3.30}$$

In this case α and β are defined according to

$$\alpha = \sigma_s(1 - g^N)\beta, \quad \beta = \frac{1 - g}{2(g - g^N)}. \tag{3.31}$$

This adjustment will be shown to improve the accuracy of the Leakeas-Larsen approximation in the limit as g tends to unity.

3.4 Comparison of scattering operator spectra

Having recalled the forward scattering approximations due to asymptotic and spectral approximation arguments we close with a comparison of the eigenvalues of each scattering operator derived. All of the scattering operators have an eigenspace defined by the set of spherical harmonics, an essential feature that will be exploited in the sequel when we formulate the P_N-method to solve the RTE along with the GFPE's. For completeness the eigenvalues of each of the scattering operators derived in the previous sections are listed below.

(1) Integral scattering operator with arbitrary phase function

$$\lambda_n = -\sigma_s(1 - \hat{f}_n) \tag{3.32}$$

(2) Integral scattering operator with Henyey-Greenstein phase function

$$\lambda_n = -\sigma_s(1 - g^n) \tag{3.33}$$

(3) High order Fokker-Planck scattering operator (3.16)

$$\lambda_n = \begin{cases} 0, & l = 0, \\ 2\pi\sigma_s \sum_{l=1}^{n} \frac{(-1)^l}{2^l (l!)^2} \prod_{i=0}^{l-1} \Big([n(n+1)] - i(i+1) \Big) \int_{-1}^{1} (1-\xi)^l f(\xi) \mathrm{d}\xi, & 1 \le l \le n. \end{cases} \tag{3.34}$$

(4) Standard Fokker-Planck scattering operator (3.19)

$$\lambda_n = \frac{\sigma_s(1-g)}{2}[-n(n+1)] \tag{3.35}$$

(5) Standard Fokker-Planck scattering operator with $\mathcal{L}_{3/2}$ (3.24)

$$\lambda_n = (1-g)(2-g)[-n] + \frac{\sigma_s(1-g)^2}{2}[n(n+1)] \tag{3.36}$$

(6) Modified Leakeas-Larsen rational approximation (3.28)

$$\lambda_n = \frac{\alpha[-n(n+1)]}{1 + \beta[n(n+1)]} \tag{3.37}$$

In Figure 3.1 we present a typical comparison of the spectra over the range $n = 0$ up to $n = 25$ for $g = 0.9$. To assess the accuracy of the approximations, the spectra of the scattering operators is compared over the range of relevant optical properties that characterize the tissue optics regime: $g \in [0.7,\ 1)$. Defining $\lambda_{H.G.}(n)$ to be the eigenvalues of the integral scattering operator with Henyey-Greenstein phase function and $\lambda_{GFP}(n)$ to be the eigenvalues of the generalized Fokker-Planck operators, the error

$$E(g; N) = \max_{n \in [0,N]} \frac{|\lambda_n^{HG}(g) - \lambda_n^{GFP}(g)|}{|\lambda_n^{HG}(g)|} \tag{3.38}$$

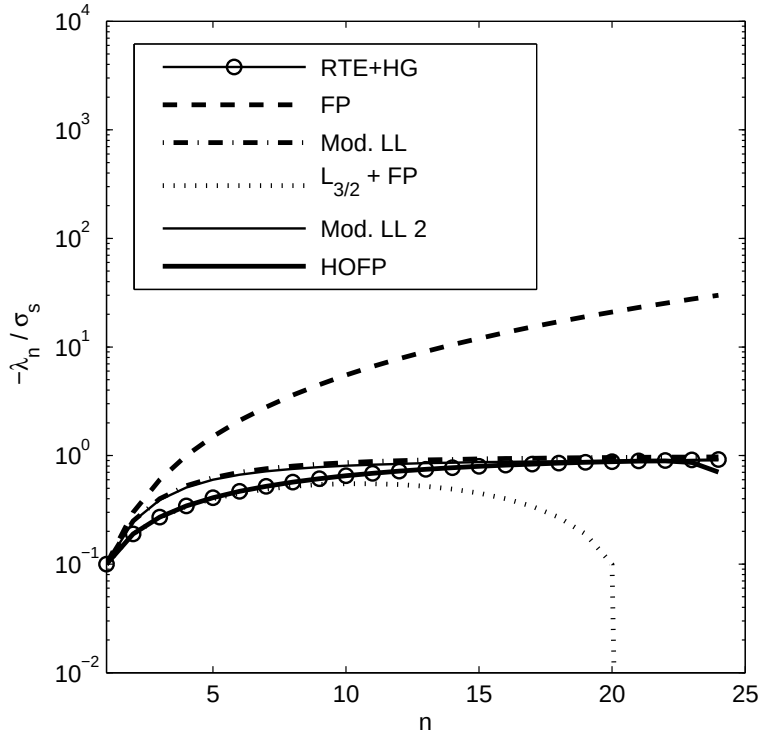

Figure 3.1: Comparison of GFP and RTE+HG spectra for $g = 0.9$, $\sigma_s = 100$ [cm^{-1}].

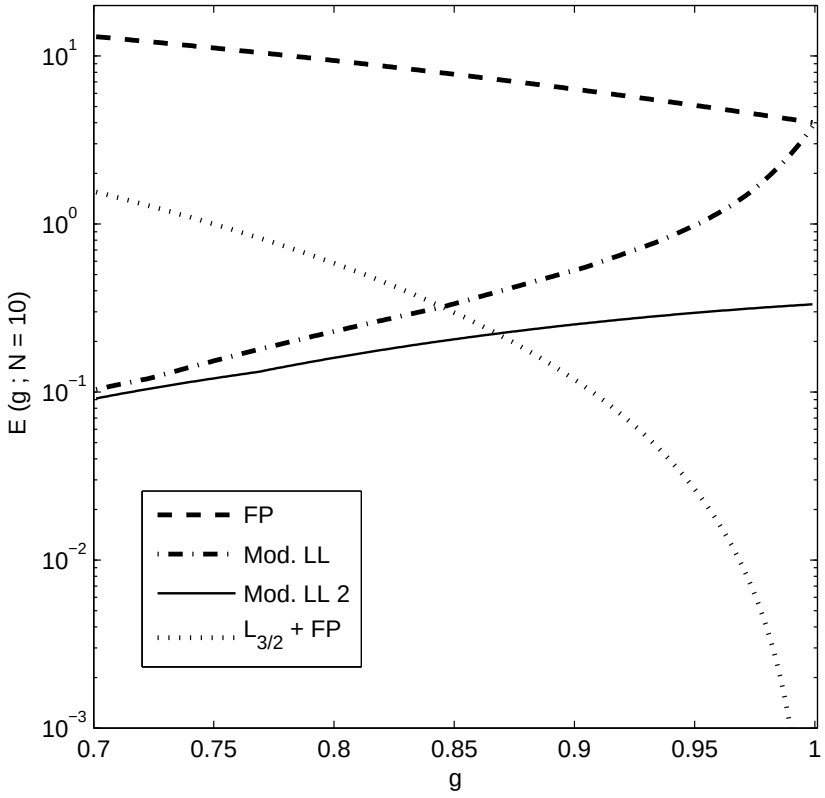

Figure 3.2: Error in GFP scattering operator spectra for $N = 10$.

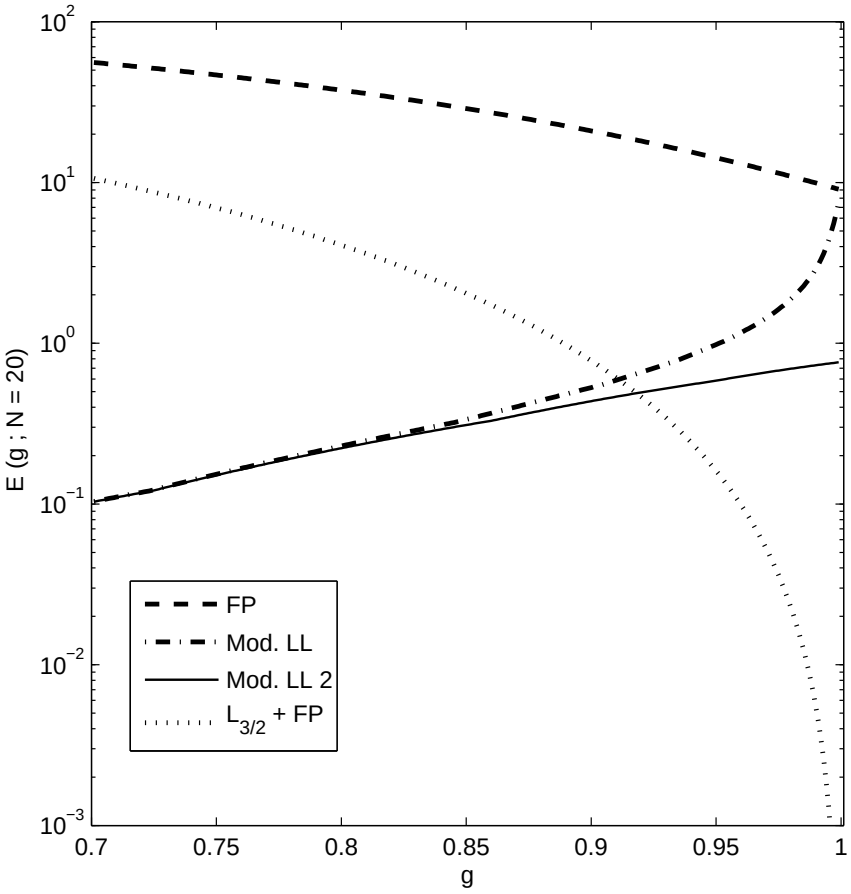

Figure 3.3: Error in GFP scattering operator spectra for $N = 20$.

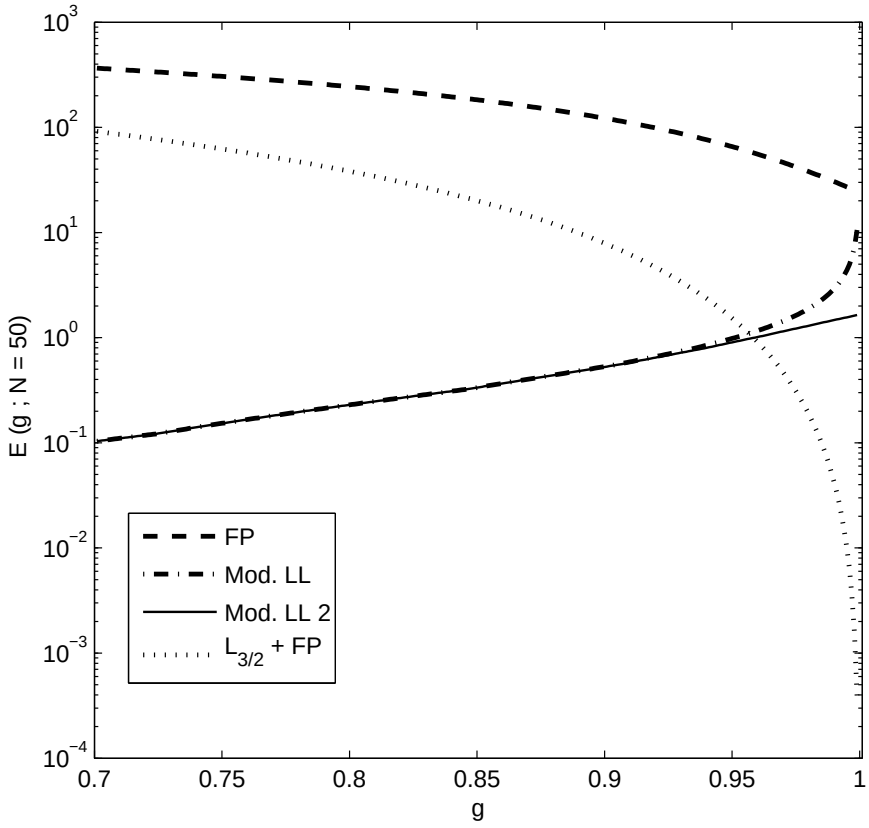

Figure 3.4: Error in GFP scattering operator spectra for $N = 50$.

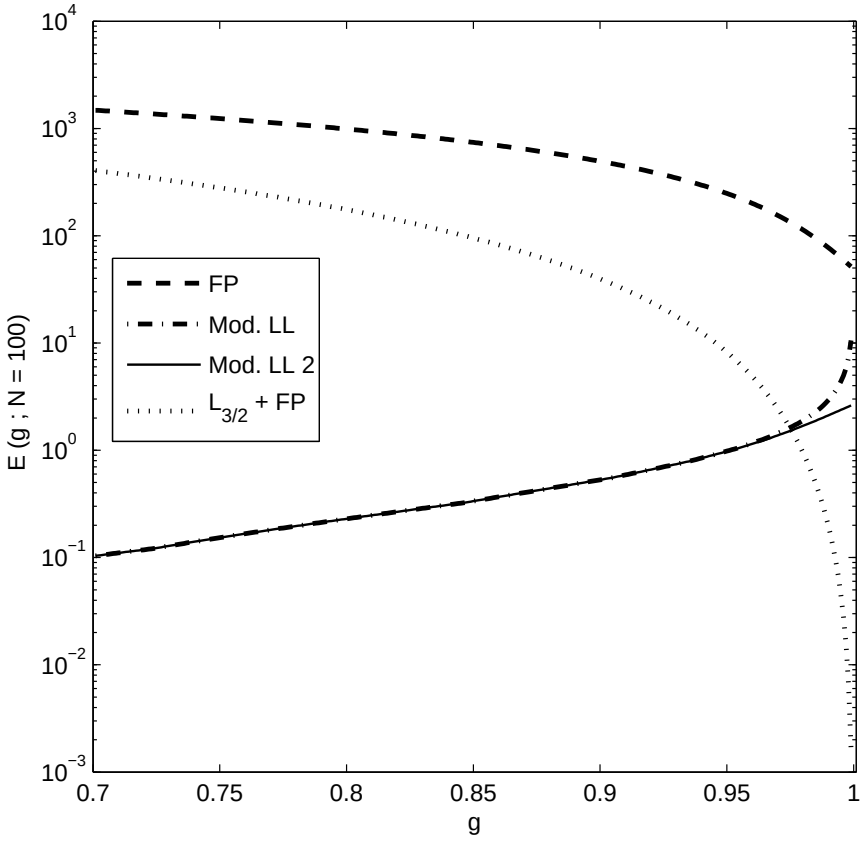

Figure 3.5: Error in GFP scattering operator spectra for $N = 100$.

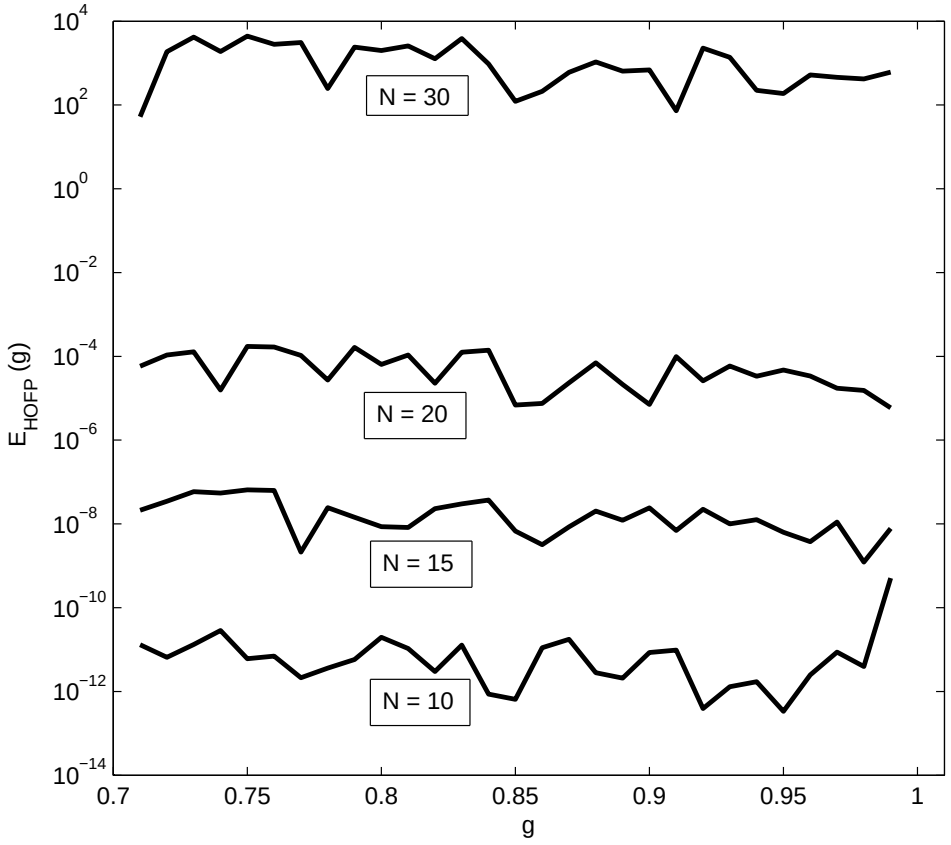

Figure 3.6: Error of the HOFP scattering operator spectra for $N = 10, 15, 20, 30$.

in the discrete maximum norm is presented for all the GFPE (except for the HOFP) in Figures 3.2-3.5, for $N = 10, 20, 50, 100$ and with $g \in [0.7,\ 1)$. The error is by construction independent of σ_s. HOFP errors are reported in Figure 3.6.

The progression of figures illustrates that the modified Leakeas-Larsen scattering operators do the best job in reproducing the eigenvalues over the most values of g, particularly as the number N of eigenvalues considered increases. Because the eigenvalues of the Fokker-Planck equation are unbounded, they provide a poorer representation of the true spectra- though they improve as g approaches one. The figures demonstrate the existence of a threshold in g beyond which the the Fokker-Planck operator in combination with $\mathcal{L}_{3/2}$ reproduces the spectra best. This threshold value of the anisotropy shifts to larger g with increasing N as a result of the unbounded behavior in N exhibited by the eigenvalues in (3.36).

As well, the figures indicate that the correction to the modified Leakeas-Larsen equation to capture the "locally" asymptotic eigenvalue, ie. the highest order eigenvalue $\lambda_N = -\sigma_s(1-g^N)$, of the integral scattering operator with Henyey-Greenstein phase function, reduces the error in the spectra for g near one. This correction is more noticeable at lower values of N where the locally asymptotic eigenvalue and the true asymptotic eigenvalue of the RTE with Henyey-Greenstein phase function differ by the greatest magnitude.

The HOFP eigenvalues reproduce the spectrum extremely well for $N \leq 20$. Unfortunately, these eigenvalues become unbounded for $N > 20$. For calculations involving up to $N = 20$ eigenvalues, no differences in the predicted photon density should be observed when using the HOFP spectra. However, typical calculations of the photon density when $g = 0.9$ require $N = 30$ eigenvalues to obtain converged solutions when using the P_N-method [44], see § 5.2.

3.5 Summary

Forward scattering approximations to the integral scattering operator of the RTE were derived. These approximations introduce functions of the spherical Laplacian by attempting to reproduce the eigenvalues of the integral scattering operator. The high order Fokker-Planck scattering operator was found to reproduce the spectra of the integral scattering operator over the appropriate optical range of anisotropies characteristic of tissue optics the best for $N \leq 20$ eigenvalues. However, calculations involving greater than $N = 20$ eigenvalues become suspect as the HOFP spectra becomes unbounded. For calculations requiring more than 20 eigenvalues, a suitable replacement for $g \leq 0.95$ is the modified Leakeas-Larsen equation, corrected to capture the locally asymptotic behavior of the integral scattering operator eigenvalues. For sufficiently strong anisotropy, ie. $g > 0.95$, the standard Fokker-Planck operator in combination with the pseudo-differential operator $\mathcal{L}_{3/2}$ provided the best approximation to the spectrum of the integral scattering operator.

In the next chapter a spectral method, known as the P_N-method, will be applied to the RTE to generate solutions for the cases of infinite and collimated plane wave illumination of a semi-infinite half space. First a presentation of spectral methods will be presented and then specialization to the tissue optics problem will be considered.

Chapter 4

The P_N-Method

4.1 Introduction to Spectral Methods

Spectral methods [12, 57] are a class of discretization schemes for differential equations. The key components of a spectral methods' formulation are the trial functions, also known as the expansion or approximating functions, and the test functions, also known as weight functions, used. The trial functions are used to express the variable dependence of the unknown solution of the differential equation through projection. The test functions are used to enforce the differential equation in a weak sense; through integration against the test function. The choice of trial/test functions used in the discretization scheme distinguishes the spectral method. Examples of spectral methods with different test/trial functions include Galerkin, collocation, and tau-spectral methods and the finite element method.

For Galerkin spectral methods, the space of test functions and trial functions are the same. The choice of a set of test functions is made so that the members of the set individually satisfy all or some of the boundary conditions. The differential equation is enforced by requiring that the integral of the residual times each test function be zero, accounting in the process of integration for any remaining boundary conditions. The trial functions in a Galerkin method are typically a complete orthonormal set of polynomials over the domain of the problem and arise as solutions (eigenfunctions) to singular Sturm-Liouville problems. Examples are

the Legendre polynomials, Chebyshev polynomials, etc.

In collocation methods, the trial functions are translated Dirac delta functions centered at the collocation points. This approach requires that the differential equation be satisfied in the strong sense, ie. pointwise, at the collocation points. Tau methods are essentially the same as the Galerkin method however, the trial functions need not satisfy the boundary conditions. Instead the boundary conditions are enforced through a supplementary set of equations called the "tau-conditions".

Finite element methods divide the domain of the problem into small elements and the trial/test functions are low-order functions specified in each element. The low-order functions are (nearly) locally orthogonal and are used to describe local properties of the solutions as opposed to the global description of test functions in the Galerkin method. Finite-elements are well suited for complex geometries owing to the local character of the trial functions.

Higher dimensional problems in all of the methods above are treated using tensor products of trial functions [13]. These methods result in large sparse matrices that are typically in need of pre-conditioning to determine the unknown expansion coefficients of the solution. This procedure has been carried out extensively in fluid dynamics [11] and various other fields [9].

Alternatives to the use of tensor products of trial functions are composite methods in which a spectral approach in one variable is combined with Fourier or Laplace transform, finite differences, or normal mode expansions in the other variables. For the case of the radiative transport equation, composite methods which employ, for example, collocation in angle and normal mode expansions (real exponentials) in space have been more common [7, 33, 32]. We mention as well composite Galerkin methods in space using Chebyshev polynomials in combination with collocation in angle [33, 3]. The use of tensor products of trial

functions and the ensuing analysis of the (typically ill-conditioned) large sparse system of coefficients remains a relatively unexplored avenue.

The most widely used discretization schemes used to treat the angular dependence of the photon density in the radiative transport equation are the discrete ordinates method [14, 39] and the P_N-method [14, 23], though these are not the only methods, see [55] for example. The discrete ordinates method is a collocation method in angle due to Wick [59] and Chandrasekhar [16] while the P_N-method is a Galerkin spectral method due to Jeans [29]. In treating the generalized Fokker Planck equations of Chapter 3, the P_N-method is readily applicable to all of the models [44] while the discrete ordinates method requires model-specific adaptations to treat the scattering operators [32]. Additionally, the discrete ordinates method leads to strong coupling when treating the integral scattering operator through Gauss quadrature. The P_N-method on the other hand treats the scattering operator without coupling the expansion coefficients of the Legendre series. Moreover, the P_N-method is applicable to any scattering theory provided the eigenfunctions of the scattering operator are the spherical harmonics. It is for these reason that we pursue calculations of the photon density in the semi-infinite slab using the P_N-method.

In the next section a general overview of Galerkin methods is presented. We then apply the P_N- method in detail to the RTE for the case of infinite plane wave illumination.

4.2 The Galerkin Spectral Method in Detail

Suppose we have an equation of the form

$$\frac{\partial}{\partial t}u(t,x) = \mathcal{M}[u(t,x)] \quad \text{s.t } (t,x) \in [0,T] \times D, \tag{4.1}$$

with $[0, T]$ the time interval and D the spatial domain s.t. $D \subset R$. For simplicity we assume D is $(0, L)$ with $L > 0$. $\mathcal{M}[u(t, x)]$ is an operator of linear or nonlinear type that encompasses spatial derivatives of the solution, u. We assume suitable boundary and initial conditions on u are specified.

In a Galerkin method the solution u is approximated as the projection onto a set of complete orthogonal polynomials over $(0, L)$. We denote these polynomials $\phi_k(x)$, and assume their orthogonality with respect to the weighted inner product

$$\int_0^L w(x)\phi_k(x)\phi_{k'}(x)\mathrm{d}x = \delta_{kk'}. \tag{4.2}$$

The projection of u onto the set of polynomials, ϕ_k is then

$$u(t, x) = \sum_{k=0}^{\infty} \hat{u}_k(t)\phi_k(x), \tag{4.3}$$

with

$$\hat{u}_k(t) = \int_0^L w(x)u(t, x)\phi_k(x)\mathrm{d}x. \tag{4.4}$$

Ultimately, the infinite sum in (4.5) must be truncated for some $k = N$. This truncation is denoted

$$u^N(t, x) = \sum_{k=0}^{N} \hat{u}_k(t)\phi_k(x) \tag{4.5}$$

The degree to which u^N approximates u is well studied for specific model problems [12]. For instance if u is continuous, periodic, and of bounded variation on $(0, L)$, then u^N is uniformly convergent to u on $(0, L)$. The situation improves beyond uniform convergence if u and u^N possess greater regularity. Specifically if u is m-times continuously differentiable, $m \geq 1$, in $(0, L)$ and if $u^{(j)}$ is periodic for all $j \leq m-2$ then $\hat{u}_k = \mathcal{O}(k^{-m})$, speeding up the convergence of the series (4.5). We refer to Chapters 5 and 6 of [12] for rigorous details.

Upon substitution of u^N into the generic model problem (4.1) we define the residual

$$\frac{\partial}{\partial t}u^N(t, x) - \mathcal{M}[u^N(t, x)] = 0. \tag{4.6}$$

If we apply (4.6) pointwise in (t, x) we enforce the strong form of (4.1). In contrast, the Galerkin approximation is obtained by selecting a test function T_k and requiring

$$\int_0^L \Big(\frac{\partial}{\partial t}u^N(t,x) - \mathcal{M}[u^N(t,x)]\Big)T_k \mathrm{d}x = 0, \quad k = 0, 1, 2, \ldots \tag{4.7}$$

This integral requirement is termed a discrete *weak* formulation as opposed to (4.6). The term weak results from the integration. In addition if one integrates by parts in (4.7), the regularity properties of T_k are increased by requiring their derivatives to be well defined, while the regularity of u^N is relaxed. Solutions to pde are often obtained in this way [22].

The test functions T_k are chosen to be the same as the trial functions in the Galerkin method so that orthogonality can be brought to bear. One obtains the system

$$\frac{\partial}{\partial t}\hat{u}_{k'} - M_{kk'}\hat{u}_{k'} = 0, \tag{4.8}$$

that is solved when supplemented with initial conditions. The matrix

$$M_{kk'} = \int_0^L w(x)\mathcal{M}[u^N(t,x)]\phi_{k'}\mathrm{d}x. \tag{4.9}$$

is in general sparse and couples the indices of the expansion coefficients $\hat{u}_{k'}$. The sparsity arises from the recursion relations for the spatial derivatives of the trial functions. Time dependence is typically handled through any number of finite-differencing methods including Runge-Kutta and Adams-Bashforth schemes [12] or matrix exponentiation [41].

With an understanding of the general mechanics of the spectral Galerkin method, the machinery of the method is brought to bear on the steady state RTE describing the illumination of a semi-infinite half space subject to plane wave illumination. The Galerkin method is used as a piece of a composite method consisting of a normal mode expansion in the depth dependence, z. The trial

functions of the Galerkin approximation will ultimately be Legendre Polynomials though a preliminary analysis using spherical harmonics is a necessary first step. The great utility of the Galerkin method using Legendre polynomials to treat the directional dependence of the RTE is in its ability to treat arbitrary scattering operators provided they possess spherical harmonics as eigenfunctions.

4.3 P_N-Method Applied to the General Transport Problem

Having discussed the RTE and generalized Fokker-Planck models of interest in §3.3, we now dicuss a general framework in which numerical solutions to each of them can be obtained using a composite Galerkin spectral method. We begin by specifying the time-independent transport problem in the semi-infinite slab with a general scattering operator, $\mathcal{L}[\cdot]$,

$$(\mu\partial_z + \sigma_a)\,\psi(\mu, z) = \mathcal{L}[\psi(\mu, z)],\ (\mu, z) \in [-1, 1] \times [0, L]. \tag{4.10}$$

The infinite plane-wave boundary conditions on the faces of the slab are

$$\psi(\mu, z = 0) = \delta(\mu - 1),\quad \mu \in [0, 1], \tag{4.11}$$

$$\psi(\mu, z = L) = 0,\quad \mu \in [-1, 0]. \tag{4.12}$$

The scattering operator $\mathcal{L}[\cdot]$ can be any of the scattering operators considered in §3.3 though one is of course not limited to these examples! *The only requirement of the scattering operator is that it possess spherical harmonics as eigenfunctions.* The method we outline consists of three steps: treating the z-derivative through an exponential ansatz (normal modes), expanding the remaining μ dependencies in spherical harmonics- and then performing some algebra to obtain an expansion in terms of Legendre polynomials. Lastly, the boundary conditions (4.11-4.12) are applied by collocation to solve for the expansion coefficients of the normal modes in z.

4.3.1 Normal mode expansion in z

The z-dependence of the radiance is addressed via z-exponential ansatz [14, 21], exploiting separability of the angular and spatial variables

$$\psi(\mu, z) = \phi(\mu)e^{\gamma z}. \tag{4.13}$$

We remark that Kim [33] and Asadzadeh [3] have both used Chebyshev polynomials to treat the z dependence. Upon substituting (4.13) into the general transport equation (4.10) we obtain the following eigenvalue problem

$$(\mu\gamma + \sigma_a)\,\phi(\mu) = \mathcal{L}[\phi(\mu)],\ \ \mu \in [-1, 1]. \tag{4.14}$$

In the next section this differential equation will be reduced to a set of algebraic relations after expanding the angular dependence in Legendre polynomials.

4.3.2 Expansion in (spherical harmonics) Legendre polynomials

To begin, we replace μ by $\omega\cdot\hat{k}$ in the eigenvalue problem (4.14). Then $\phi(\omega\cdot\hat{k})$ is expanded in spherical harmonics on both sides of (4.14). We concentrate on the rhs of (4.14) to elucidate the generality of the method as it applies to different scattering operators. We have

$$\mathcal{L}[\phi(\omega\cdot\hat{k})] = \mathcal{L}\left[\sum_{n=0}^{\infty}\sum_{m=-n}^{+n}\hat{\phi}_n Y_{nm}(\omega)Y_{nm}^*(\hat{k})\right], \tag{4.15}$$

where

$$\hat{\phi}_n = 2\pi\int_{-1}^{1}\phi(\mu)P_n(\mu)\mathrm{d}\mu. \tag{4.16}$$

We now operate with $\mathcal{L}[\cdot]$ on $Y_{nm}(\omega)$ in (4.15) keeping in mind

$$\mathcal{L}[Y_{nm}] = \lambda_n Y_{nm}, \tag{4.17}$$

where λ_n is given by any of the expressions in §3.4 depending on the choice of scattering operator $\mathcal{L}[\cdot]$. Substituting (4.17) into (4.15), substituting that result into

the rhs of (4.14) and applying the addition theorem gives the following equation for the Legendre expansion of $\phi(\mu)$

$$(\gamma\mu + \sigma_a)\sum_{n=0}^{\infty}\frac{2n+1}{4\pi}\hat{\phi}_n P_n(\mu) = \sum_{n=0}^{\infty}\frac{2n+1}{4\pi}\lambda_n\hat{\phi}_n P_n(\mu). \tag{4.18}$$

We note that the sums are infinite and the $\hat{\phi}_n$ cannot be determined for all n. Instead the sums are truncated at some finite value $N-1$ (There are a total of N Legendre polynomials used, including $n=0$, hence the name P_N-method). Specifically

$$\phi(\mu) \cong \sum_{n=0}^{N-1}\frac{2n+1}{4\pi}\hat{\phi}_n P_n(\mu). \tag{4.19}$$

The P_N-method has been criticized because it has long been thought that the number N of Legendre polynomials needed to obtain accurate numerical solutions is restrictively large. While this may be true for the three dimensional RTE with no inherent symmetries, we will show this not to be the case for the semi-infinite slab problem with azimuthal symmetry considered here.

As described in the previous section, the Galerkin method is made complete by enforcing the equation (4.18) via integration against a test function, chosen here to be the Legendre polynomials. The integration against $P_k(\mu)$ requires some recursion relations that we omit by referring the reader to [14] for an explanation of the steps involved. This integration results in the following set of algebraic constraints that couple only three of the Legendre coefficients, $\hat{\phi}_k$

$$\frac{\gamma}{2k+1}\left[k\hat{\phi}_{k-1} + (k+1)\hat{\phi}_{k+1}\right] + (\sigma_a - \lambda_k)\hat{\phi}_k = 0 \quad \text{for } k = 0, 1, \ldots, N-1. \tag{4.20}$$

We rewrite the above in matrix form

$$(\gamma A + D)\,\hat{\phi} = 0 \quad \text{or} \quad -A^{-1}D\hat{\phi} = \gamma\hat{\phi}. \tag{4.21}$$

where $\hat{\phi}$ is now a vector of Legendre coefficients, $\hat{\phi} = (\hat{\phi}_0, \hat{\phi}_1, \ldots, \hat{\phi}_{N-1})^T$, and the

$N \times N$ matrices A and D have the following structure

$$A = \begin{pmatrix} 0 & 1 & 0 & 0 & \cdot & 0 \\ 1/3 & 0 & 2/3 & 0 & \cdot & 0 \\ 0 & 2/5 & 0 & 3/5 & \cdot & 0 \\ \cdot & \cdot & \cdot & \cdot & \cdot & 0 \\ \cdot & \cdot & k/(2k+1) & 0 & (k+1)/(2k+1) & \cdot \\ \cdot & \cdot & \cdot & \cdot & \cdot & \cdot \\ \cdot & \cdot & \cdot & \cdot & 0 & N/(2N-1) \\ 0 & 0 & 0 & 0 & N/(2N+1) & 0 \end{pmatrix} \tag{4.22}$$

$$D = \text{diag}(\sigma_a - \lambda_0, \sigma_a - \lambda_1, \ldots, \sigma_a - \lambda_{N-1}). \tag{4.23}$$

We remark that A is non-singular when $N-1$ is odd [21]. The eigenvalue problem (4.21) can now be solved for the N eigen-pairs $(\gamma, \hat{\phi})$.

4.3.3 Imposing boundary conditions

Following Kim and Keller [32], the solution to the general transport problem is represented as a superposition of normal modes

$$\psi(\mu, z) = \sum_{l=1}^{N/2} c_l \phi_l^+(\mu) e^{\gamma_l^+(z-L)} + \sum_{l=1}^{N/2} d_l \phi_l^-(\mu) e^{\gamma_l^- z}. \tag{4.24}$$

We note that the sums are finite as a result of our truncation of the sum of Legendre polynomials in μ. The number of Legendre modes determines the number of normal modes. The truncation of (4.19) at N results in N distinct normal modes. The eigenvalue problem (27) admits N/2 distinct eigen-pairs $(\gamma_l, \hat{\phi}_l)$ in which the eigenvalue $\gamma_l > 0$ for $l = 1, 2, \ldots, N/2$. We denote the eigenvalue then as γ_l^+ and the corresponding eigenvector as $\hat{\phi}_l^+$. Likewise there are $N/2$ negative eigenvalues and we denote these eigen-pairs as $(\gamma_l^-, \hat{\phi}_l^-)$. In this way we can split the sum over z-exponential modes as in (4.24). In general we observe that $-\gamma_l^+ = \gamma_l^-$ for each l.

This property emerges in the discrete ordinates method where it can be utilized in reducing the number number of computations necessary to produce numerical solutions [32]. Note that the vector of Legendre coefficients, $\hat{\phi}$, is now indexed by l corresponding to the eigenvalue $\gamma_l^{\pm}$. We thus denote $\hat{\phi}$ by $\hat{\phi}_l^{\pm}$ and note that this vector of coefficients is related to $\phi^{\pm}(\mu)$ through

$$\phi_l^{\pm}(\mu) \cong \sum_{n=0}^{N-1} \frac{2n+1}{4\pi} \hat{\phi}_{ln}^{\pm} P_n(\mu). \tag{4.25}$$

The coefficients c_l and d_l are furnished through the boundary conditions (4.11)-(4.12) by collocation in μ over [0, 1] at $z = 0$ and collocation in μ over [-1, 0] at $z = L$. This results in the system of equations

$$\psi(\mu_i, z=0) = \sum_{l=1}^{N/2} c_l e^{-\gamma_l^+ L} \phi_l^+(\mu_i) + \sum_{l=1}^{N/2} d_l \phi_l^-(\mu_i) = h(\mu_i),\ \mu_i \in [0,1], \tag{4.26}$$

$$\psi(\mu_i, z=L) = \sum_{l=1}^{N/2} c_l \phi_l^+(\mu_i) + \sum_{l=1}^{N/2} d_l e^{\gamma_l^- L} \phi_l^-(\mu_i) = 0,\ \mu_i \in [-1,0]. \tag{4.27}$$

The collocation points μ_i are chosen to be the zeros of the N^{th}-order Legendre polynomial[12], μ_i s.t. $P_N(\mu_i) = 0$.

4.3.4 Summary of the P_N-method: Numerical Procedure

To recap we overview the numerical procedure on a step-by-step basis.

(1) Specify the eigenvalues, λ_n, of the scattering operator of interest when acting on the spherical harmonics, see § 3.3. These eigenvalues may be determined analytically, as in the case of the FPE and MLLE, or using Gauss-Legendre quadrature- as in the RTE with **any** phase function dependent only on $\omega \cdot \omega'$. These eigenvalues populate the diagonal matrix D in (4.21).

(2) Solve the eigenvalue problem (4.21) for the eigen-pairs $(\gamma_l^-, \hat{\phi}_l^-)$ and $(\gamma_l^+, \hat{\phi}_l^+)$.

(3) Solve (4.26), (4.27) for the coefficients c_l and d_l.

The backscattered light distribution at $z = 0$ can then be constructed according to (4.26), using collocation points in [-1, 0]. Similarly for the transmission, (4.27) can be used however with collocation point in [0,1]. For completeness we report these expressions

Backscatter

$$\psi(\mu_i, z = 0) = \sum_{l=1}^{N/2} c_l e^{-\gamma_l^+ L} \phi_l^+(\mu_i) + \sum_{l=1}^{N/2} d_l \phi_l^-(\mu_i), \quad \mu_i \in [-1, 0], \tag{4.28}$$

Transmission

$$\psi(\mu_i, z = L) = \sum_{l=1}^{N/2} c_l \phi_l^+(\mu_i) + \sum_{l=1}^{N/2} d_l e^{\gamma_l^- L} \phi_l^-(\mu_i), \quad \mu_i \in [0, 1]. \tag{4.29}$$

Results for (4.28), (4.29) are presented in Chapter 6 for scattering given by the Henyey-Greenstein phase function and the various GFPE for values of anisotropy in the tissue-optics range. The angular boundary condition is a Gaussian of the form

$$h(\mu) = \frac{1}{l_s\sqrt{2\pi}} e^{-(\mu-1)^2/4l_s^2}. \tag{4.30}$$

In the next chapter the convergence properties of the P_N-method are investigated.

4.4 Summary

Spectral methods, with an emphasis on Galerkin methods, were introduced. The P_N-method was demonstrated to be a Galerkin type spectral method and can used in combination with a normal mode expansion to solve the depth and angle dependent RTE. The P_N-method is applicable to any scattering operator provided the eigenfunctions of the scattering operator are the spherical harmonics. Three term coupling of the expansion coefficients was observed. The P_N-method

provides the same amount of coupling regardless of the scattering operator used. For this reason, the P_N-method can be used as a tool to explore different tissue-light interactions without recourse to model-specific numerical methods.

In the next chapter the converge rate of the solutions is investigated as the number of Legendre polynomials used in the calculation is increased and as the anisotropy ranges through the tissue-optics range: $g \in [0.7, 1)$. As well, the effect of increasing the number of polynomials kept in the solution on the computation time to produce solutions is explored. It will be seen that the time required to solve the depth and angle dependent problem is conducive to multiple side-by-side comparisons of transport equations with varied tissue-light interactions. In Chapter 6 solutions to the RTE with Henyey-Greenstein phase function are compared to the generalized Fokker-Planck models considered in Chapter 3.

Chapter 5

Convergence Properties of the P_N-method

5.1 Introduction

In this chapter we investigate the impact of the truncation order of the Legendre polynomial series, (4.25), and hence normal mode expansion, (4.24), on the relative error of solutions of the transport equation, the time required to obtain these solutions, and the condition number associated with the matrix form of the boundary conditions, (4.26) and (4.27), used to obtain the expansion coefficients of the normal mode expansion. Additionally, the role anisotropy, g, plays in the convergence behavior is also investigated. The optimal truncation, n^*, for each scattering theory is identified for each g in the range $[0.7, 0.999]$, given a specified tolerance in the realtime error.

These results are of an empirical nature and no attempt at a theory of convergence, computation time, and condition number for the P_N-method is made. This appears to be an open problem of numerical analysis. In contrast, the convergence properties of the discrete ordinates method is well documented, see [30] for instance.

5.2 Definition of the Relative Error

Solutions to the transport problem obtained using different orders of truncation in the Legendre series (4.25) used to define the photon density in (4.24) are

expressed on different Gauss-Legendre points. For example, if the highest order Legendre polynomial used in a calculation is $N-1$, then the optimal grid points in μ are the zeros of the N^{th}-order Legendre polynomial: μ_i s.t. $P_N(\mu_i) = 0$ for $i = 1, 2, \ldots, N$ [12]. Resolving the solutions over any other grid, eg. a uniform grid, than the optimal quadrature points introduces oscillatory errors into the solutions [57].

Instead of comparing the solutions at different orders on a pointwise basis, we present the relative error in the calculation of the reflected current, R_n, termed reflectance, and transmitted current, T_n, termed transmittance, computed using n Legendre polynomials. These quantities are defined as direction space integrals in ω of the backscattered and transmitted radiance, respectively. In this way we circumvent the pointwise incompatibility of the solutions at different truncation orders. The reflectance and transmittance are computed using Gauss-Legendre quadrature [12] and are defined

$$R_n = -\int_{-1}^{0} \mu\psi_n(\mu, 0)\mathrm{d}\mu, \tag{5.1}$$

$$T_n = \int_{0}^{1} \mu\psi_n(\mu, L)\mathrm{d}\mu. \tag{5.2}$$

The relative error is defined

$$E_R(n, g) = \frac{|R_N - R_n|}{|R_N|}, \quad n = 2, 4, \ldots, N-2, \tag{5.3}$$

$$E_T(n, g) = \frac{|T_N - T_n|}{|T_N|}, \quad n = 2, 4, \ldots, N-2, \tag{5.4}$$

where the index N denotes the number of Legendre polynomials used in the highest order, and presumably most accurate, numerical solution of the RTE. The index n is the number of Legendre polynomials used in a lower order solution. The g dependence denotes the level of anisotropy of the material specified in the calculation. We recall that the anisotropy enters through the eigenvalues of the scattering operator, see (4.21), and influences the normal mode eigenvalues, γ, in

(4.24). We expect that as n approaches N,

$$\lim_{n\to N} E_R(n,g) = 0 \quad \lim_{n\to N} E_T(n,g) = 0. \tag{5.5}$$

Important questions are: How quickly does the convergence to zero occur? What role does anisotropy play in slowing down / speeding up the convergence? Are solutions with a desired tolerance of the relative error computable in a short enough amount of time? These questions are addressed in the subsequent sections.

5.3 Convergence of the Relative Error in Truncation Order, n

Figures 5.2 through 5.11 present the convergence profile of the RTE with Henyey-Greenstein phase function and the various generalized Fokker-Planck operators of Chapter 3 for strong levels of anisotropy: $g = 0.9,\ 0.99,\ 0.999$. Due to the singular nature of scattering as g tends to one, the need to include more Legendre polynomials in the solution is expected. We expect then that anisotropy slows down the convergence rate. Convergence in the presence of less anisotropy is explored in § 5.4.

In each of the Figures 5.2-5.11, a benchmark reflectance/transmittance using $N = 100$ Legendre polynomials is used. A semi-log-y scale is employed to infer the convergence rate of the relative error profiles. All of the plots were generated under the same material conditions: $\sigma_s = 100\ [\ \mathrm{cm}^{-1}],\ \sigma_a = 1\ [\ \mathrm{cm}^{-1}],\ L = 1\ [\mathrm{cm}]$.

One striking feature of Figures 5.2-5.11 is the non-constant rate of decay of the relative error. The local variations of the relative error possess minima that provide higher order accuracy at lower order truncations. A rather extreme example of this can be seen in the decay structure of the RTE with $g = 0.9$ in Figure 5.2, in which the $N = 46$ relative error is equal to that of the $N = 98$ relative error. This same behavior pervades most of the decay curves, albeit to a lesser degree.

Secondly, the decay rates exhibit a transition from a faster average rate of decay over part of the truncation range, typically $2 \leq n \leq 40$, to a slower average rate of decay over the remaining truncation range. An example of this can be seen in Figure 5.1 which displays the convergence profile of the relative error for the transmitted flux at the incident surface of a slab computed with the RTE with Henyey-Greenstein phase function. The average convergence behavior in the fast range is fitted on the semi-log-y scale with a line using a least squares procedure in Matlab [26]. The slower convergence is fitted with a second-order polynomial. In all of the profiles, the faster convergence in n is found to be proportional to exp(-αn). For Figure 5.1, $\alpha = 0.282$, with fast convergence over the range of truncation $2 \leq n \leq 44$. The slower convergence in n is found to be proportional to exp(-$\gamma n^2 + \delta n$) for all of the operators over roughly the second half of the truncation range. Exceptions to this are the profiles for the second modified Leakeas-Larsen operator whose convergence rate is slow ($\propto$ exp(-$\gamma n^2 + \delta n$)) for approximately 3/4 of the truncation interval. In Figure 5.1, slow convergence occurs over the range $48 \leq n \leq 98$ with $(\gamma, \delta) = (0.001974, 0.2262)$.

In Tables 5.1-5.2 the convergence behavior characterized by α for fast convergence of the relative error for both the reflected (Table 5.1) and transmitted (Table 5.2) flux at the surfaces of the slab for g=0.9, 0.99, and 0.999 are presented for each of the scattering operators. Additionally the maximum value n for which fast convergence occurs is also presented. These data are inferred from Figures 5.2-5.11 using the fitting process described for Figure 5.1. In general, the fit lines for fast convergence of the relative error suggest an exponential behavior in n though the convergence is slower than exp(-n). Exponential convergence is characteristic of spectral methods in general [12].

Both the local variations of the relative error and transition from fast to slow average convergence are advantageous to computation as both behaviors fa-

vor truncation of the Legendre series in the range $40 \leq n \leq 50$. This means less memory requirements and due to the pointwise implementation of boundary conditions, a smaller matrix to invert to find the normal mode expansion coefficients in (4.26) and (4.27), see § 5.7.

Lastly, we remark on certain shortcomings of the solutions obtained as indicated by the presence of slow convergence rates. Slow convergence is seen over all truncation orders in the second Modified Leakeas-Larsen equation for $g = 0.99$ and 0.999. The relative error 10^{-4} is obtainable only in the limit of keeping $N = 98$ Legendre modes for transmission and is unobtainable at $N = 98$ modes in reflection. The error does decay at a comparative rate to that of the RTE and standard Fokker-Planck operator for $g = 0.9$ in both reflection and transmission.

The slow convergence rate of solutions to the second modified Leakeas-Larsen equation is attributed to the slow convergence of the eigenvalues of this scattering operator to $-\sigma_s$ as n increases. By design, the second modified Leakeas-Larsen operator matches the highest order integral scattering operator eigenvalue, not $-\sigma_s$. See § 3.3.5. For instance, with $g = 0.99$ and $n = 20$, the $n = 20$ eigenvalue is $-100(1-0.99^{20}) = -18.209$ while the $n = 100$ eigenvalue is $-100(1-0.99^{20}) = -63.397$. These eigenvalues in turn change the spectra, γ_l, used in the normal mode expansion. This is in contrast to the first modified Leakeas-Larsen operator whose $n = 20$ and $n = 100$ eigenvalues are -67.96 and -98.077 respectively. These eigenvalues converge faster to $-\sigma_s$ and thus provide a similar set of eigenvalues λ_n used in the matrix equation (4.21) to determine the normal mode spectra γ_l in (4.24).

The standard Fokker-Planck operator in combination with the pseudo-differential operator $\mathcal{L}_{3/2}$ exhibits trouble converging at $g = 0.9$ for both transmitted and reflected fluxes, see Figures 5.9 and 5.10. This is attributed to the positivity of the eigenvalues λ_n of this operator at $g = 0.9$, see Figure 3.1. As g increases

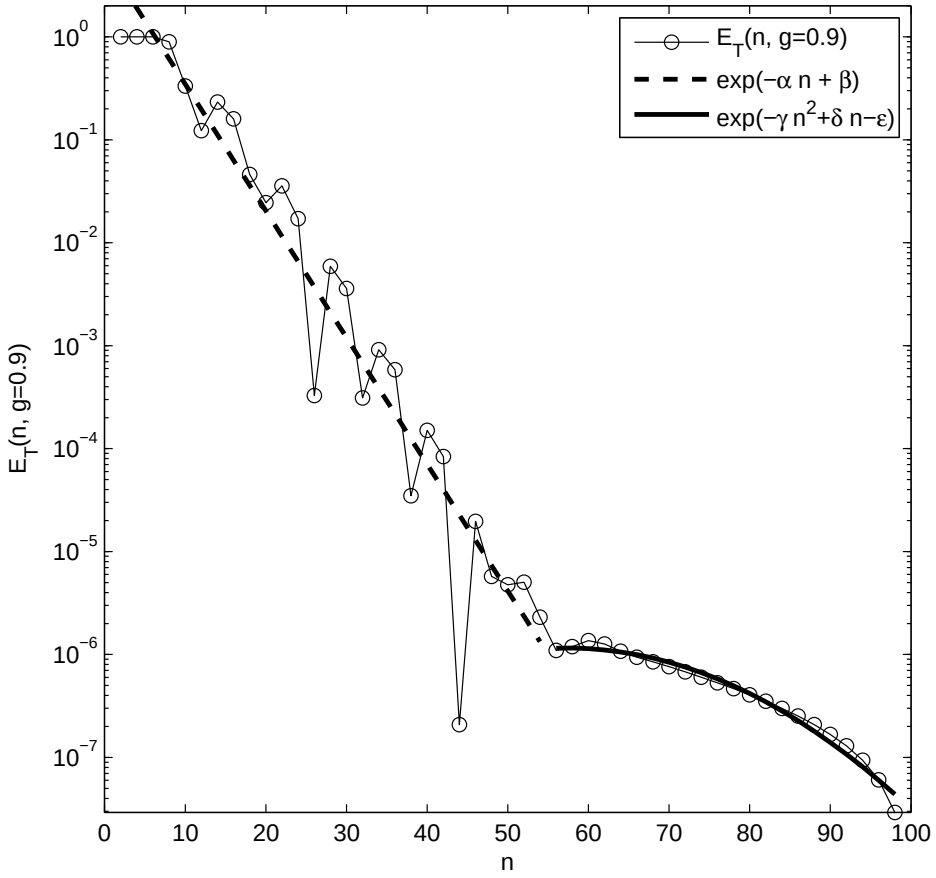

Figure 5.1: Convergence of the *transmitted* current computed using the RTE with HG phase function reported for g=0.9. The function exp(-$\alpha n + \beta$), $\alpha = 0.282$, (dashed) provides a fit of the faster convergence, with exp(-$\gamma n^2 + \delta n - \epsilon$), (γ, δ) = (0.001974, 0.2262), (solid) fitting the slower convergence.

	$g = 0.9$	$g = 0.99$	$g = 0.999$
RTE+H.G.			
α	0.2937 ± 0.0412	0.2525 ± 0.0219	0.25 ± 0.0296
n	46	46	38
F.P.			
α	0.2912 ± 0.0358	0.2825 ± 0.0433	0.1918 ± 0.0215
n	48	48	74
Mod. L.L.			
α	0.2745 ± 0.0287	0.2805 ± 0.0378	0.2096 ± 0.0274
n	50	50	64
Mod. L.L.#2			
α	0.26 ± 0.0336	0.05934 ± 0.00457	0.05164 ± 0.00824
n	36	98	98
F.P. + $\mathcal{L}_{3/2}$			
α	-	0.2526 ± 0.0219	0.2563 ± 0.0322
n	2	46	36

Table 5.1: Reflected Flux: Convergence rate, α, with 95% confidence bounds, of the exponential decay of the relative error. The value n denotes the point at which the convergence rate becomes sub-exponential.

	$g = 0.9$	$g = 0.99$	$g = 0.999$
RTE+H.G.			
α	0.282 ± 0.0307	0.2766 ± 0.0348	0.2789 ± 0.0293
n	56	48	56
F.P.			
α	0.2835 ± 0.0247	0.2769 ± 0.0351	0.2899 ± 0.0253
n	56	48	60
Mod. L.L.			
α	0.2851 ± 0.0325	0.266 ± 0.0406	0.2906 ± 0.0254
n	48	42	58
Mod. L.L.#2			
α	0.2562 ± 0.0328	0.3264 ± 0.1619	0.2606 ± 0.0488
n	36	26	30
F.P. + $\mathcal{L}_{3/2}$			
α	-	0.2817 ± 0.0375	0.2789 ± 0.0293
n	2	48	54

Table 5.2: Transmitted Flux: Convergence rate, α, with 95% confidence bounds, of the exponential decay of the relative error. The value n denotes the point at which the convergence rate becomes sub-exponential.

away from 0.9, the eigenvalues of this operator become purely negative and the corresponding solution becomes more regular. This is evident in the decay rates at $g = 0.99$ and 0.999. In the next section, a more exhaustive study of the influence of the anisotropy factor on the convergence properties of the relative error is carried out over $g \in [0.7, 1)$.

5.4 Dependence of the Relative Error Convergence on Anisotropy Factor, g

The relative error is presented as a function of the anisotropy factor g for various truncation values, n, in figures 5.12-5.21. The most desirable dependence of the relative error on g would be a weak dependence as g tends towards one, where more Legendre modes are required to describe the forward-scattering behavior of the photons.

Weak dependence indeed predominates for the RTE with Henyey-Greenstein phase function, Figures 5.12-5.13, the standard Fokker-Planck operator, Figures 5.14-5.15, and the modified Leakeas-Larsen equation, Figures 5.16-5.17. One peculiar property is the existence of anisotropy factors that give rise to local minima in the relative error. See Figures 5.13, 5.15, and 5.17. This "resonant" behavior occurs systematically for $N = 60, 80$ and only for the transmitted flux. A suitable explanation for this behavior has not been found.

Figure 5.
Planck o

Lastly we remark the large growth in error, as g tends to one, present in the second modified Leakeas-Larsen profiles, Figures 5.18 and 5.19. This is attributed to the change in the 'local asymptotic eigenvalue' mentioned in § 3.3.5 and the previous section. The opposite behavior occurs for the Fokker-Planck operator in combination with the pseudo-differential operator, $\mathcal{L}_{3/2}$. The eigenvalues of this operator become purely negative as (1-g) approaches zero and the solutions become more regular. The accuracy of this operator improves as g tends to 1.

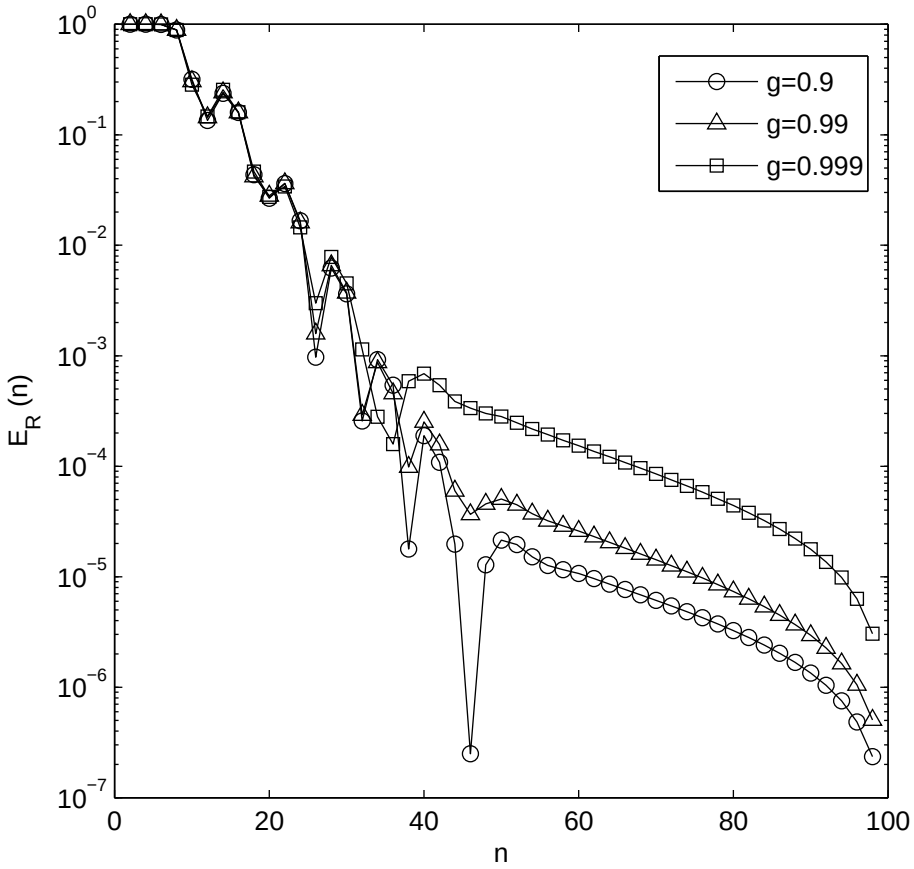

Figure 5.2: Convergence of the *reflected* current computed using the RTE with HG phase function reported for g=0.9 (circles), g=0.99 (triangles), g=0.999 (squares).

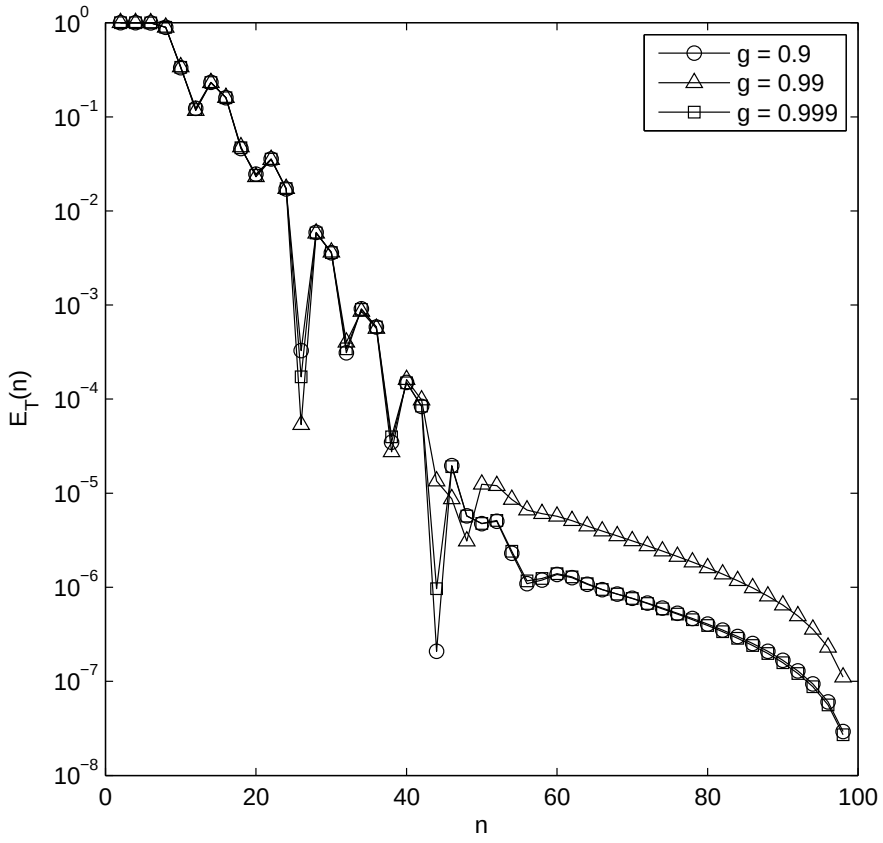

Figure 5.3: Convergence of the *transmitted* current computed using the RTE with HG phase function reported for g=0.9 (circles), g=0.99 (triangles), g=0.999 (squares).

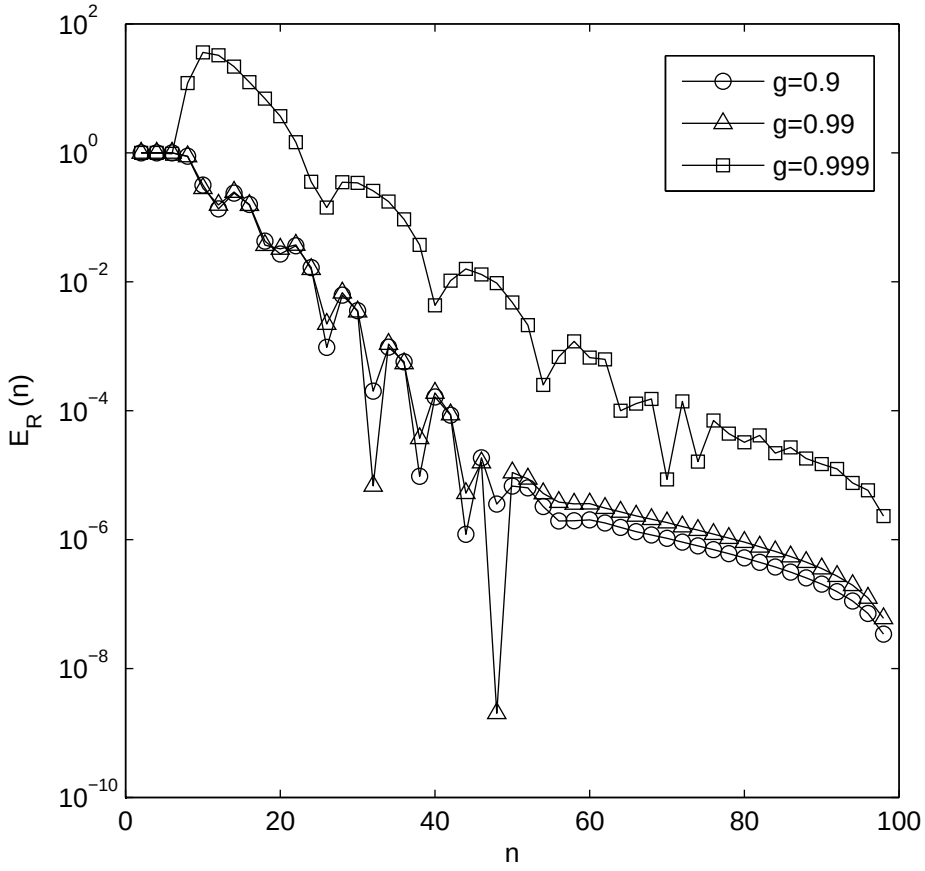

Figure 5.4: Convergence of the *reflected* current computed using the standard Fokker-Planck equation reported for g=0.9 (circles), g=0.99 (triangles), g=0.999 (squares).

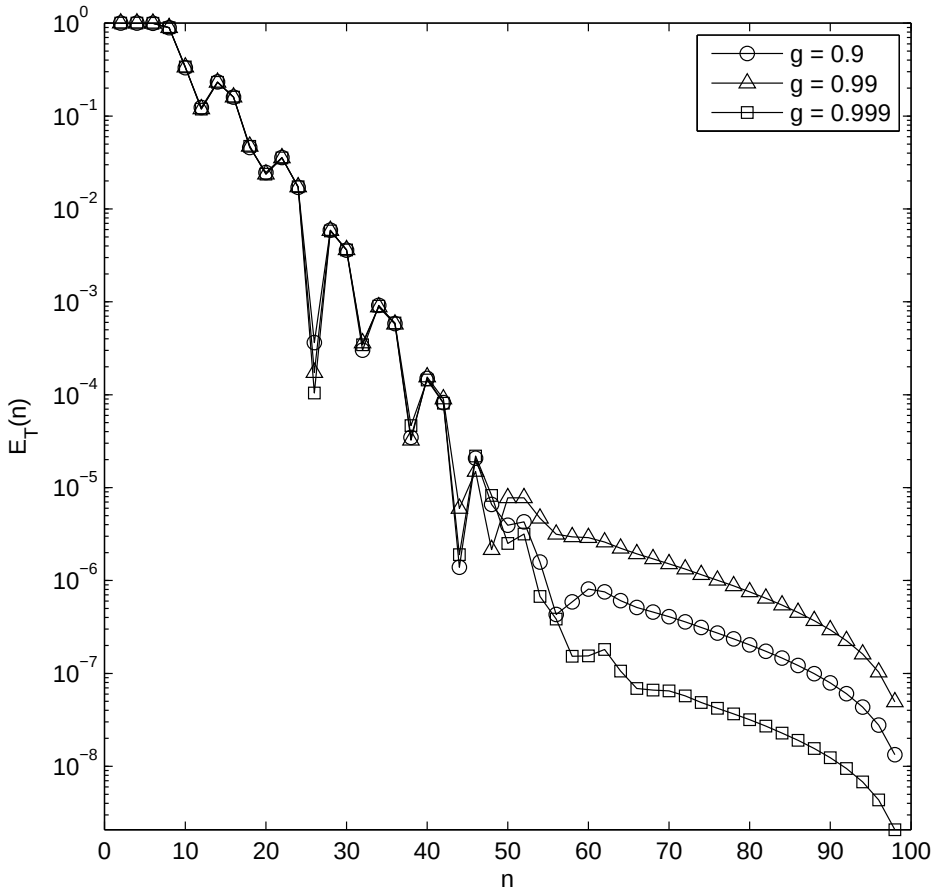

Figure 5.5: Convergence of the *transmitted* current computed using the standard Fokker-Planck equation reported for g=0.9 (circles), g=0.99 (triangles), g=0.999 (squares).

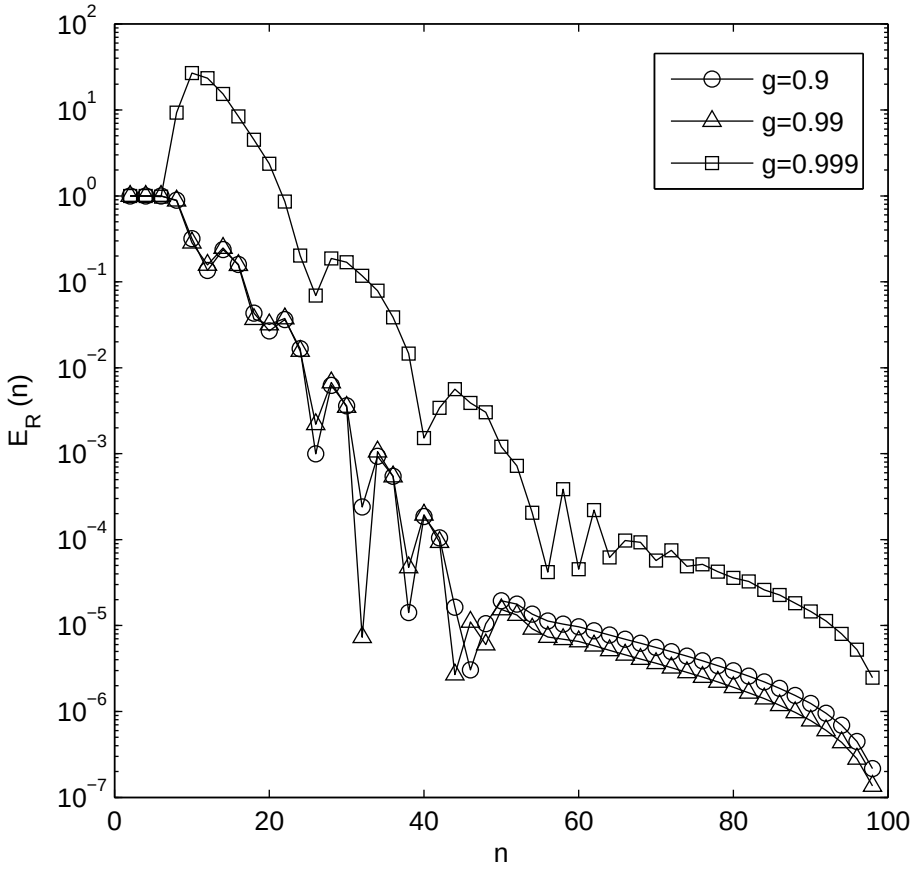

Figure 5.6: Convergence of the *reflected* current computed using the modified Leakeas-Larsen equation reported for g=0.9 (circles), g=0.99 (triangles), g=0.999 (squares).

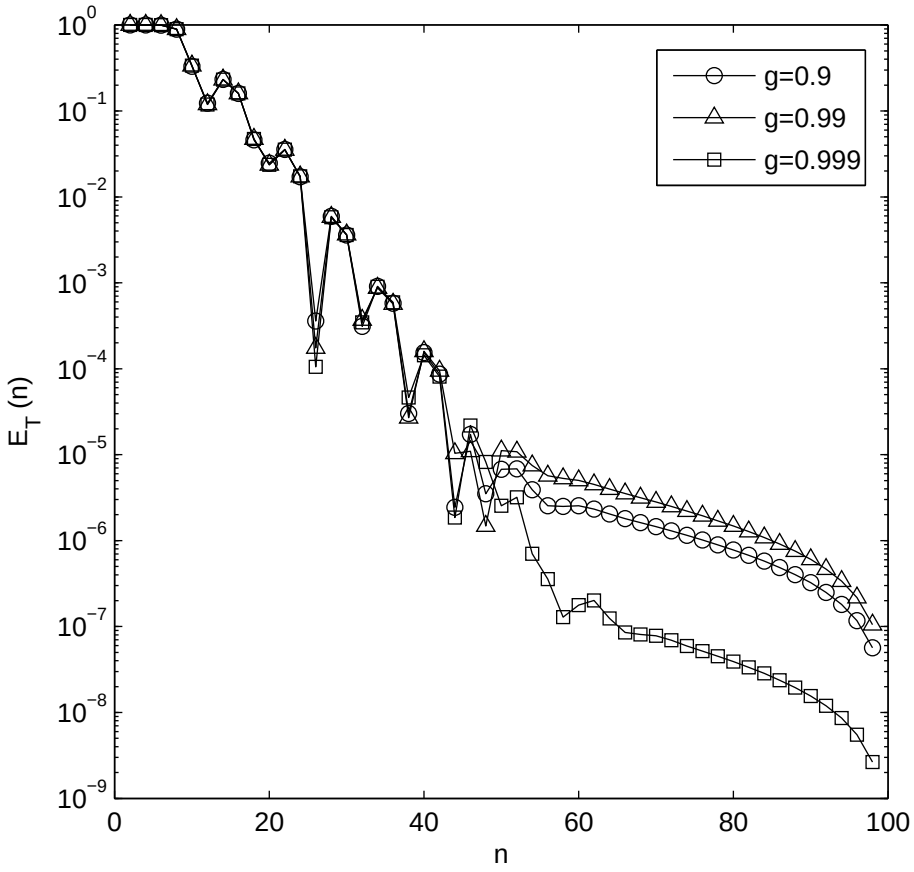

Figure 5.7: Convergence of the *transmitted* current computed using the modified Leakeas-Larsen equation reported for g=0.9 (circles), g=0.99 (triangles), g=0.999 (squares).

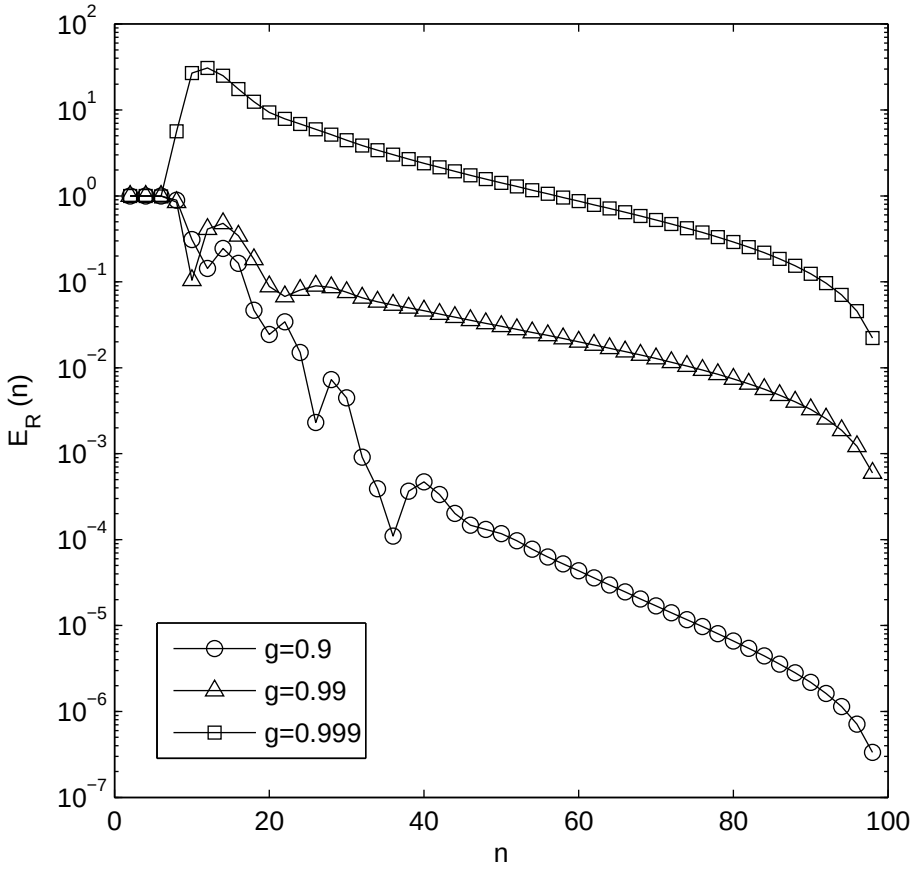

Figure 5.8: Convergence of the *reflected* current computed using the second modified Leakeas-Larsen equation reported for g=0.9 (circles), g=0.99 (triangles), g=0.999 (squares).

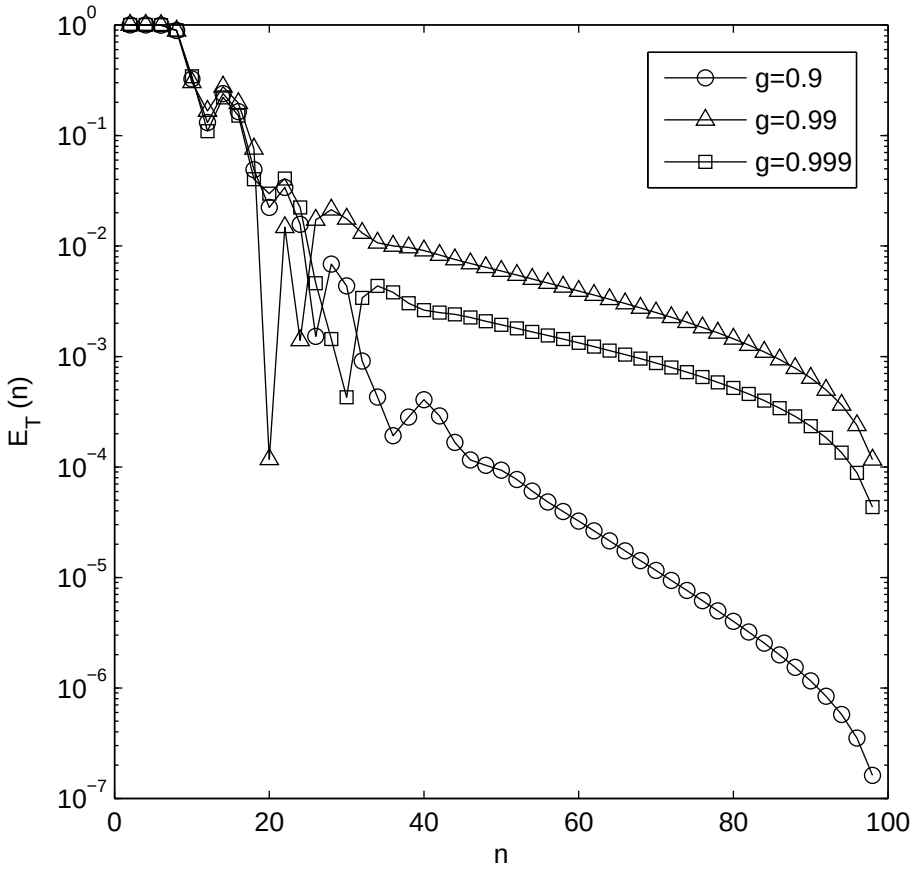

Figure 5.9: Convergence of the *transmitted* current computed using the second modified Leakeas-Larsen equation reported for g=0.9 (circles), g=0.99 (triangles), g=0.999 (squares).

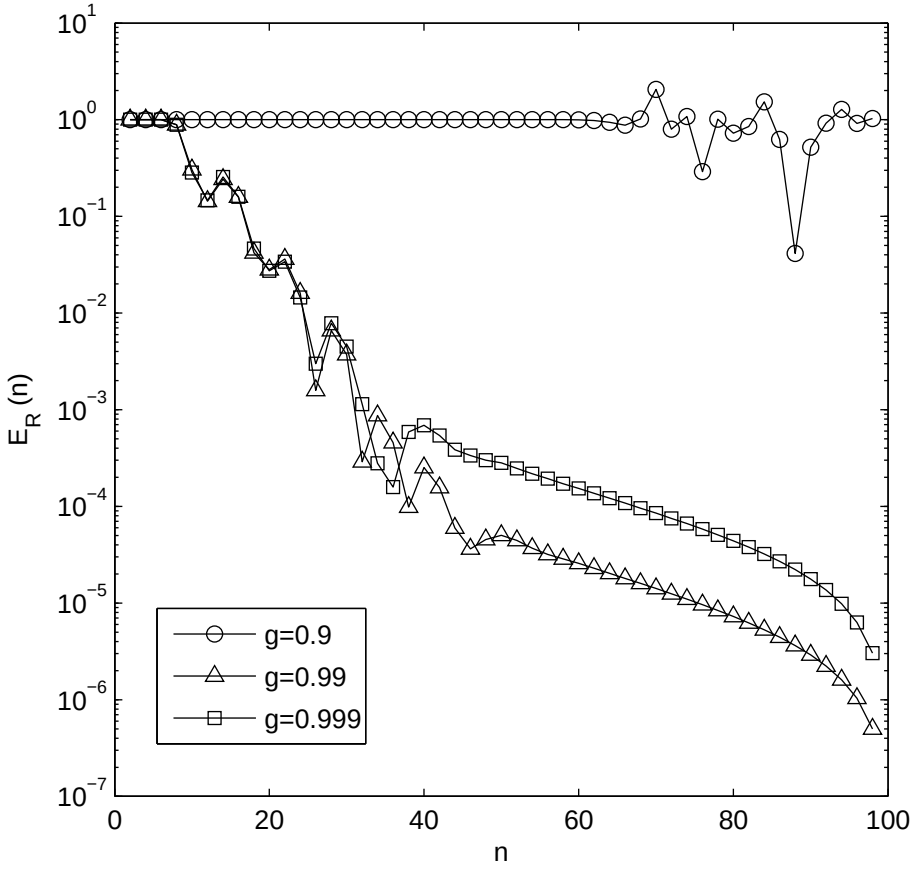

Figure 5.10: Convergence of the *reflected* current computed using the Fokker-Planck + $\mathcal{L}_{3/2}$ operator reported for g=0.9 (circles), g=0.99 (triangles), g=0.999 (squares).

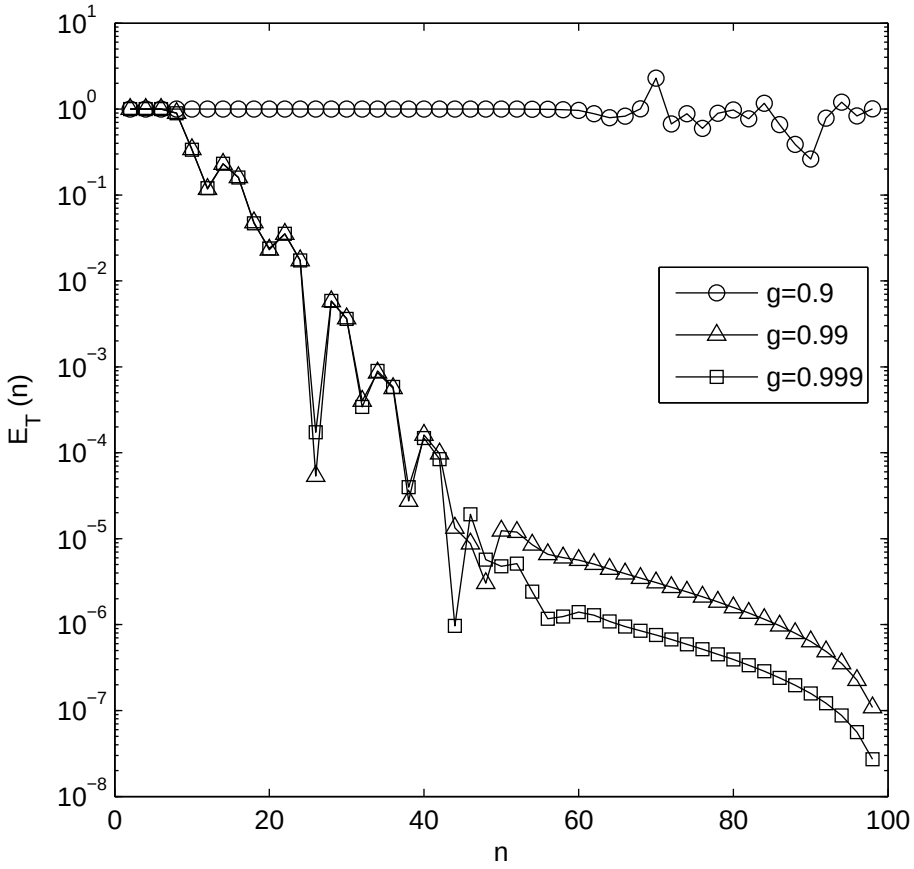

Figure 5.11: Convergence of the *transmitted* current using the Fokker-Planck + $\mathcal{L}_{3/2}$ operator reported for g=0.9 (circles), g=0.99 (triangles), g=0.999 (squares).

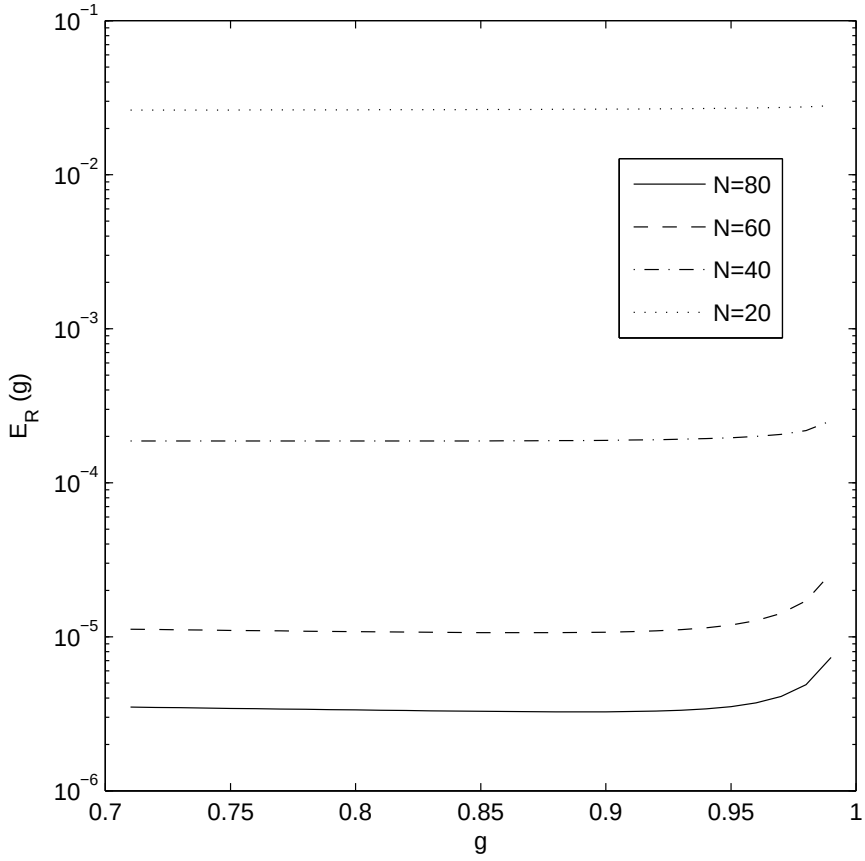

Figure 5.12: Convergence of the *reflected* current for RTE with HG phase function reported for $N = 20$, 40, 60, 80.

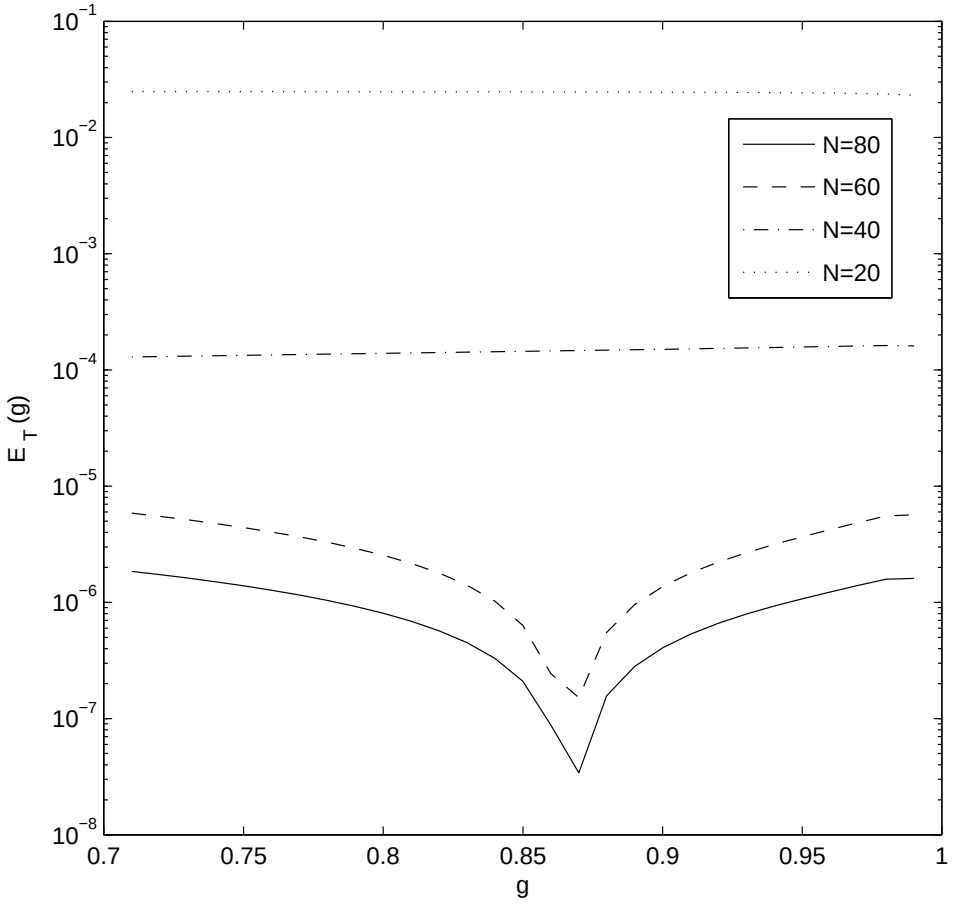

Figure 5.13: Convergence of the *transmitted* current for RTE with HG phase function reported for $N = 20, 40, 60, 80$.

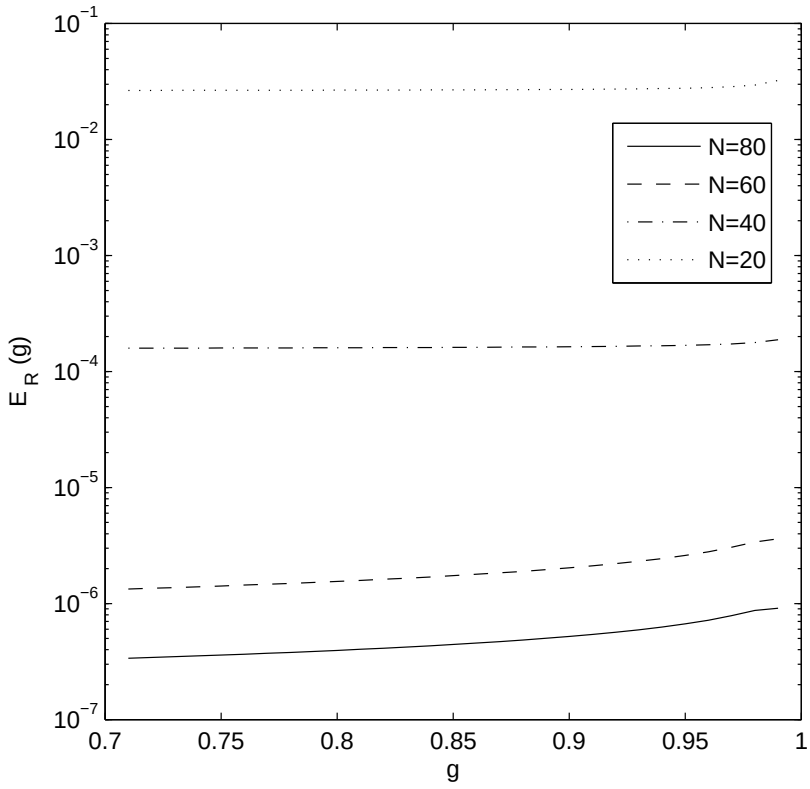

Figure 5.14: Convergence of the *reflected* current computed using the standard Fokker-Planck equation reported for $N = 20, 40, 60, 80$.

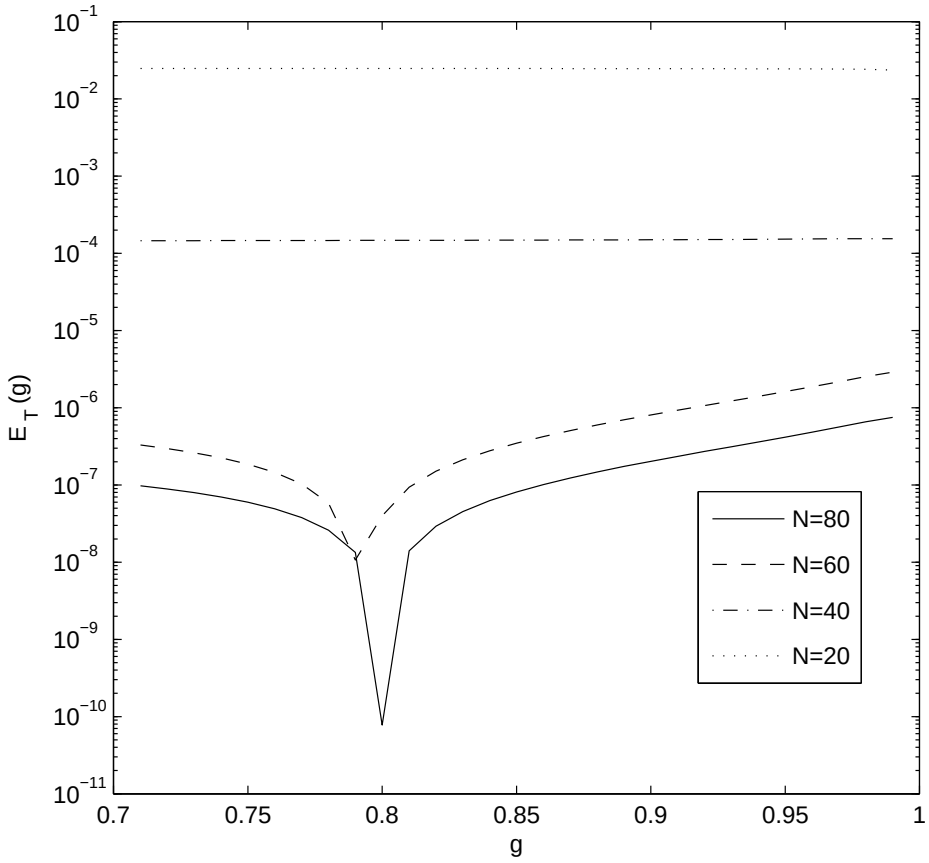

Figure 5.15: Convergence of the *transmitted* current computed using the standard Fokker-Planck equation reported for $N = 20, 40, 60, 80$.

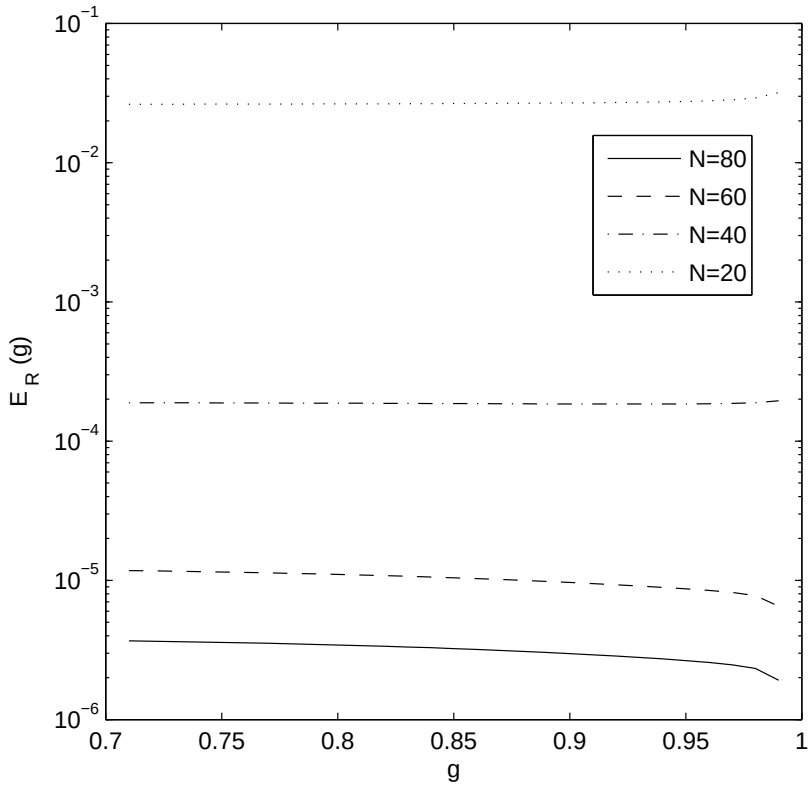

Figure 5.16: Convergence of the *reflected* current computed using the modified Leakeas-Larsen equation reported for $N = 20, 40, 60, 80$.

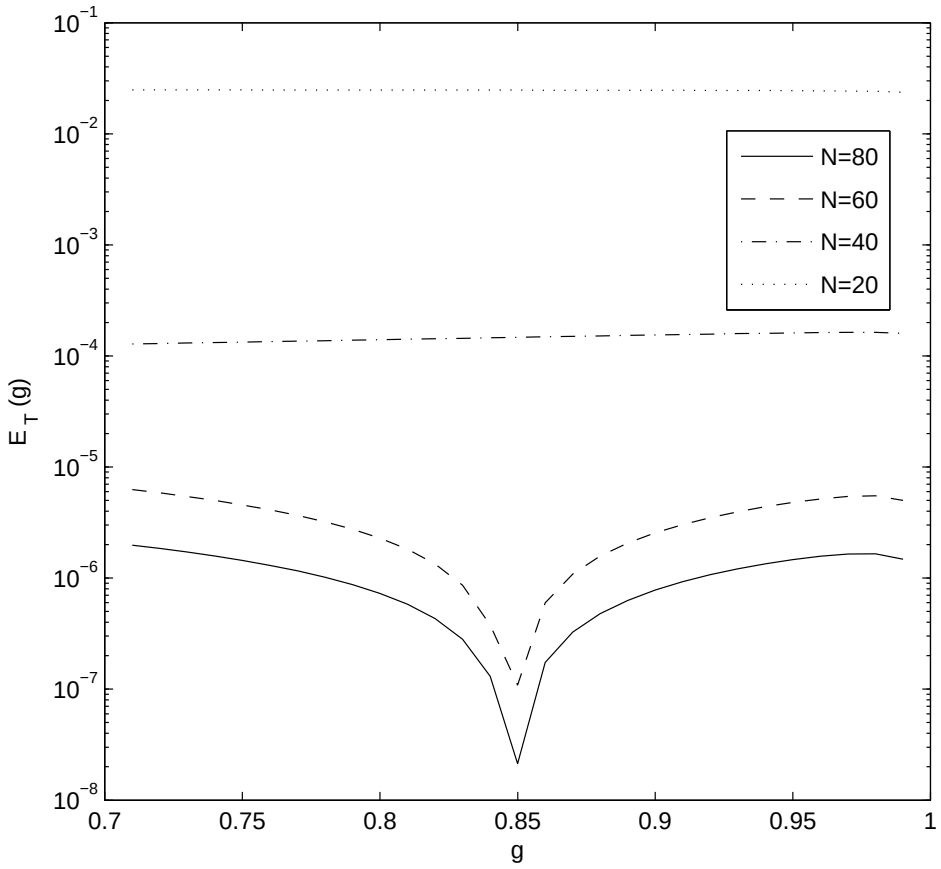

Figure 5.17: Convergence of the *transmitted* current computed using the modified Leakeas-Larsen equation reported for N =20, 40, 60, 80.

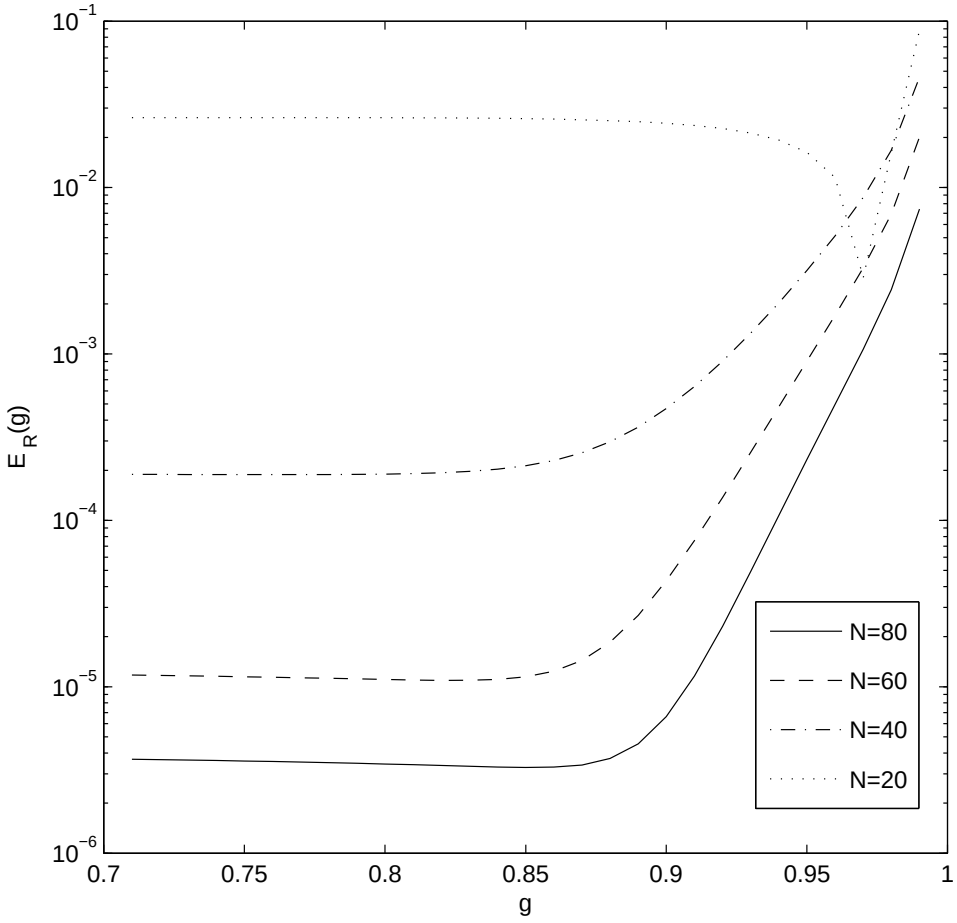

Figure 5.18: Convergence of the *reflected* current computed using the second modified Leakeas-Larsen equation reported for $N = 20, 40, 60, 80$.

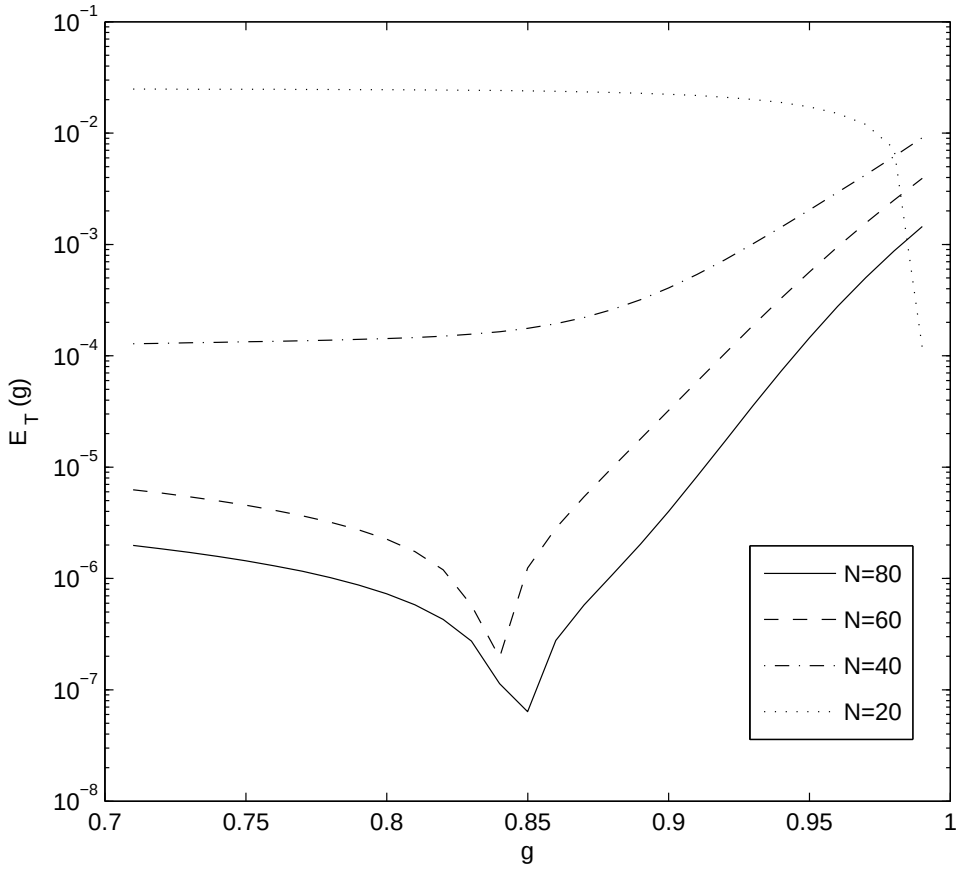

Figure 5.19: Convergence of the *transmitted* current computed using the second modified Leakeas-Larsen equation reported for $N = 20$, 40, 60, 80.

5.5 Optimal Truncation Order, n^*, for each g

In Figures 5.22-5.26 the optimal truncation order is found for each scattering model for the reflected and transmitted flux over the range of anisotropies $g \in [0.7, 1)$. The criteria for choosing an optimal operational value of the Legendre truncation, denoted n^*, should provide a good compromise between accuracy and computational requirements. Though, as we will see in the next section, the computation time associated with truncation in n even at $n = 100$ is not at all prohibitive of prompt side-by-side comparisons of scattering theories. However, we would still like to do the least amount of work possible!

The optimal truncation order, n^*, is determined by specifying a tolerance, `TOL`, such that when $n = n^*$

$$E_R(n^*, g) \leq \texttt{TOL}, \tag{5.6}$$

$$T_R(n^*, g) \leq \texttt{TOL}. \tag{5.7}$$

In Figures 5.22-5.26 `TOL` is set to 10^{-3} and 10^{-4} for both the reflected and transmitted flux. n^* is found to be below 40 for the integral scattering operator, the Fokker-Planck operator, and modified Leakeas-Larsen operator for both tolerances. For the second modified Leakeas-Larsen operator and the Fokker-Planck operator in combination with $\mathcal{L}_{3/2}$, both require many more modes to account for reflection than transmission. This suggests that these operators are better suited for small angle scattering calculations. The second modified Leakeas-Larsen equation is unable to obtain a relative error of 10^{-4} for $n \leq 100$.

5.6 Computation Time

In Figure 5.27 we illustrate the time required to compute solutions to the linear transport equation as the number of Legendre modes used in the solution

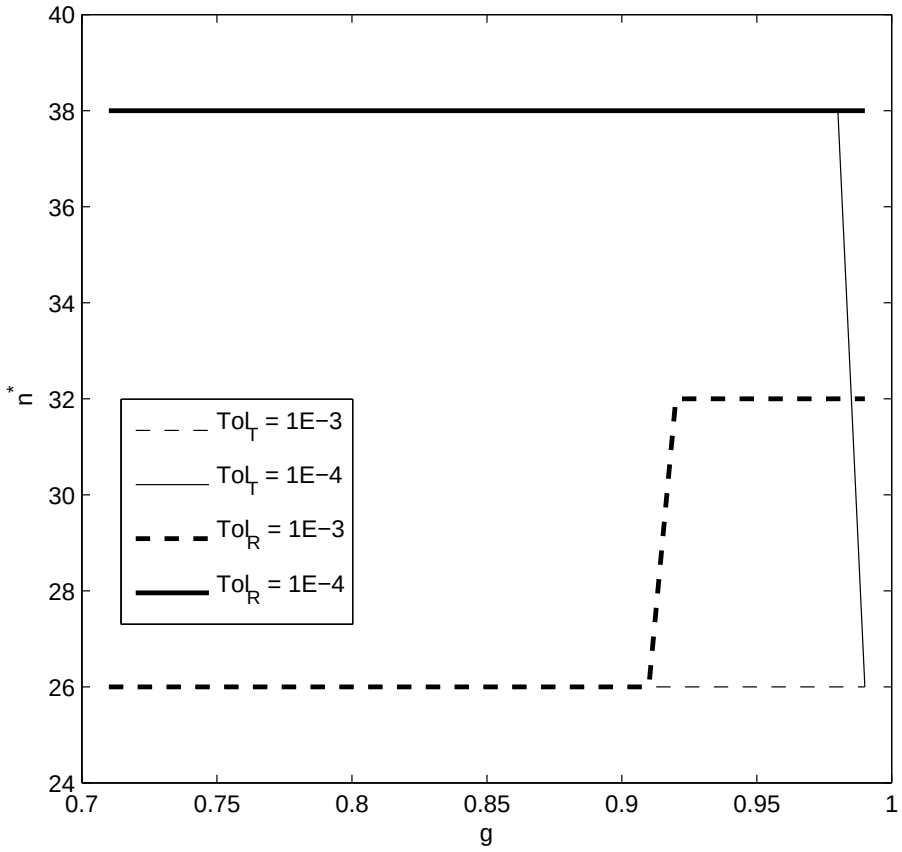

Figure 5.22: Optimal truncation order, n^*, of the RTE determined for $g \in [0.7, 0.99]$ and for both the reflected (Tol_R = 1E-3, 1E-4) and transmitted (Tol_T = 1E-3, 1E-4) flux.

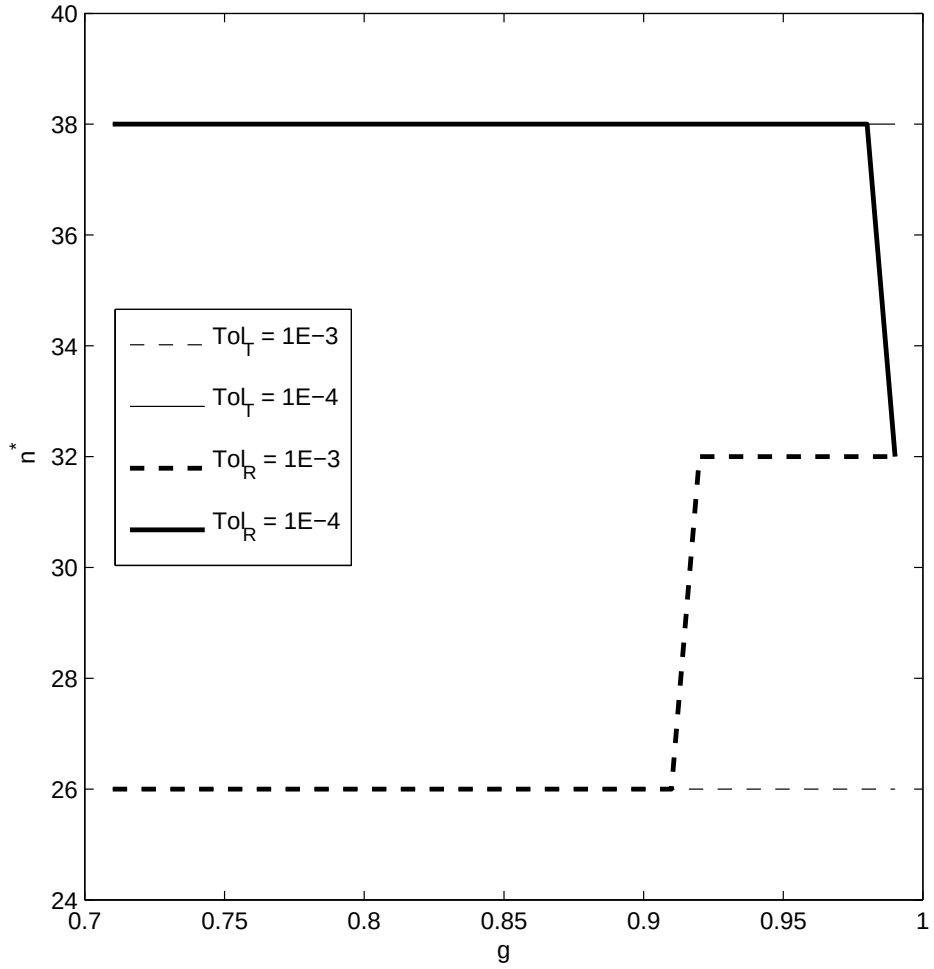

Figure 5.23: Optimal truncation order, n^*, of the Fokker-Planck equation determined for $g \in [0.7, 0.99]$ and for both the reflected (Tol_R = 1E-3, 1E-4) and transmitted (Tol_T = 1E-3, 1E-4) flux.

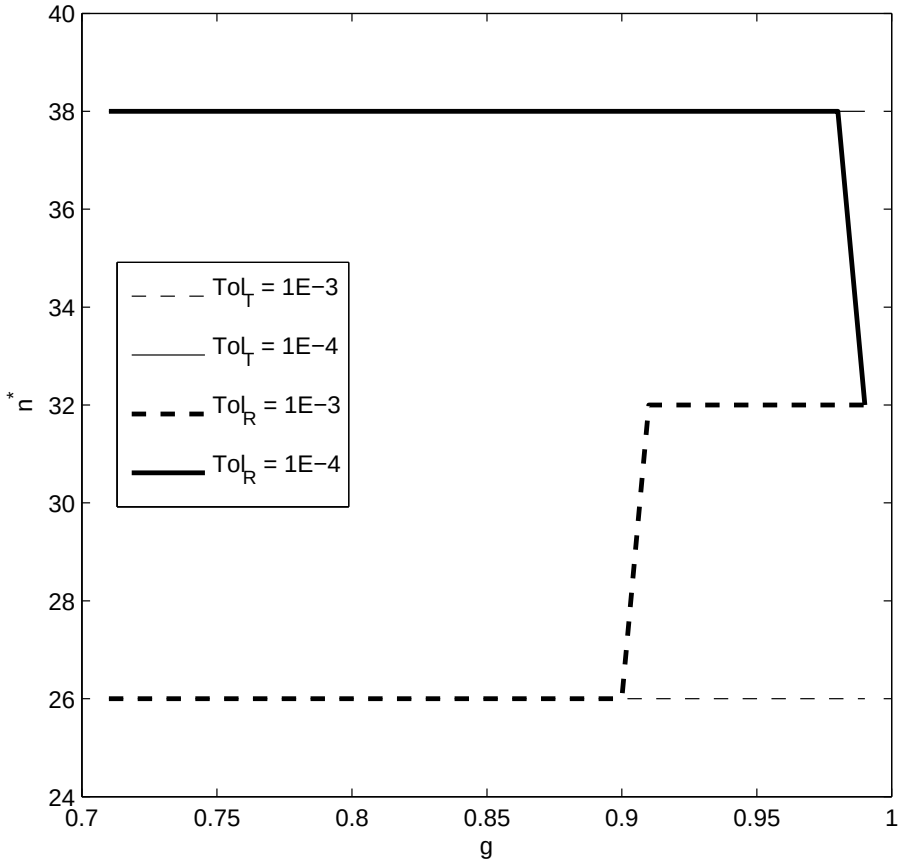

Figure 5.24: Optimal truncation order, n^*, of the modified Leakeas-Larsen equation determined for $g \in [0.7, 0.99]$ and for both the reflected (Tol_R = 1E-3, 1E-4) and transmitted (Tol_T = 1E-3, 1E-4) flux.

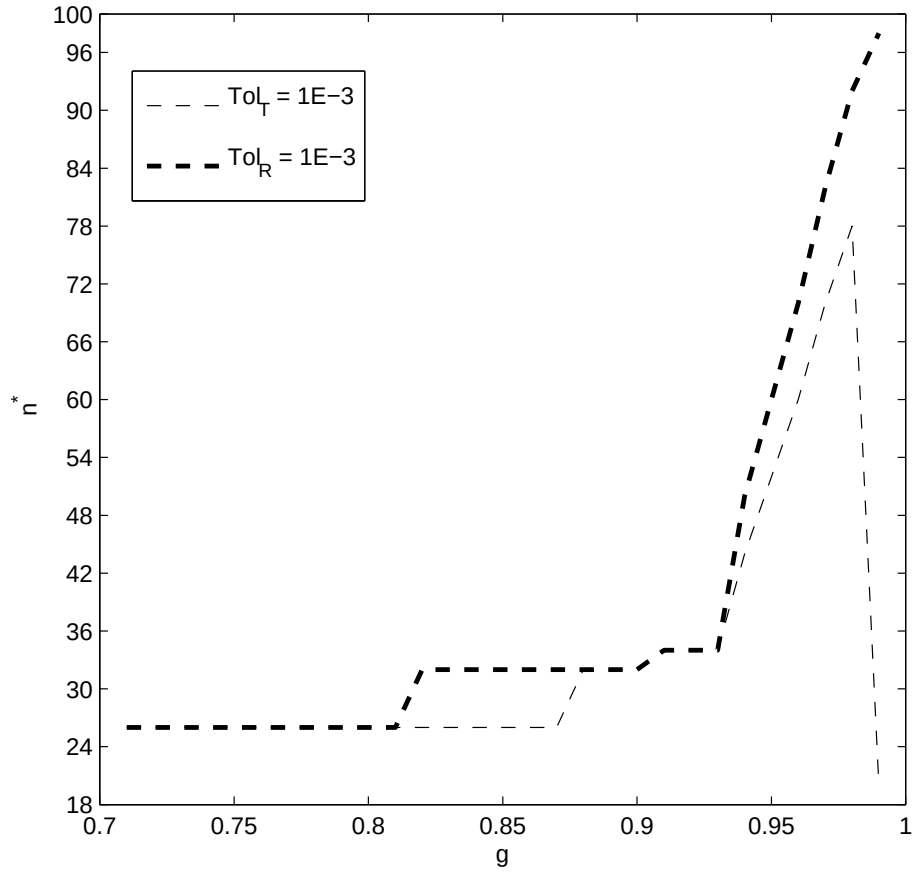

Figure 5.25: Optimal truncation order, n^*, of the second modified Leakeas-Larsen equation determined for $g \in [0.7, 0.99]$ and for both the reflected (Tol_R = 1E-3) and transmitted (Tol_T = 1E-3) flux. For this scattering theory, a tolerance level of 1E-4 is unobtainable for $n \leq 100$.

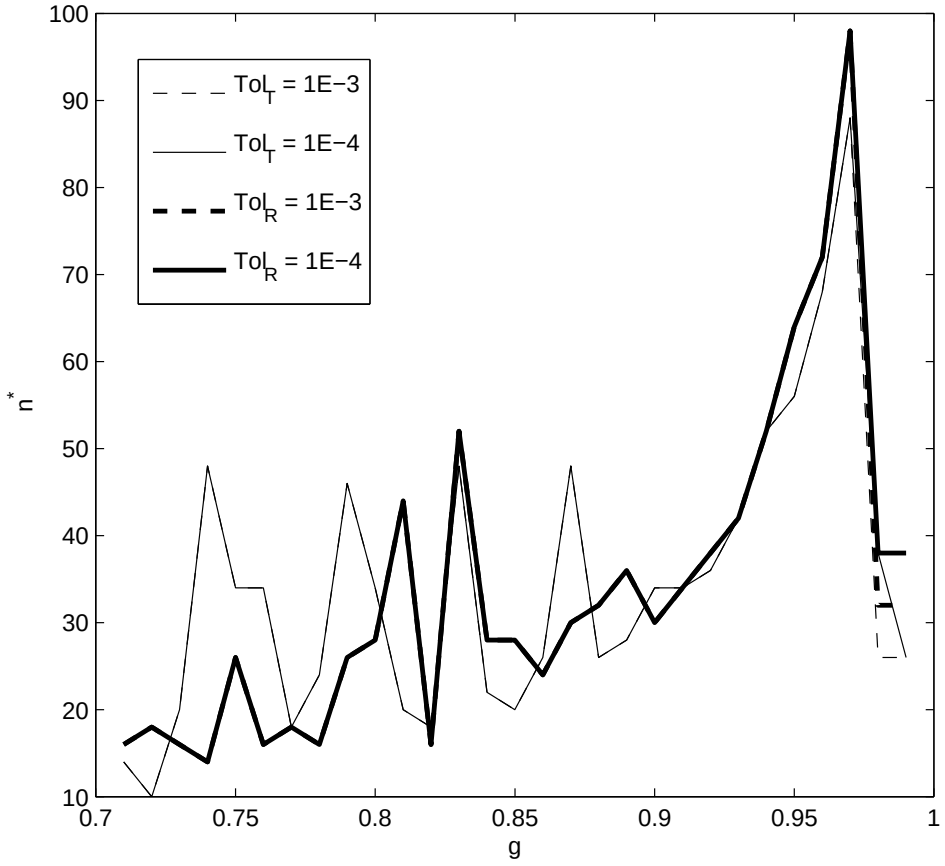

Figure 5.26: Optimal truncation order, n^*, of the Fokker-Planck operator + $\mathcal{L}_{3/2}$ operator determined for $g \in [0.98, 0.999]$ and for both the reflected (Tol_R = 1E-3, 1E-4) and transmitted (Tol_T = 1E-3, 1E-4) flux.

increases. Data for the RTE with Henyey-Greenstein phase function, the standard Fokker-Planck equation, and the modified Leakeas-Larsen equation are presented. The RTE time profile was generated under the assumption that we had not known $\hat{f}_n = g^n$ in the expression for the eigenvalues $-\sigma_s(1 - \hat{f}_n)$. Gaussian quadrature was used to determine the $\hat{f}_n$. Indeed, the RTE calculations are slower as a result of the Gauss quadrature needed to determine the eigenvalues, however, solutions are still quickly obtained, eg. 2.52 seconds for $n = 98$ Legendre polynomials. Both the FPE and MLLE eigenvalues are coded using their exact expressions given in §3.4 and take the same amount of time, eg. just over half a second for $n = 98$ Legendre polynomials. Computations were carried out on an Intel Dual Core machine.

Time requirements for the P_N-method are negligible for generating solutions with relative errors in the range 1E-4.

5.7 Condition Number of Boundary Condition Matrix

The last area of numerical concern is the determination of the normal mode expansion coefficients, see § 4.3.3. The coefficients are obtained through collocation in μ at the boundaries of the slab $z = 0$ and $z = L$. The boundary conditions at $z = 0$ and $z = L$ were introduced in (4.26) and (4.27), respectively, and admit the matrix form

$$\mathbf{V}\begin{pmatrix} \vec{c} \\ \vec{d} \end{pmatrix} = \begin{pmatrix} V_1 & V_2 \\ V_3 & V_4 \end{pmatrix}\begin{pmatrix} \vec{c} \\ \vec{d} \end{pmatrix} = \begin{pmatrix} \vec{h} \\ 0 \end{pmatrix}. \tag{5.8}$$

For $1 \leq l \leq N/2$ and $1 \leq k \leq N/2$, the sub-matrices V_i of $\mathbf{V}$ are defined

$$\{V_1\}_{lk} = \sum_{n=0}^{N-1} \frac{2n+1}{4\pi}\hat{\phi}^+_{ln}P_n(\mu_k)e^{-\gamma_l^+ L}, \quad \mu_k \in [0,1], \tag{5.9}$$

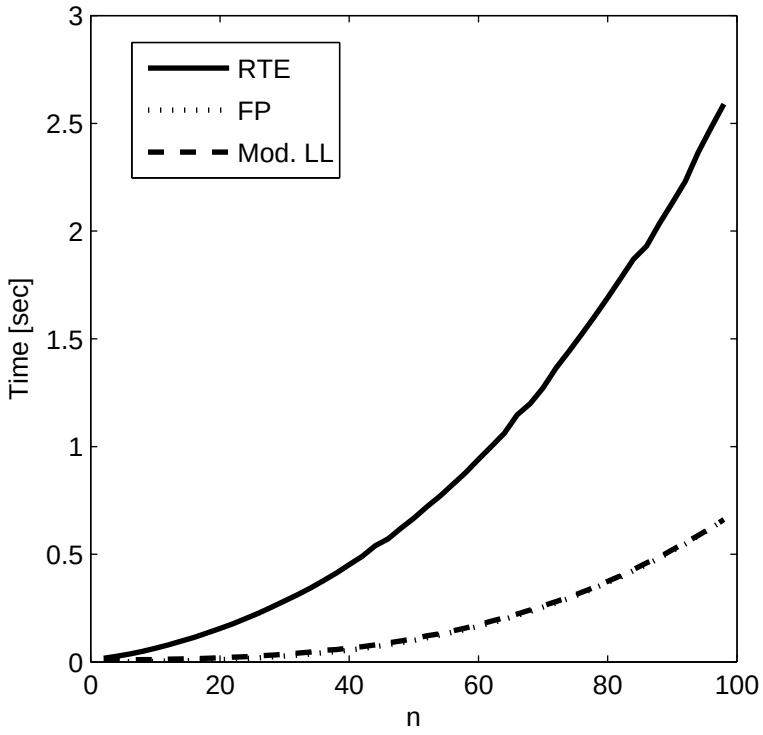

Figure 5.27: Computation time required to obtain solutions to the radiative transport equation with Henyey Greenstein phase function, the standard Fokker-Planck equation, and the modified Leakeas-Larsen equation.

$$\{V_2\}_{lk} = \sum_{n=0}^{N-1} \frac{2n+1}{4\pi} \hat{\phi}_{ln}^{-} P_n(\mu_k), \quad \mu_k \in [0,1], \tag{5.10}$$

$$\{V_3\}_{lk} = \sum_{n=0}^{N-1} \frac{2n+1}{4\pi} \hat{\phi}_{ln}^{+} P_n(\mu_k), \quad \mu_k \in [-1,0], \tag{5.11}$$

$$\{V_4\}_{lk} = \sum_{n=0}^{N-1} \frac{2n+1}{4\pi} \hat{\phi}_{ln}^{-} P_n(\mu_k) e^{\gamma_l^{-} L}, \quad \mu_k \in [-1,0]. \tag{5.12}$$

With

$$\vec{c} = (c_1, c_2, \ldots, c_{N/2})^T, \tag{5.13}$$

$$\vec{d} = (d_1, d_2, \ldots, d_{N/2})^T, \tag{5.14}$$

$$\vec{h} = \Big(h(\mu_1), h(\mu_2), \ldots, h(\mu_{N/2})\Big)^T, \ \mu_k \in [0,1], \tag{5.15}$$

$$0 = \underbrace{(0, 0, \ldots, 0)}_{N/2-\text{terms}}. \tag{5.16}$$

The inversion of the matrix $\mathbf{V}$ is essential to the P_N-method. It is desirable that $\mathbf{V}$ remain both invertible as the truncation order of the Legendre series increases and that it remain well-conditioned. The condition number of a matrix provides a gauge on how numerically well-posed a problem is. Moreover, the number of significant digits in the coefficients of the normal mode expansion can be inferred from the exponent of the resulting number when multiplying the condition number by the machine precision, ϵ [40]. Well-conditioned matrices are always invertible [40], thus the condition number will allow us to classify both desired properties of $\mathbf{V}$.

5.7.1 Definition of the Condition Number

When solving matrix equations of the form

$$\mathbf{A}\vec{x} = \vec{b} \tag{5.17}$$

it is natural to ask how sensitive the solution $\vec{x}$ is to changes in both $\vec{b}$ and $\mathbf{A}$. Systems in which small changes in $\vec{b}$ or $\mathbf{A}$ produce large changes in $\vec{x}$ are said to

be ill-conditioned. The condition number is defined [40]

$$\kappa(\mathbf{A}) = ||\mathbf{A}^{-1}||_1 \cdot ||\mathbf{A}||_1 \tag{5.18}$$

where the matrix 1-norm is defined

$$||\mathbf{A}||_1 = \max_j \sum_i |\mathbf{A}_{ij}|. \tag{5.19}$$

In Figure 5.28 the condition number of the matrix $\mathbf{V}$ is determined up to truncation $N = 200$ in the Legendre series. The maximal value of the condition number is 275. Using single precision arithmetic, a 24-bit mantissa is used for number storage providing a machine accuracy $\epsilon = 2^{-23} = 1.19 * 10^{-7}$. The number of significant digits in the numerical values of the expansion coefficients is roughly, see [40], $7 - log(275) = 4.561 \sim 4$. The situation improves if less Legendre modes are used. For instance at $N = 100$, in Figure 5.28, $\kappa(\mathbf{V}) = 80.38$, hence $7 - log(80.38) \sim 5$ digit accuracy is obtained in the expansion coefficients.

5.8 Summary

The condition number of the boundary value matrix $\mathbf{V}$ is sufficiently small to allow application of the P_N-method to order $N = 200$ with 4 digit accuracy in the expansion coefficients, see (4.26) and (4.27). The convergence of the relative error for solutions obtained using the P_N method was shown to converge exponentially in the truncation order, n, of the Legendre series. The decay rate of the relative error is not constant. It exhibits local minima that can be employed to obtain accuracies at lower order truncations obtainable at higher order truncations. The optimal truncation order, n^*, of the P_N-method was identified for each scattering operator in the range $g \in [0.7, 0.999]$. The computation time required for truncations ≤ 100 were found to be conducive to prompt side-by-side comparison of scattering theories.

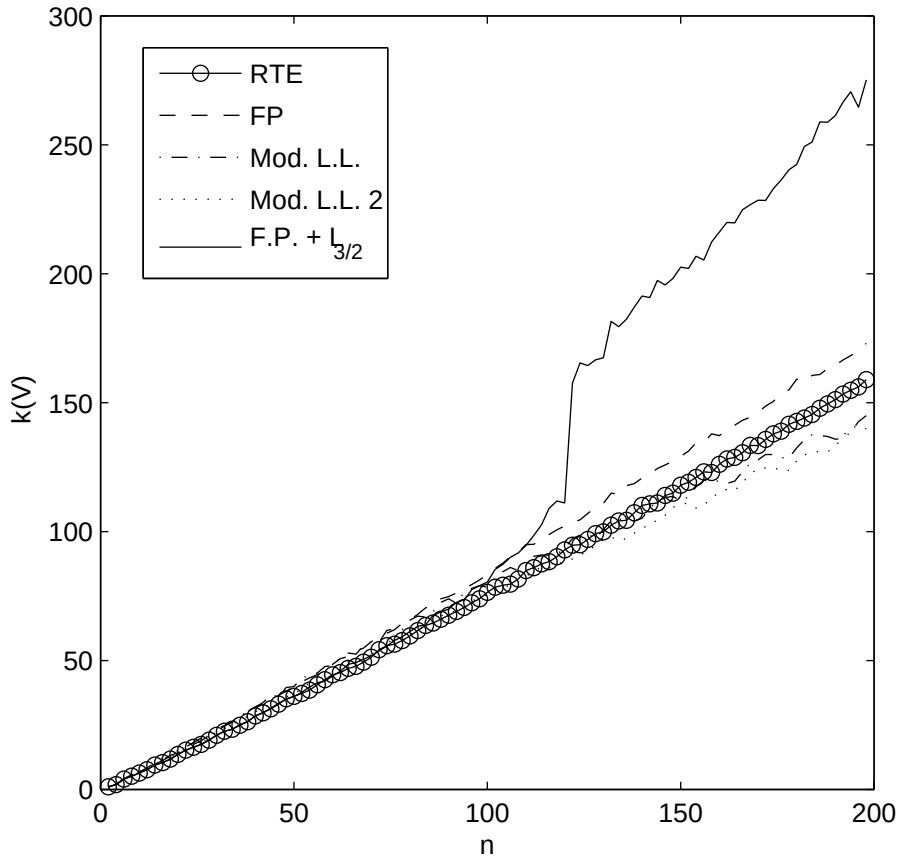

Figure 5.28: Condition number for each scattering theory of the boundary condition coefficient matrix, $\mathbf{V}$ computed in the 1-norm. Material properties: $\sigma_s = 100$ [cm^{-1}], $\sigma_a = 1$ [cm^{-1}], $L = 1$ [cm].

In the next chapter we compare and contrast the scattering theories. Our main goal will be in the assessment of the ability of the generalized Fokker-Planck equations of Chapter 3 to describe transport as modeled by the integral scattering operator with Henyey-Greenstein phase function over the range of anisotropies characteristic of tissue optics.

Chapter 6

Accuracy of Generalized Fokker-Planck Equations in Tissue Optics

6.1 Introduction

Using the P_N-method, the ability of the generalized Fokker-Planck equations to describe transport in anisotropic media is investigated. Typical solutions are presented for the angularly resolved backscattered and transmitted radiance, the reflectance and transmittance, and depth-dependent fluence rate. Solutions to the transport equation with Henyey-Greenstein phase function and the generalized Fokker-Planck equations are then compared in a quantitative fashion through the L_2-error. It is found that the radiance, flux and fluence are best described by the pseudo-differential operator $\mathcal{L}_{3/2}$ in combination with the spherical Laplacian in the limit $g \to 1$. However, for values of the anisotropy in the typical tissue optics range of $g \in [0.7, .9]$, the modified Leakeas-Larsen equation is found to be the best model.

6.2 Solutions: Backscattered and Transmitted Radiance

The backscattered and transmitted radiance are presented in Figures 6.1-6.10 for various values of the anisotropy factor in the range $g \in [0.7,\ 0.9]$. A slab thickness of 1 $[cm]$ is assumed throughout along with the standard material properties $\sigma_s = 100$ $[\text{cm}^{-1}]$, $\sigma_a = 1$ $[\text{cm}^{-1}]$.

For the backscattered radiance, the modified Leakeas-Larsen approximations agree best with the Henyey-Greenstein curve at $g = 0.7$ and $g = 0.8$, see Figures 6.1 and 6.2, respectively, though deviations are seen as scattering becomes more anisotropic at $g = 0.9$ and above, see Figures 6.3-6.5. For values of anisotropies greater than 0.9, Figures 6.4-6.5, the backscattered radiance is best described by the pseudo-differential operator $\mathcal{L}_{3/2}$ in combination with the spherical Laplacian.

In the transmission profiles, the Fokker-Planck model and modified Leakeas-Larsen equations compare favorably to the transport equation with Henyey-Greenstein phase function for anisotropies $g = 0.7$, 0.8 and 0.9, see Figures 6.6-6.8. As in the case of backscatter, the pseudo-differential operator $\mathcal{L}_{3/2}$ in combination with the spherical Laplacian does the best job above $g = 0.9$, see Figures 6.9-6.10. In general as g becomes closer to one, the Fokker-Planck and modified Leakeas-Larsen radiances in both transmission and backscatter begin to converge. This is attributable to the similarity of the analytical form of their scattering operator spectra as g tends to one. See §3.4.

In the next section, the agreement of the radiances for all anisotropies in the tissue optics range will be studied through an L_2-error analysis.

6.3 L_2-Error of RTE and GFPE Solutions: Radiance

In this section we present the relative error of the backscattered and transmitted radiances of the generalized Fokker-Planck equations in the L_2-norm. We refer simply to "the error" or L_2-error from hence forth and define the L_2-error between solutions to the RTE with Henyey-Greenstein phase function, ψ^{RTE}, and the GFPE, ψ^{GFP}, as

$$||\psi^{RTE} - \psi^{GFP}||_{L_2(a,b)}(z) = \Big(\int_a^b |\psi^{RTE}(\mu, z) - \psi^{GFP}(\mu, z)|^2 \mathrm{d}\mu \Big)^{1/2}. \qquad (6.1)$$

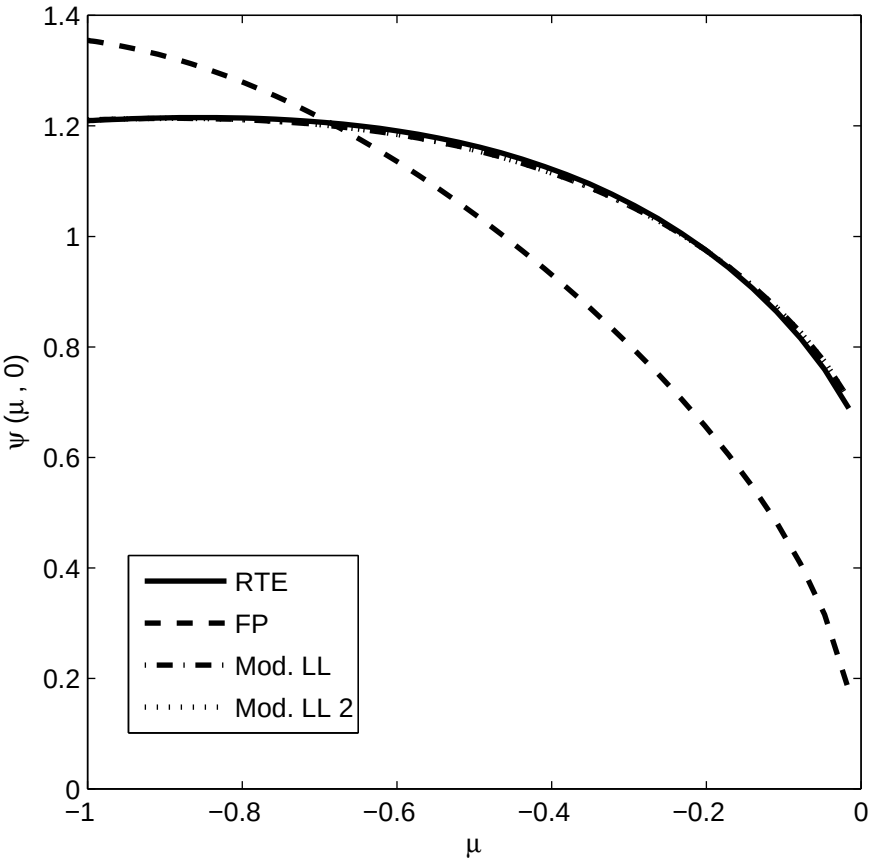

Figure 6.1: Backscattered Radiance, $g = 0.7$, N = 100

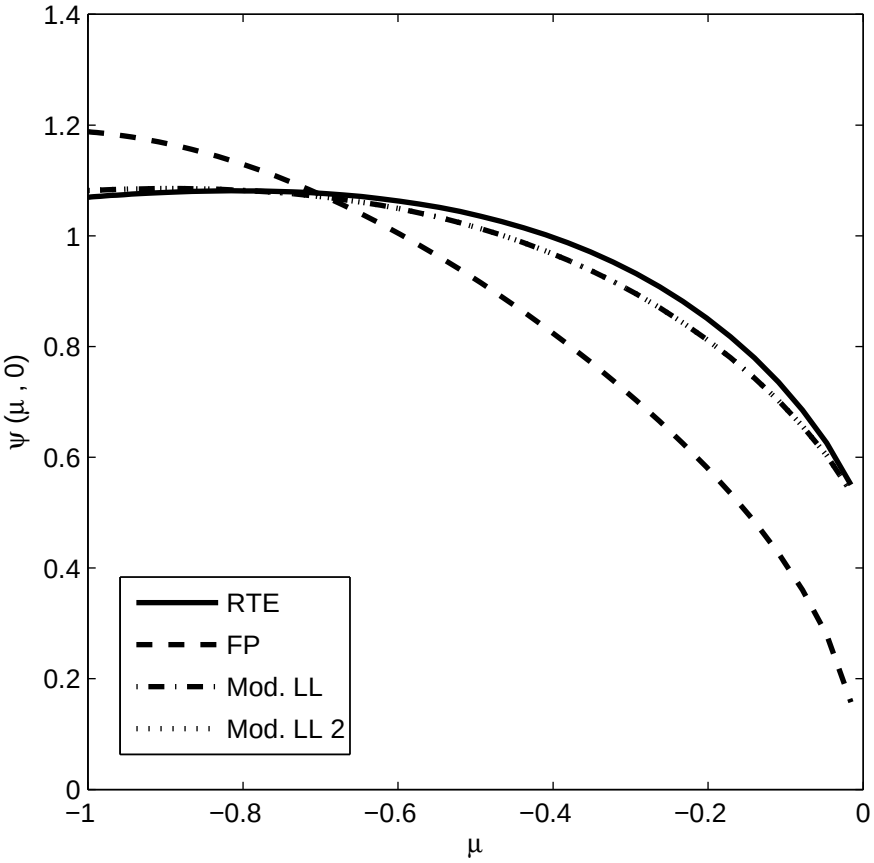

Figure 6.2: Backscattered Radiance, $g = 0.8$, N = 100

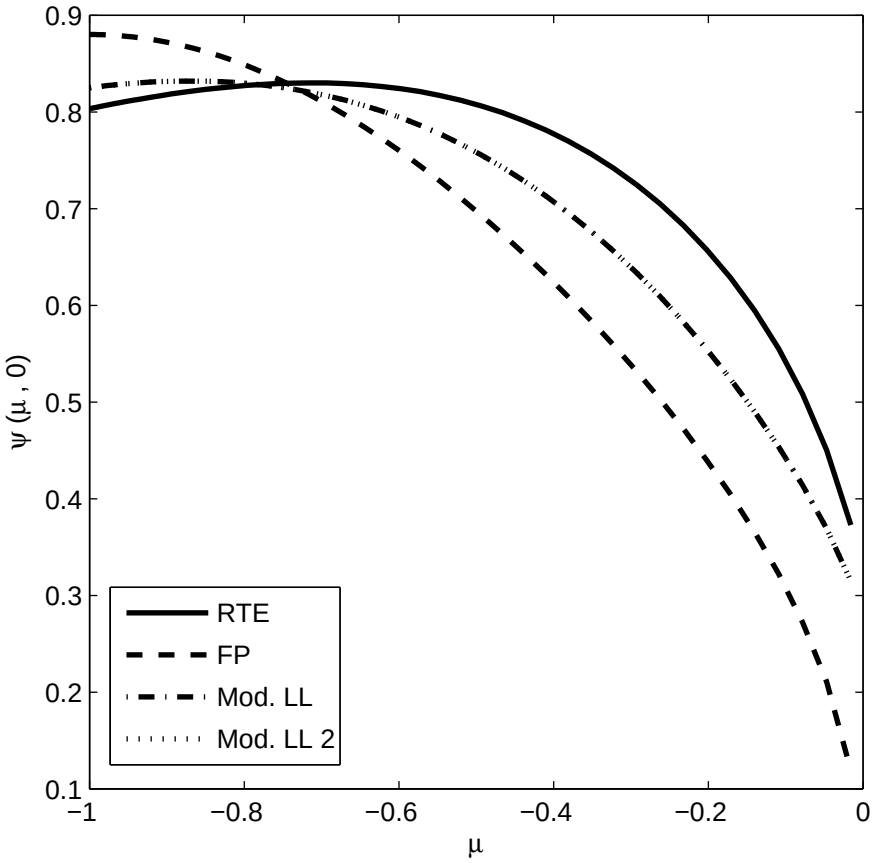

Figure 6.3: Backscattered Radiance, $g = 0.9$, N = 100

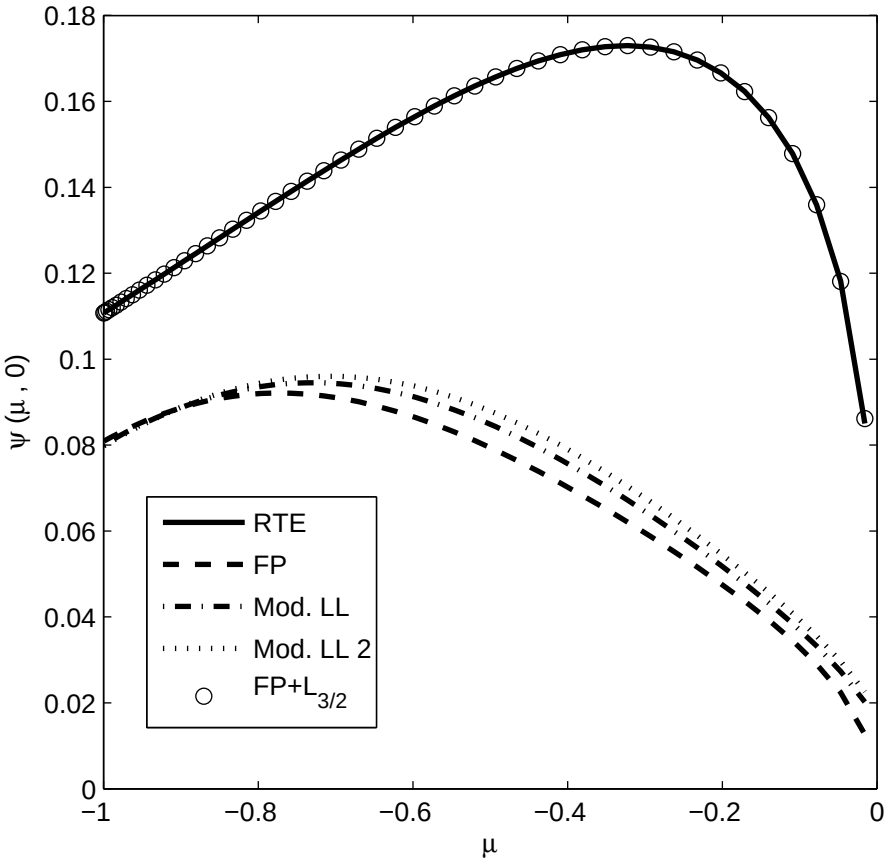

Figure 6.4: Backscattered Radiance, $g = 0.99$, N = 100

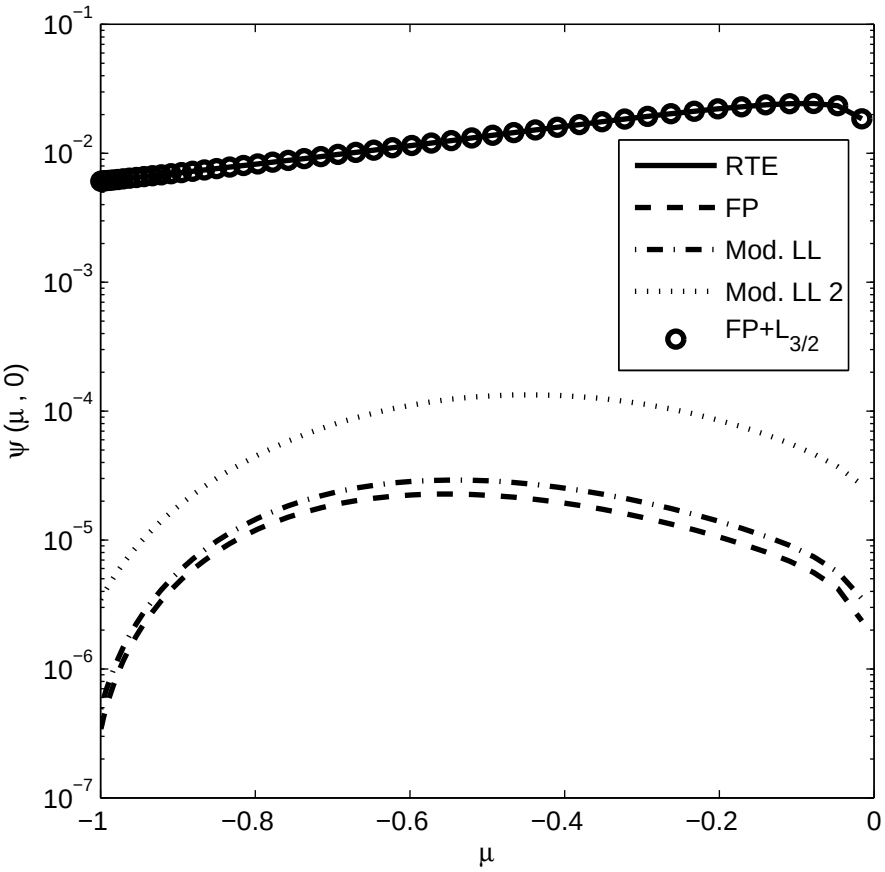

Figure 6.5: Backscattered Radiance, $g = 0.999$, N = 100

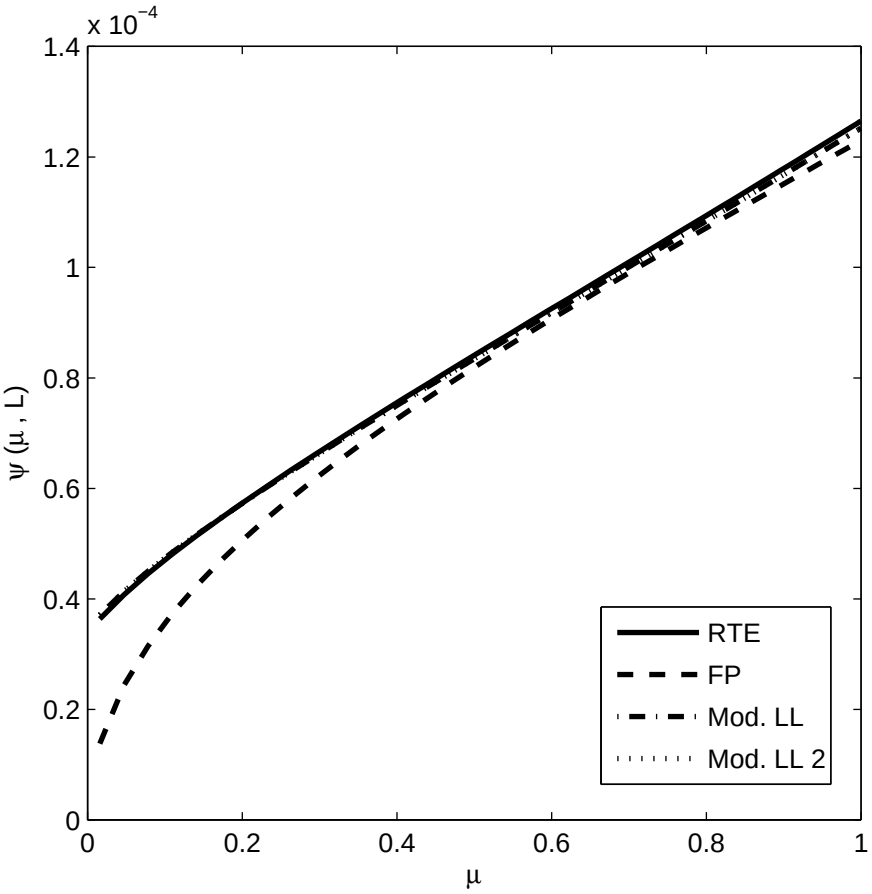

Figure 6.6: Transmitted Radiance, $g = 0.7$, N = 100

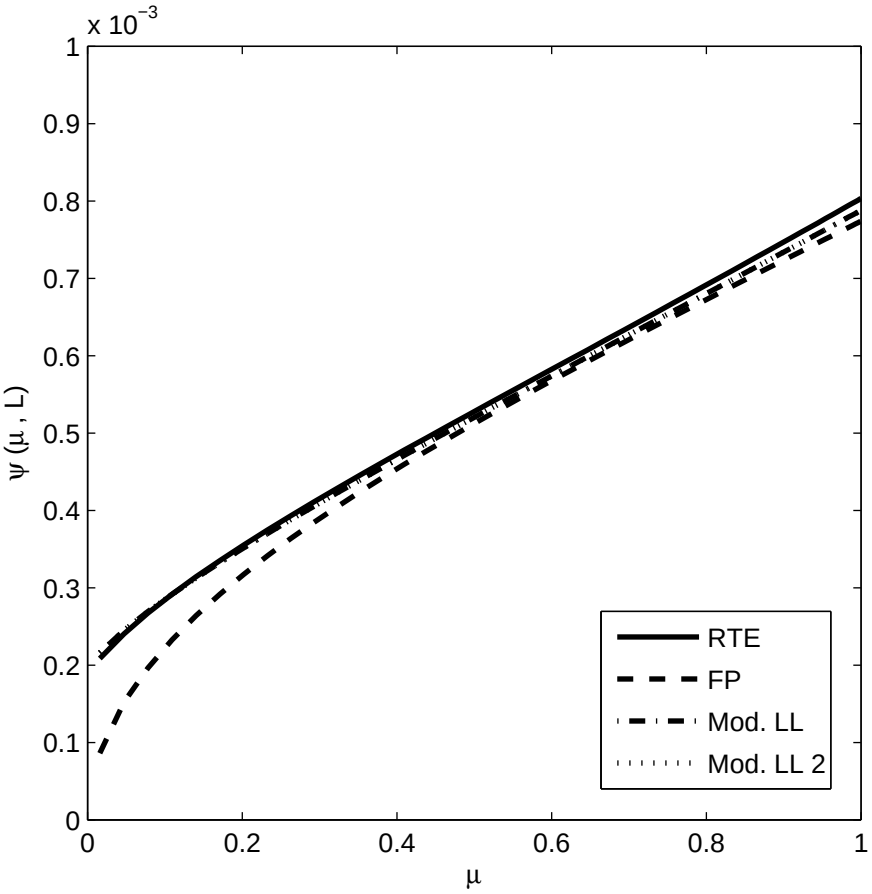

Figure 6.7: Transmitted Radiance, $g = 0.8$, N = 100

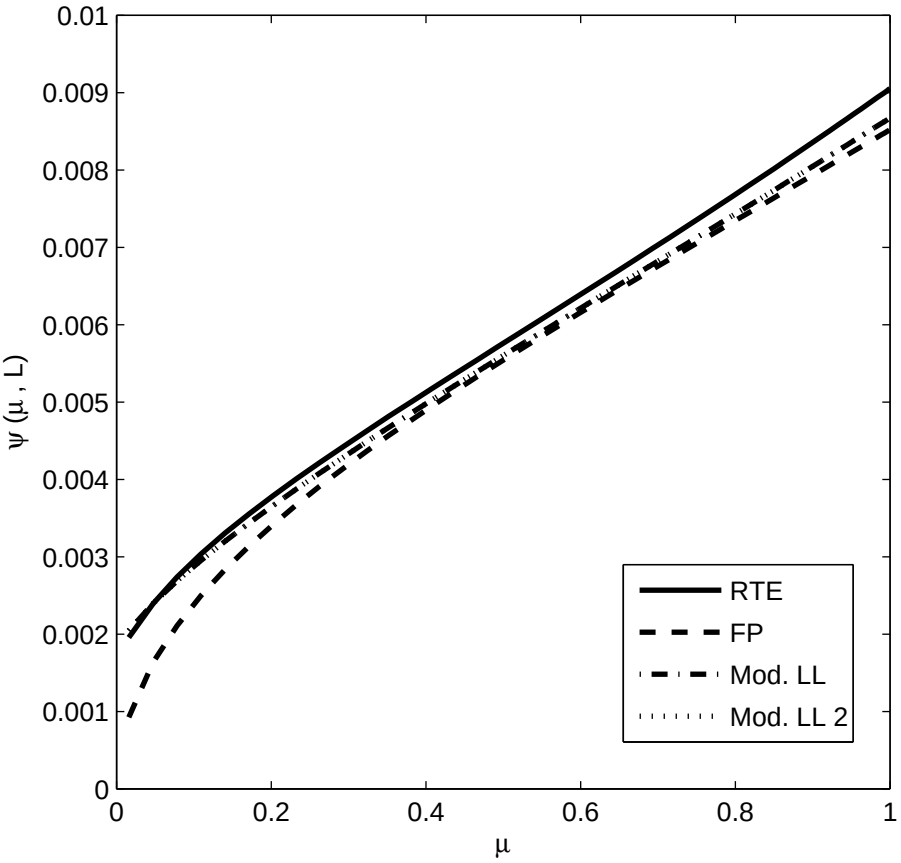

Figure 6.8: Transmitted Radiance, $g = 0.9$, N = 100

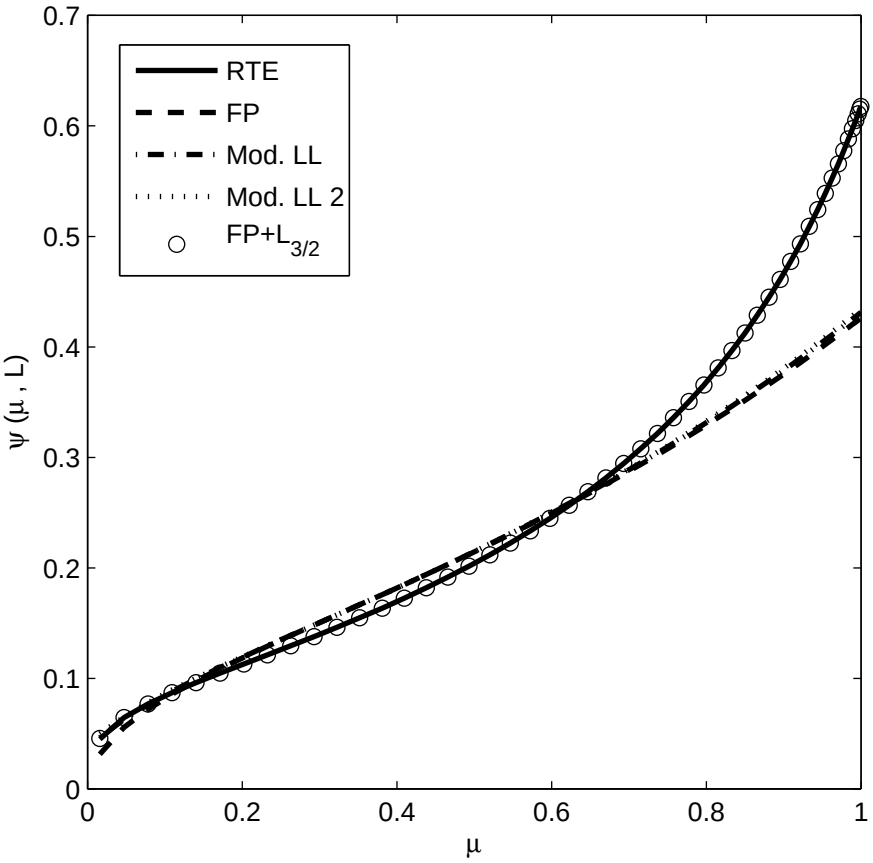

Figure 6.9: Transmitted Radiance, $g = 0.99$, N = 100

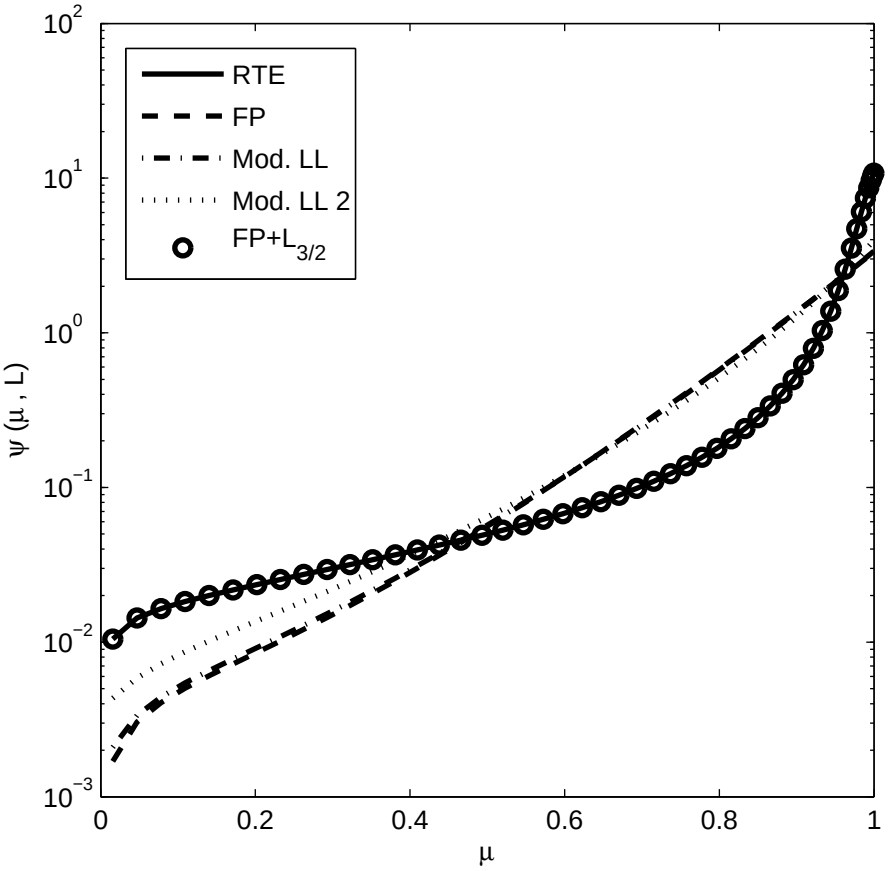

Figure 6.10: Transmitted Radiance, $g = 0.999$, N = 100

We consider only $z = L$ in which $a = 0$ and $b = 1$ for transmission, and $z = 0$ in which $a = -1$ and $b = 0$ for backscatter. Figures 6.11 and 6.12 present the L_2-error for the backscattered radiance and Figures 6.13 and 6.14 present the L_2-error for the transmitted radiance.

In the backscattered error profile we find again that the modified Leakeas-Larsen equations are the best choice for anisotropies in the range $g \in [0.7, 0.9]$, with the pseudo-differential operator in combination with the spherical Laplacian being the best choice in the case of scattering with anisotropies in the range $g > 0.9$. Note that for forward-scattering in the range 0.99 to 0.999, the Fokker-Planck and modified Leakeas-Larsen equations are indistinguishable. This is attributed to the similarity of their scattering operator eigenvalues as g tends towards one. In the transmission profiles the same behaviors occur: the modified Leakeas-Larsen equations again dominate the Fokker-Planck equation over the range of tissue anisotropies [0.7, 0.9]. The pseudo-differential operator is again the best choice for stronger forward-scattering characterized by $g > 0.9$. Note as well that because the integral scattering operator with Henyey-Greenstein phase function does not possess an asymptotic Fokker-Planck limit as g tends to one, the L_2-error continues to grow in the range of $0.99 < g < 0.999$. In general all of the GFPE are more accurate in predicting the transmitted intensity distribution over the range of anisotropies in [0.7, 0.9] as opposed to backscatter over the same range of g. From Figures 6.11 and 6.13 we see the L_2-error in transmission is bounded by 3×10^{-4} in transmission as opposed to 3×10^{-1} in backscatter for $g \in [0.7, 0.9]$.

6.4 Relative Error of RTE and GFPE Solutions: Surface Currents

The relative error of the backscattered and transmitted currents are presented in Figures 6.15-6.18. The backscattered and transmitted surface currents were introduced in §2.4. The relative error in the surface currents of the GFPE

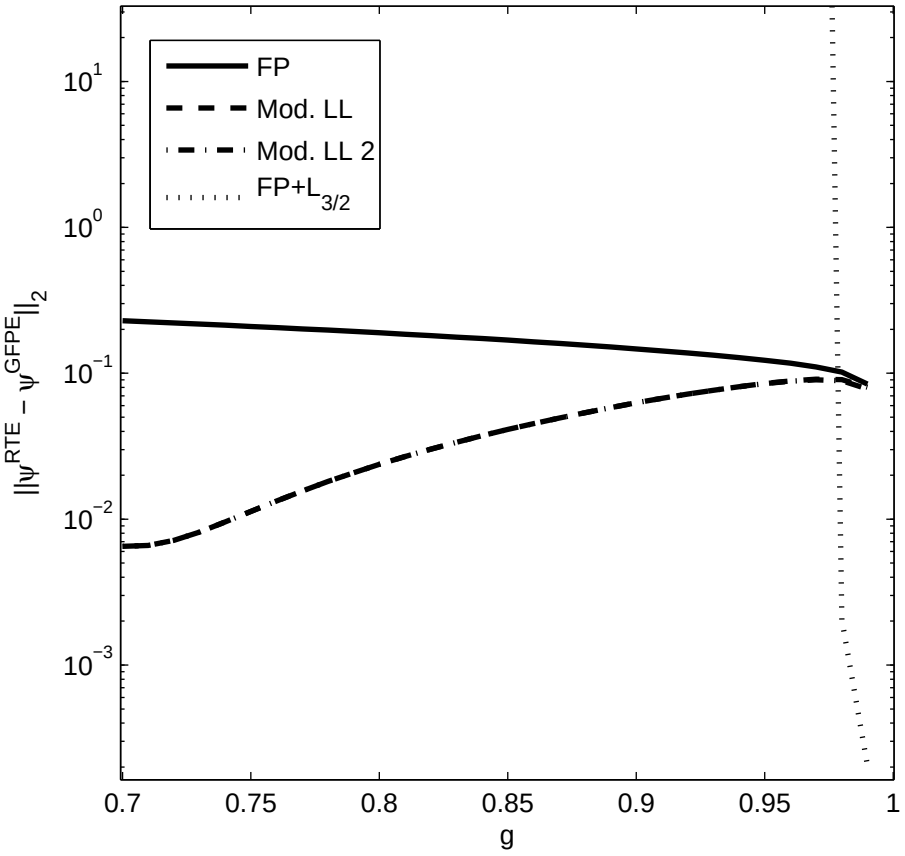

Figure 6.11: L_2-error of the RTE and GFPE Backscattered Solutions vs. g, $N = 100$

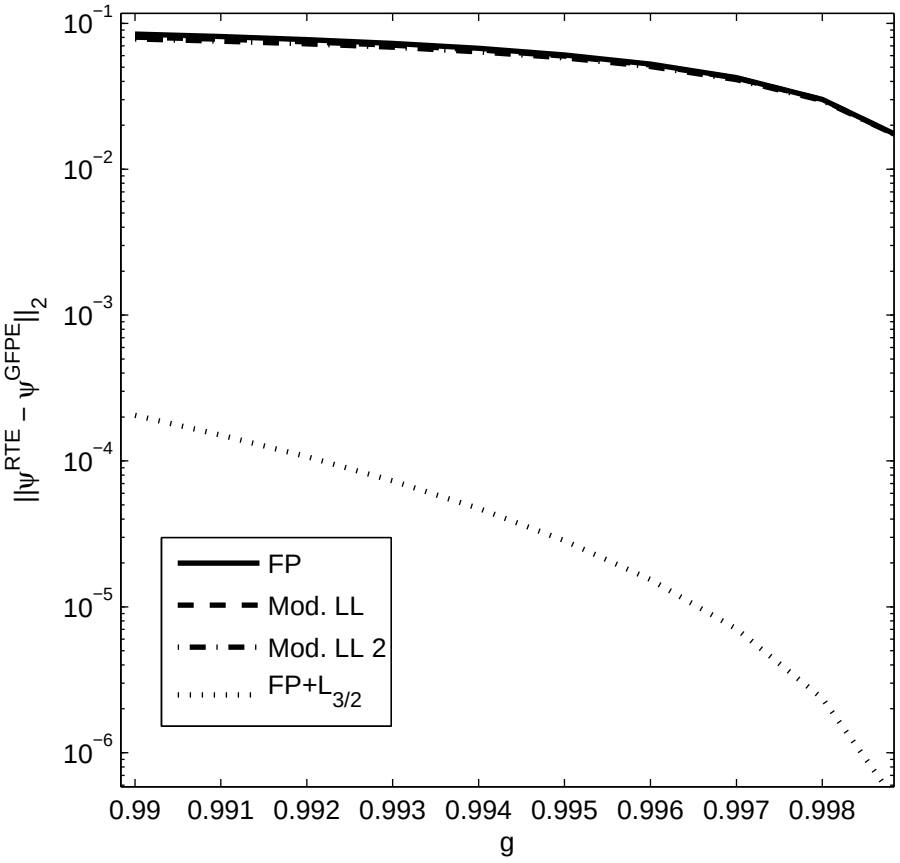

Figure 6.12: L_2-error of the RTE and GFPE Backscattered Solutions near $g = 1$, $N = 100$

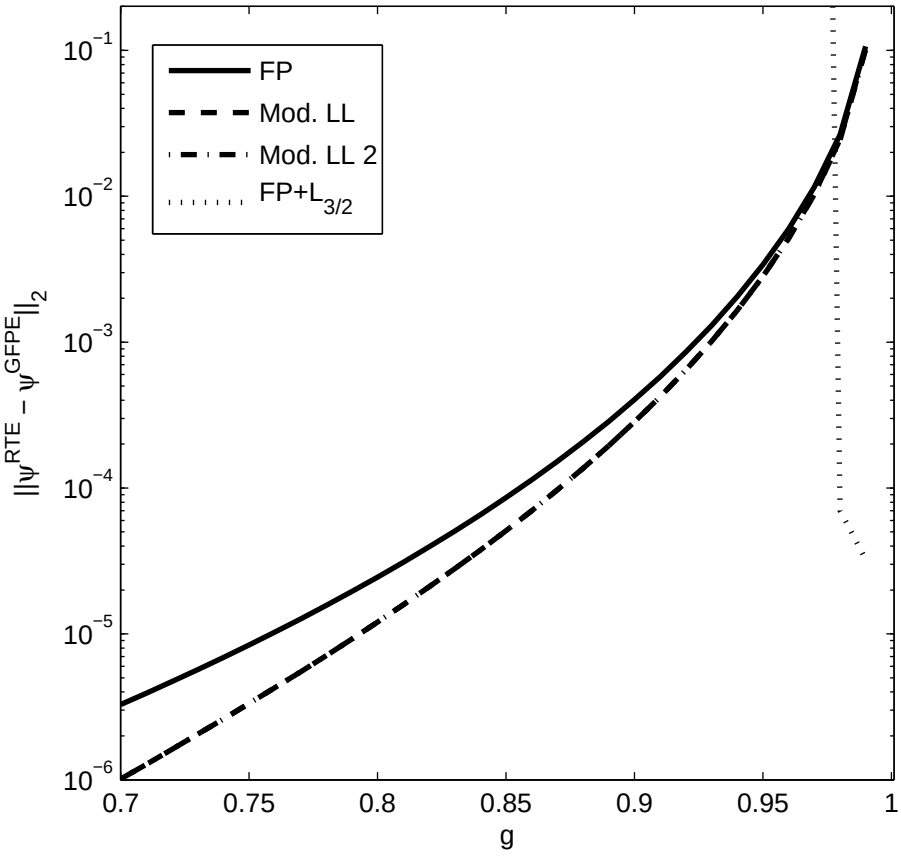

Figure 6.13: L_2-error of the RTE and GFPE Transmitted Solutions vs. g, $N = 100$

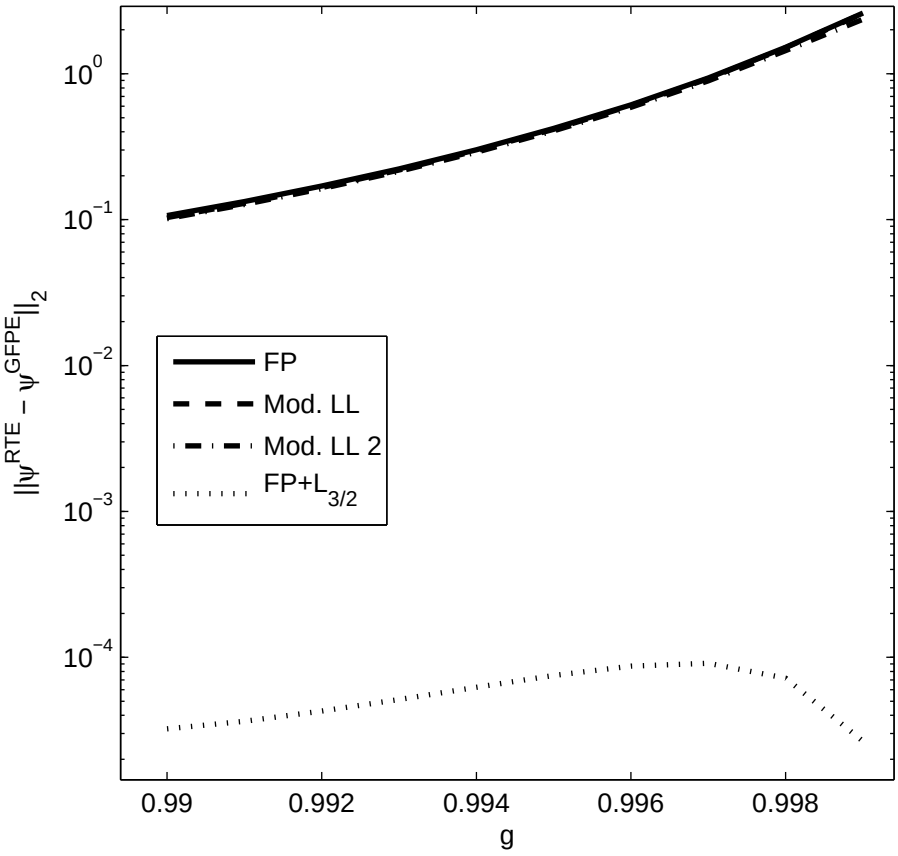

Figure 6.14: L_2-error of the RTE and GFPE Transmitted Solutions near $g = 1$, $N = 100$

are determined according to comparison to the current of the RTE with Henyey-Greenstein phase function according to

$$R(N;g) = \frac{|R^{RTE} - R^{GFP}|}{|R^{RTE}|},\ T(N;g) = \frac{|T^{RTE} - T^{GFP}|}{|T^{RTE}|}. \tag{6.2}$$

N denotes the number of Legendre polynomials used in the calculation. g is the anisotropy factor of the scattering material.

The accuracy of the GFPE in predicting the surface currents is found to be dominated by the modified Leakeas-Larsen equations over the range of anisotropies [0.7, 0.9] in both backscatter and transmission, with the pseudo-differential operator in combination with the spherical Laplacian being the best model over the range of strong forward-scattering, $g > 0.9$. Again we find that the modified Leakeas-Larsen equations predict the same result as the standard Fokker-Planck equation as g tends to one.

6.5 Solutions: Depth-dependent Fluence

In Figures 6.19-6.22 the fluence rate, introduced in §2.4, is presented for anisotropies 0.7, 0.8, 0.9, 0.99 respectively. The GFPE are all quantitatively similar to the fluence predicted by the RTE with Henyey-Greenstein phase function. For g =0.7, 0.8 and 0.9 the Fokker-Planck equation overshoots the peak in the fluence rate while the modified Leakeas-Larsen equations match the peak of the RTE with Henyey-Greenstein phase function. Again we observe that the Fokker-Planck and modified Leakeas-Larsen equations give identical results as $g \sim 1$. In the next section the relative errors of the fluence rates is compared in the L_2-norm.

6.6 L_2-Error of RTE and GFPE Solutions: Fluence

The L_2-error of the fluence is presented in Figures 6.23-6.24. The modified Leakeas-Larsen equations are found to be the best approximate models over the

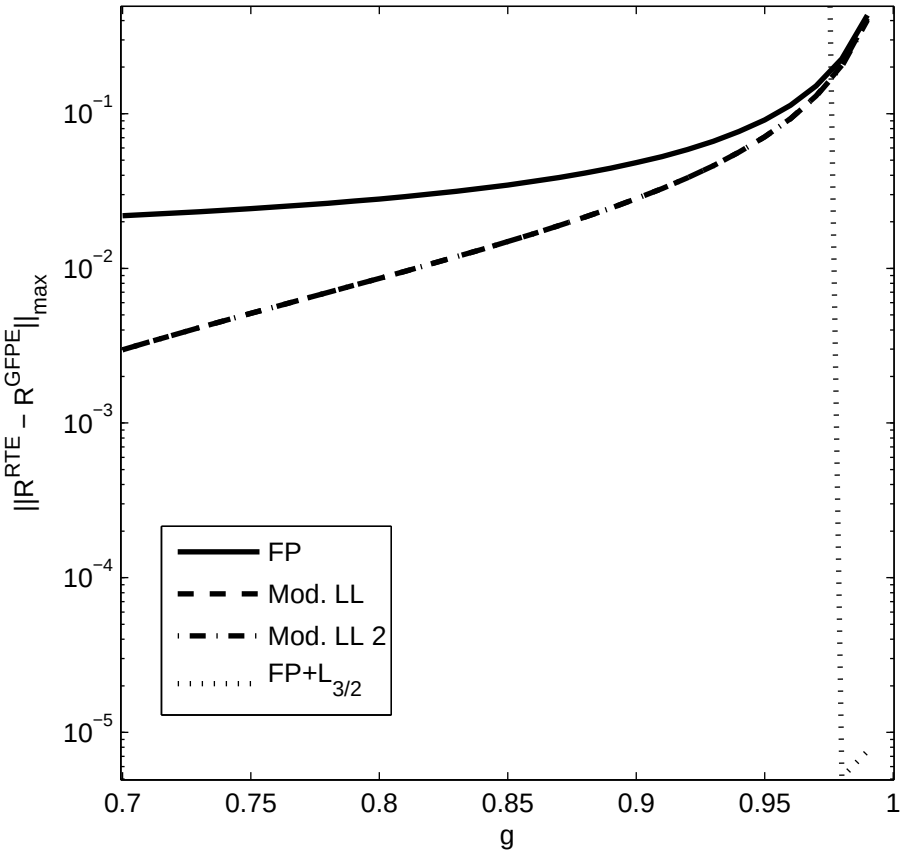

Figure 6.15: Relative Error of the Reflected Current vs. g, $N = 100$

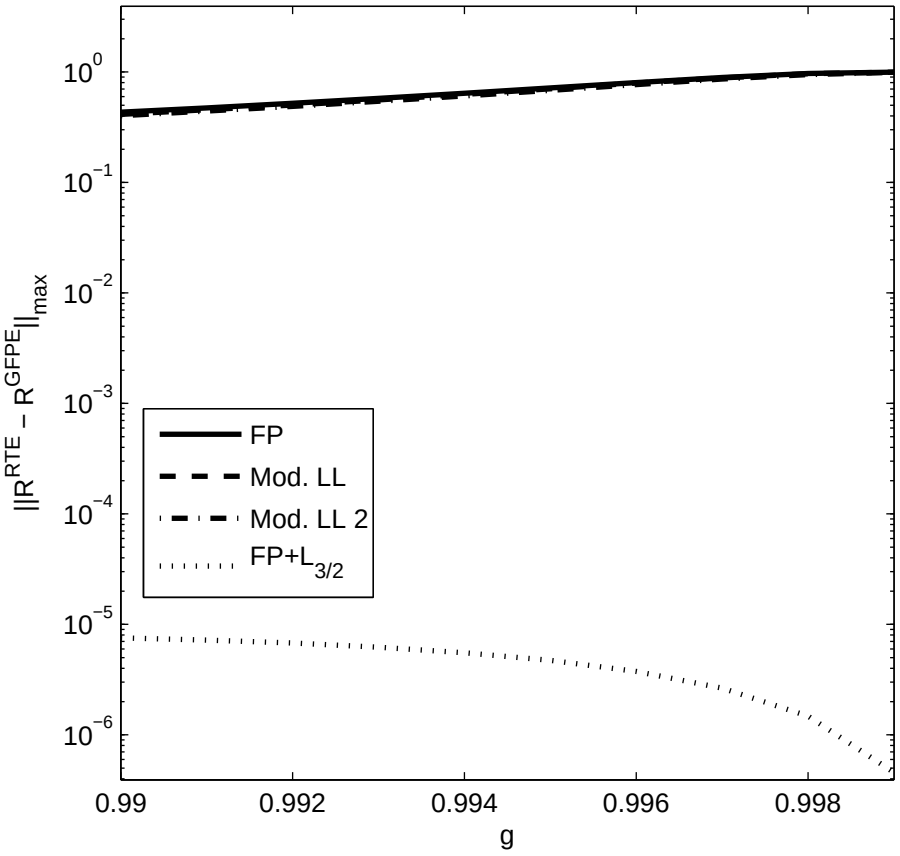

Figure 6.16: Relative Error of the Reflected Current near $g = 1$, $N = 100$

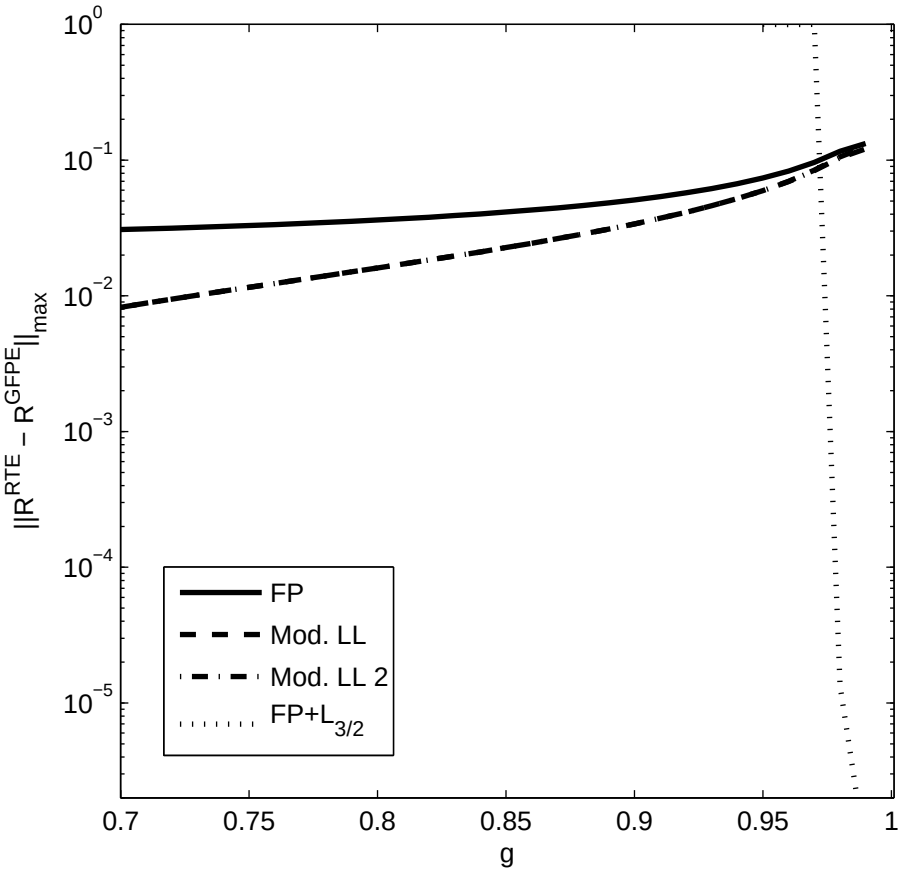

Figure 6.17: Relative Error of the Transmitted Current vs. g, $N = 100$

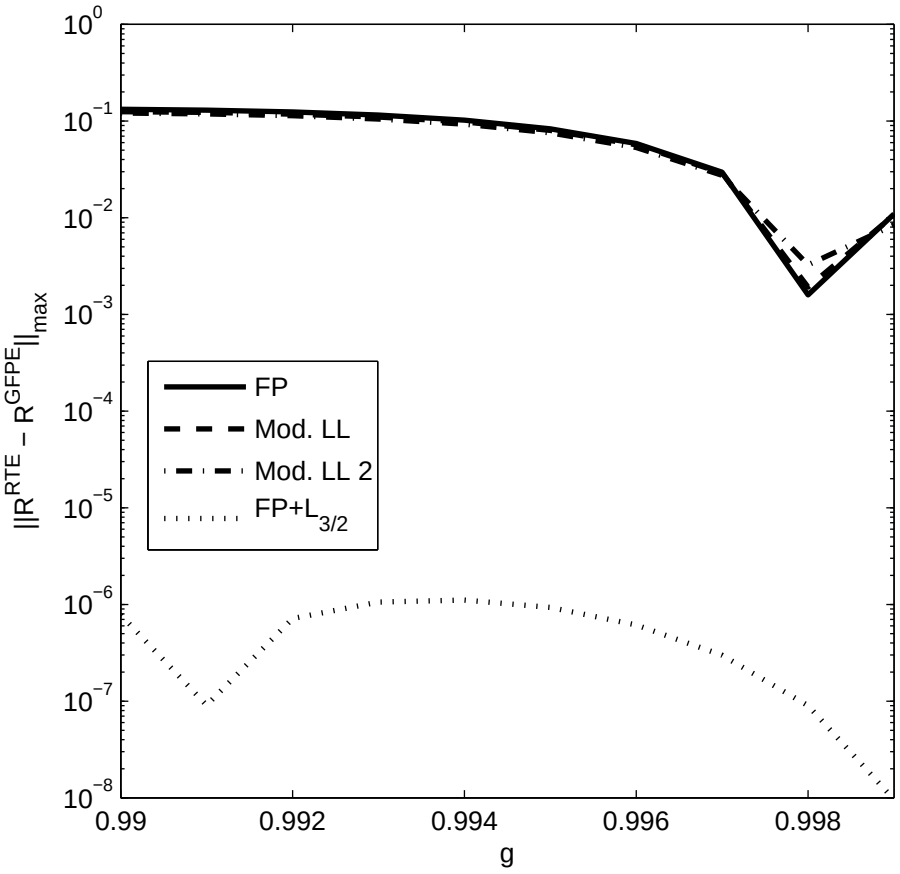

Figure 6.18: Relative Error of the Transmitted Current near $g = 1$, $N = 100$

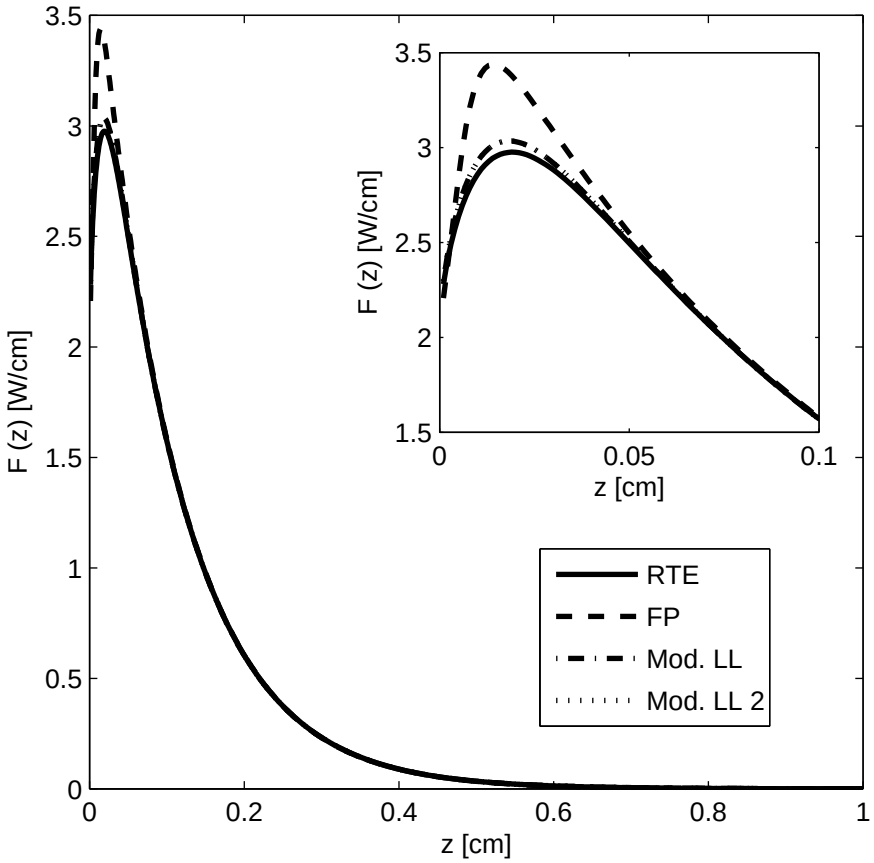

Figure 6.19: Fluence, $g = 0.7$, N = 100

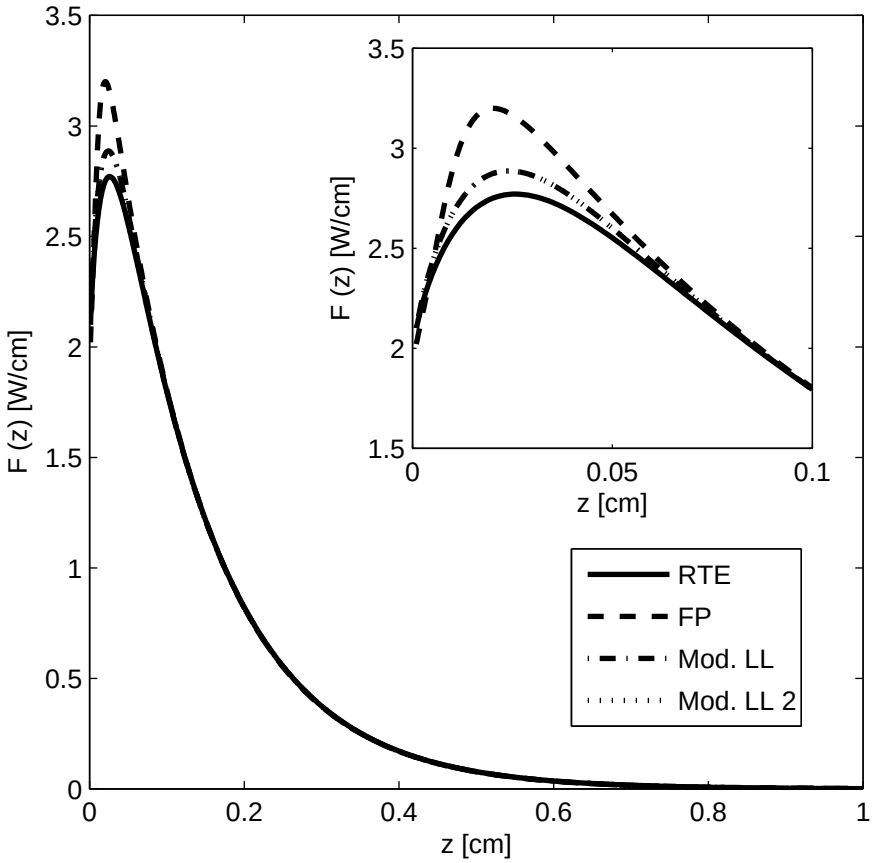

Figure 6.20: Fluence, $g = 0.8$, N = 100

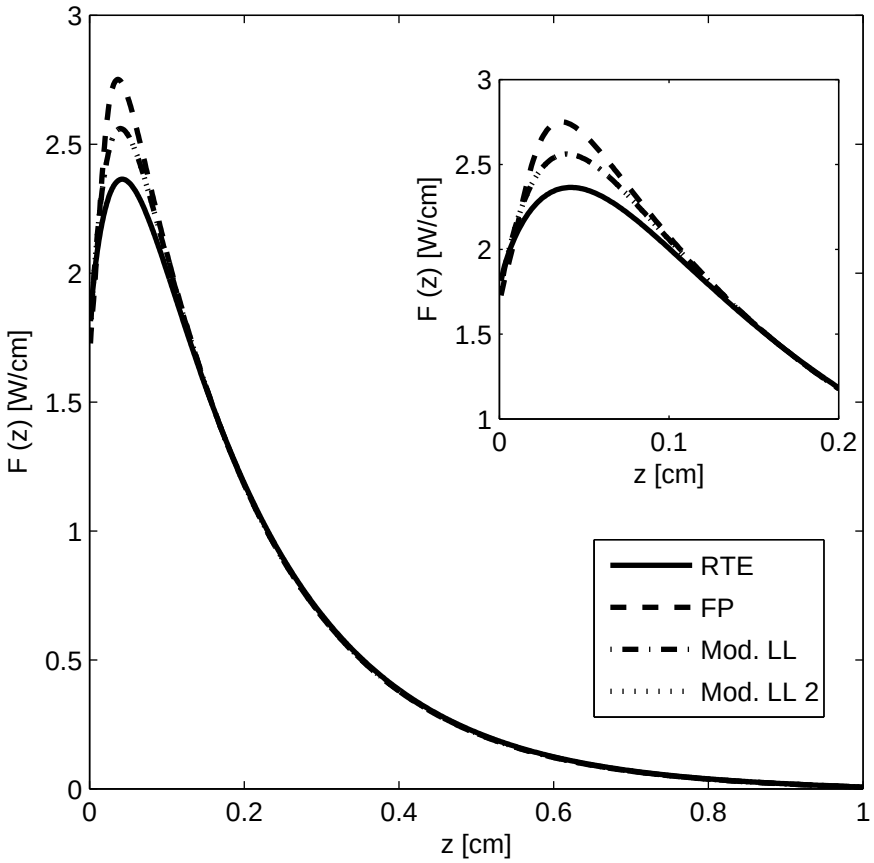

Figure 6.21: Fluence, $g = 0.9$, N = 100

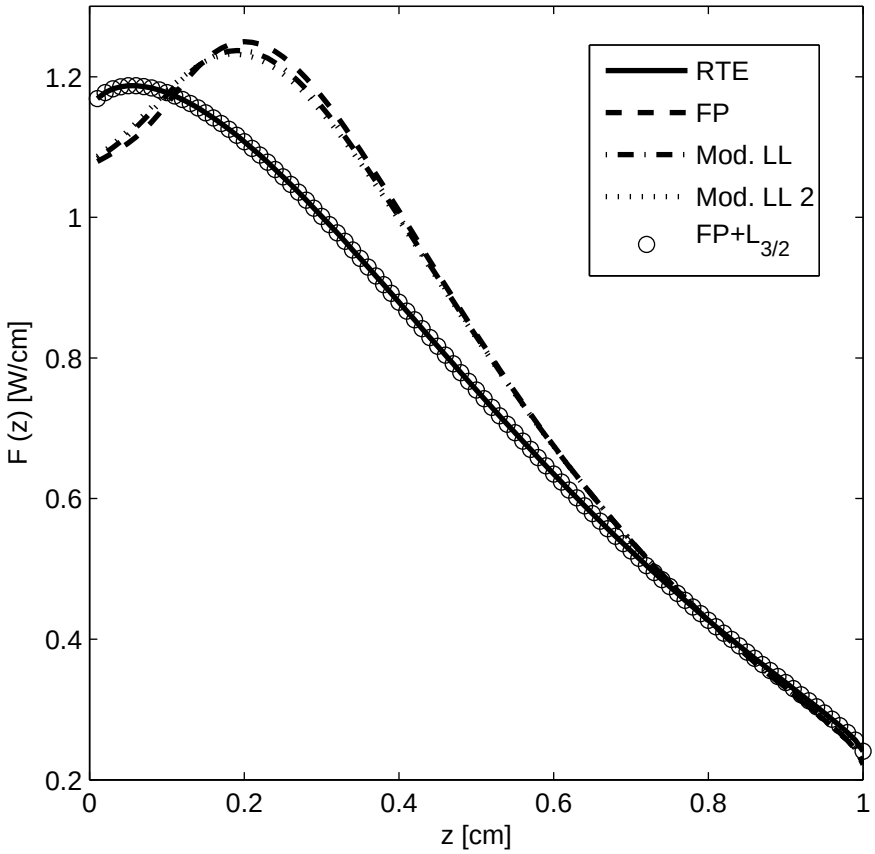

Figure 6.22: Fluence, $g = 0.99$, N = 100

range of anisotropies [0.7, 0.9] with the pseudo-differential operator in combination with the spherical Laplacian being the best approximate forward-scattering theory in the range of forward-scattering anisotropies [0.99, 0.999].

6.7 Summary

Using the P_N-method, the ability of the generalized Fokker-Planck equations to describe transport in anisotropic media was investigated. Typical solutions were presented for the angularly resolved backscattered and transmitted radiance, the reflectance and transmittance, and depth-dependent fluence rate. Solutions to the transport equation with Henyey-Greenstein phase function and the generalized Fokker-Planck equations were then compared in a quantitative fashion through the L_2-error of their solutions. It was found that the radiance, flux and fluence rate are best described by the pseudo-differential operator $\mathcal{L}_{3/2}$ in combination with the spherical Laplacian in the limit $g \to 1$. However, for values of the anisotropy in the typical tissue optics range of $g \in [0.7, .9]$, the modified Leakeas-Larsen equation is found to be the best model.

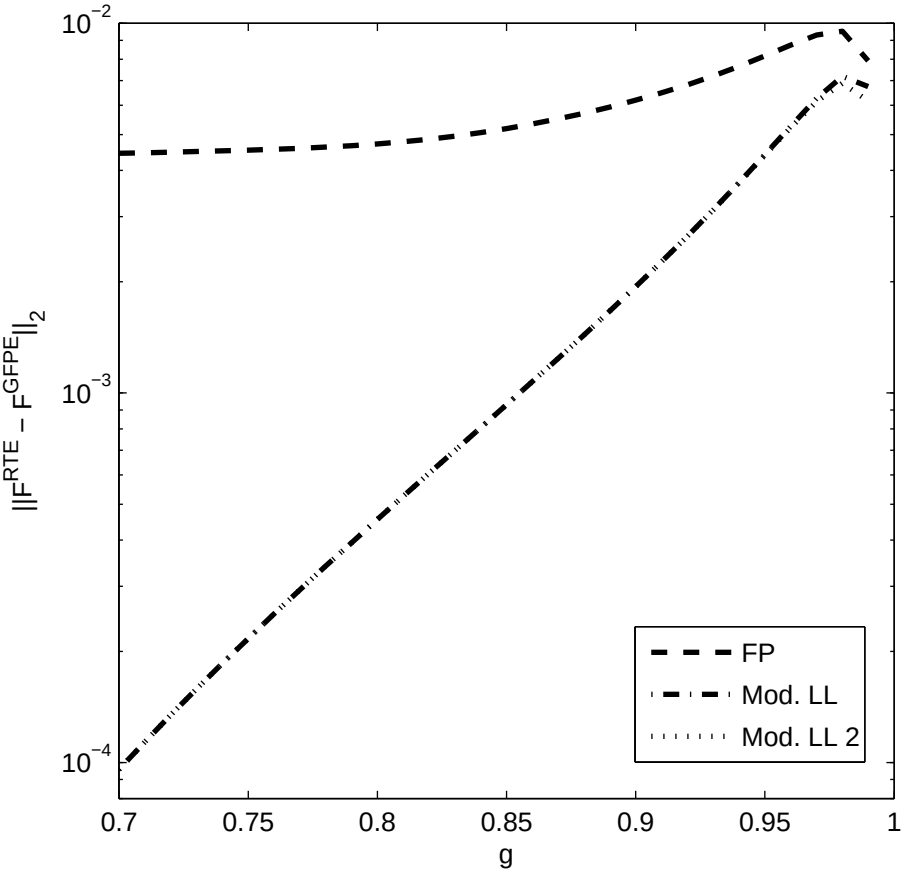

Figure 6.23: L_2-error of the Fluence vs. g, $N = 100$

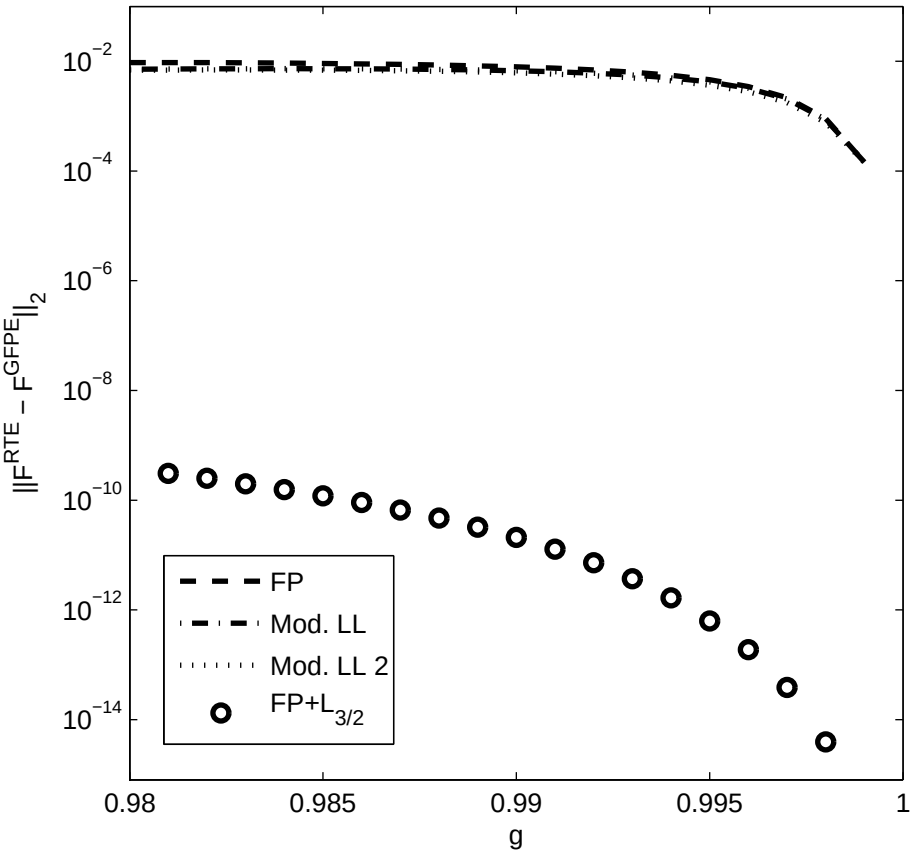

Figure 6.24: L_2-error of the Fluence near $g = 1$, $N = 100$

Chapter 7

Summary and Outlook

The main result of this dissertation is the discovery that the P_N-method provides accurate and timely solutions to linear transport equations with scattering operators of integral and differential type. More generally, the P_N-method is applicable to any scattering operator whose eigenfunctions are the spherical harmonics. Operators that satisfy this requirement are integral scattering operators with any scattering phase function, such as the Henyey-Greenstein phase function, and functions of the Laplace-Beltrami operator- characteristic of forward-scattering approximations. The P_N-method was used to compare forward-scattering approximations of the RTE with Henyey-Greenstein phase function. Such approximations include the Fokker-Planck equation, the modified Leakeas-Larsen equation and the standard Fokker-Planck operator in combination with the pseudo-differential operator $\mathcal{L}_{3/2}$. It was found that the radiance, flux and fluence rate are best described by the standard Fokker-Planck operator in combination with the pseudo-differential operator $\mathcal{L}_{3/2}$ in the limit $g \to 1$. However, for values of the anisotropy in the typical tissue optics range of $g \in [0.7, .9]$, the modified Leakeas-Larsen equation was found to be the best model.

One open area of research is the extension of the P_N-method to collimated illumination of a semi-infinite half-space. Collimated illumination has been investigated numerically by Kim [34] using the Fokker-Planck equation and subse-

quently investigated using the Electric Field Monte Carlo (EMC) method applied to the RTE by the author [45]. The Fokker-Planck equation predicts the formation of a halo about the point of illumination in the backscattered light. The halo is believed to result from near forward scattering events of photons as they traverse a scattering medium; giving rise to semi-circular trajectories that allow the photons to exit the surface through which they entered in a characteristic circular pattern. Using EMC, the author observed the halo only for the case of *pulsed* collimated illumination while the standard Fokker-Planck equation predicts a *steady-state* halo formation.

Halo formation has yet to be seen experimentally though it appears to have been ruled out in the lab for steady-state collimated illumination [10]. Time-resolved experiments are ultimately needed to establish the existence of halo formation. Should the halo exist, it would be of great use for non-invasive characterization of biological materials. Using the EMC, the author has shown that the time-dependent halo behavior is sensitive to absorption [46] and anisotropy factor [45].

Appendix A

Incompatibility of the Henyey-Greenstein phase function and Fokker-Planck equations

Researchers have been concerned with the compatibility of forward-scattering approximations and accurate models of tissue-light interactions. The most widely used, empirically tested, phase function is the Henyey-Greenstein phase function, presented in Chapter 1.

$$f_{\mathrm{HG}}(\omega \cdot \omega') = \frac{\sigma_s(1-g^2)}{4\pi(1-2g(\omega\cdot\omega')+g^2)^{3/2}}, \tag{A.1}$$

The compatibility of the Henyey-Greenstein phase function may be tested by considering the weighting factors, T_l, of equation (3.15) that determine the truncation order of the high order Fokker-Planck equation given in (3.16). Specifically we assess their value in the limit as $\epsilon = (1-g)$ tends to zero.

Fortunately, the Henyey-Greenstein phase function is closely related to the generating function of the Legendre polynomials and can be represented as the following infinite sum, let $\xi = \omega \cdot \omega'$,

$$\frac{\sigma_s(1-g^2)}{4\pi(1-2g\xi+g^2)^{3/2}} = \sigma_s \sum_{m=0}^{\infty} \frac{2m+1}{4\pi} g^m P_m(\xi). \tag{A.2}$$

Putting (A.2) into (3.15) one finds that in the limit $\epsilon = (1-g) \to 0$ [48],

$$\lim_{\epsilon\to 0} T_l = \left(\frac{2^{l-1}}{2l-1}\right)\epsilon,\ l \geq 2. \tag{A.3}$$

This finding shows that all of the terms in the series are of order ϵ and cannot be omitted. Thus we find that not only does the standard Fokker-Planck equation fail but also the higher order Fokker-Planck equation fails[48] when using the Henyey-Greenstein phase function. This results from the violation of (3.11) by the Henyey-Greenstein phase function. The Henyey-Greenstein phase function falls off algebraically from $\xi = 1$, and hence too slowly, for (3.11) to be satisfied. See [47, 48].

Appendix B

Derivation of the eigenvalue relation $\mathcal{L}_{3/2}Y_{nm}(\omega) = -nY_{nm}(\omega)$

amsmath

In Chapter 3 the pseudo-differential operator $\mathcal{L}_{3/2}$, see (3.36), was introduced. Some insight is provided into its definition and to the origin of the eigenvalue relation

$$\mathcal{L}_{3/2}Y_{nm}(\omega) = -nY_{nm}(\omega). \tag{B.1}$$

The origin of $\mathcal{L}_{3/2}$ is a scaling argument made on the integral scattering operator with Henyey-Greenstein phase function. Recall for $\xi = \omega \cdot \omega'$,

$$f(\xi) = \frac{\sigma_s(1-g^2)}{4\pi(1-2g\xi+g^2)^{3/2}} = \sigma_s \sum_{n=0}^{\infty} \frac{2n+1}{4\pi} g^n P_n(\xi). \tag{B.2}$$

In the context of § 3.3.3 we consider the above under the scaling $\epsilon = 1-g$ and $\sigma_s = \sigma/\epsilon$ in the limit of high optical thickness and forward scattering

$$\frac{1}{\sigma}\lim_{\epsilon\to 0} \frac{\sigma_s(1-g^2)}{4\pi(1-2g\xi+g^2)^{3/2}} = \frac{1}{\sigma}\lim_{\epsilon\to 0}\sigma_s \sum_{n=0}^{\infty} \frac{2n+1}{4\pi} g^n P_n(\xi). \tag{B.3}$$

For convenience, each side is considered separately. The lhs

$$\begin{aligned} \frac{1}{\sigma}\lim_{\epsilon\to 0} f(\xi) &= \frac{1}{\sigma}\lim_{\epsilon\to 0} \frac{\sigma_s(1-(1-\epsilon)^2)}{4\pi(1-2(1-\epsilon)\xi+(1-\epsilon)^2)^{3/2}} \\ &= \frac{1}{4\pi\sqrt{2}(1-\xi)^{3/2}}. \end{aligned} \tag{B.4}$$

The rhs

$$\frac{1}{\sigma}\lim_{\epsilon\to 0}\sigma_s \sum_{n=0}^{\infty} \frac{2n+1}{4\pi} g^n P_n(\xi) = \frac{1}{\sigma}\lim_{\epsilon\to 0}\sigma_s \sum_{n=0}^{\infty} \frac{2n+1}{4\pi}\Big(1-\epsilon n+\epsilon^2 n(n-1)+\mathcal{O}(\epsilon^2)\Big) P_n(\xi)$$

$$= \lim_{\epsilon\to 0}\frac{1}{\epsilon}\sum_{n=0}^{\infty}\frac{2n+1}{4\pi}P_n(\xi)+\sum_{n=0}^{\infty}\frac{2n+1}{4\pi}(-n)P_n(\xi) \quad \text{(B.5)}$$

$$= \lim_{\epsilon\to 0}\frac{1}{\epsilon}\delta(\xi-1)+\sum_{n=0}^{\infty}\frac{2n+1}{4\pi}(-n)P_n(\xi). \quad \text{(B.6)}$$

Putting these results together in the context of the integral scattering operator with Henyey-Greenstein phase function, $\mathcal{L}_{HG}$,

$$\begin{aligned}\frac{1}{\sigma}\lim_{\epsilon\to 0}\mathcal{L}_{HG}[Y_{nm}(\omega)] &= \lim_{\epsilon\to 0}\frac{1}{\epsilon}\int_{S^2}\delta(\omega\cdot\omega'-1)Y_{nm}(\omega')\mathrm{d}\omega' \\ &+ \sum_{n=0}^{\infty}(-n)\sum_{m=-n}^{m=n}Y_{nm}(\omega)\int_{S^2}Y^*_{nm}(\omega')Y_{nm}(\omega')\mathrm{d}\omega'. \quad \text{(B.7)}\end{aligned}$$

For this integral to exist, it must be interpreted as a principal value: one takes the limit as γ goes to zero of the integral over the unit sphere excluding the small disk $\gamma > \omega\cdot\omega'-1$. With this principal value interpretation, the above integral exists and the pseudo-differential operator is well defined by

$$\mathcal{L}_{3/2}[\psi(\omega)] = \frac{1}{4\pi\sqrt{2}}\int_{S^2}\frac{\psi(\omega')}{(1-\omega\cdot\omega')^{3/2}}\mathrm{d}\omega'. \quad \text{(B.8)}$$

Appendix C

`OneDrtePn.m`: A Matlab M-file Implementation of the P_N-method

The following M-file was used to determine solutions of the radiative transport equation for all of the scattering theories presented in chapter three. The code is organized as follows: `oneDrtePn.m` is the main program file with dependencies `amatrix.m`, `dmatrix.m`, `Gauss.m`, `legendre_associated.m`.

At the time of writing, the M-files `Gauss.m` and `legendre_associated.m` are available at the Mathworks website: `http://www.mathworks.com/matlabcentral/`.

```
function [BackRad, TransRad] = oneDrtePn(n,g,sigs,siga,L,modelNum)
%%%%%%%%%%%%%%%%%%%%%%%%%%%%%%%%%%%%%%%%%%%%%%%%%%%%%%%%%%%%%%%%
% Determines the solution of the one-dimensional RTE in slab geometry.
% Input:
% n = the number of polynomials in the Pn-method, must be even.
% g = anisotropy factor.
% sigs = scattering cross section.
% siga = absorption cross section.
% L = slab thickness.
% modelNum = 1 for RTE w/ HG, 2 for FP, 3 for MLL,
%                  4 for MLL2, 5 for FP+L3/2
% Output:
% BackRad = backscattered radiance at z = 0.
% TransRad = transmitted radiance at z = L.
%%%%%%%%%%%%%%%%%%%%%%%%%%%%%%%%%%%%%%%%%%%%%%%%%%%%%%%%%%%%%%%%
% Insure that an even number of Legendre polynomials are used
% so that the matrix 'A', in (4.22), isn't singular.
if ( mod(n,2)  = 0 )
     fprintf (1,'n has to be even!!!  ');
     error ('dmatrix - Fatal error!');
end
A = amatrix(n);
D = dmatrix(n,g,sigs,siga,modelNum);
H = -inv(A)*D;
[Evec,Evl] = eig(H);
```

```
% Construct V1, V2, V3, V4 matrices of (5.8)
% Quadrature points and weights
[mu, wt] = Gauss(n);
% Matrix representation of the Legendre polynomials.
for l=1:1:n % loop over order of Leg. poly.
     for imu = 1:1:n/2 % loop over quad. pts.
% Use abscissa from Gauss-Legendre quadrature
% mu > 0
     W1(l,imu) = (2*l-1)*legendre_associated (l-1,0,mu(imu+n/2))/4/pi;
% mu < 0
     W2(l,imu) = (2*l-1)*legendre_associated (l-1,0,mu(imu))/4/pi;
     end
end
% Select positive eigenvalues, put the associated eigenvectors in P1,P2
kpos = 1;
for i=1:n
     if Evl(i,i) > 0
     P1(:,kpos) = Evec(:,i)*exp(-Evl(i,i)*L); % z = 0
     P2(:,kpos) = Evec(:,i); % z = L
      kpos = kpos + 1;
     end
end
kpos = kpos - 1; % Number of positive eigenvalues
% Select negative eigenvalues, put the associated eigenvectors in N1,N2
kneg = 1;
for i=1:n
     if Evl(i,i) < 0
```

```
      N1(:,kpos) = Evec(:,i); % z = 0
      N2(:,kpos) = Evec(:,i)*exp(Evl(i,i)*L); % z = L
       kneg = kneg + 1;
      end
end
kneg = kneg - 1; % Number of negative eigenvalues
% Construct V1, V2, V3, V4 matrices of (5.8)
V1 = P1'*W1; % see, (5.9)
V2 = N1'*W1; % see, (5.10)
V3 = P2'*W2; % see, (5.11)
V4 = N2'*W2; % see, (5.12)
% Define the matrix V (5.8)
V = cat(1, cat(2,V1',V2'),cat(2,V3',V4'));
% Define angular boundary conditions
% mu > 0, z = 0
param = 1/sigs;
for imu = 1:n/2
      BCmuPos(imu) = exp(-(mu(imu+n/2)-1)^2/(param^2)/4)/param/sqrt(pi);
end
% mu < 0, z = L
BCmuNeg = zeros(1,n/2);
BC = cat(1,BCmuPos',BCmuNeg');
% coeff are the normal mode expansion coefficients
coeff = linsolve(V, BC);
% Define
for ii=1:kpos
      c(ii) = coeff(ii);
```

```
end
for ii=1:kneg
     d(ii) = coeff(ii+kpos);
end
% Construct the solutions
BackRad = a*(P1'*W2) + b*(N1'*W2); % z = 0, mu < 0
TransRad = a*(P2'*W1) + b*(N2'*W1); % z = L, mu > 0
```

```
function A = amatrix(n)
% Program to compute the 'A' matrix, (4.22)
for i = 1:n
        for j = 1:n
           if i == j + 1
              A(i,j) = j./(2*j+1);
           elseif j == i + 1
              A(i,j) = (i)./(2*i-1);
           else
              A(i,j) = 0;
           end
        end
end
```

```
function D = dmatrix(N,g,sigs,siga,modelNum)
for in = 1:N
     if modelNum == 1 % RTE w/ H.G.
        lambda = -sigs*(1-g.^(in-1));
     end
     if modelNum == 2 % FP
        lambda = -sigs*(1-g)*(in-1)*(in)/2;
     end
     if modelNum == 3 % Mod. L. L.
        beta = (1-g)/2/g;
        alpha = sigs*(1-g)/2/g;
        lambda = -alpha*in*(in-1)/(1+beta*in*(in-1));
     end
     if modelNum == 4 % Mod. L. L. 2
        beta = (1-g)/(2*(g-g^N));
        alpha = sigs*(1-g^N)*beta;
        lambda = -alpha*in*(in-1)/(1+beta*in*(in-1));
     end
     if modelNum == 5 % FP + L3/2
        lambda = -sigs*(in-1)*(1-g)*(2-g) + sigs*(1-g)^2*(in-1)*in/2;
     end
D(in,in) = siga - lambda;
end
```

Bibliography

[1] S. Arridge, Optical tomography in medical imaging, Inverse Problems, 15 (1999), pp. 41–93.

[2] S. Arridge, M. Schweiger, M. Hiraoka, and D. Delpy, A finite element approach for modelling photon transport in tissue, Med. Phys., 20(2) (1993), pp. 299–309.

[3] M. Asadzadeh and A. Kadim, Chebyshev spectral s_n method for the neutron transport equation, Comp. Math. with Appl., 52 (2006), pp. 509–524.

[4] E. Aydin, S. Katsimichas, and C. de Oliveira, Time-dependent diffusion and transport calculations using a finite-element-spherical harmonics method, JQSRT, 95 (2005), pp. 349–363.

[5] G. Bal, Transport through diffusive and non-diffusive regions, embedded objects, clear layers, SIAM J. Appl. Math., 62(5) (2002), pp. 1677–1697.

[6] G. Bal and Y. Maday, Coupling of transport and diffusion models in linear transport theory, M2AN Math. Model. Numer. Anal., 36 (2002), pp. 69–86.

[7] M. Benassi, R. Garcia, A. Karp, and C. Siewert, A higher-order spherical harmonics solution to the standard problem in radiative transfer, Astrophys. J., 280 (1984), pp. 853–864.

[8] C. Borgers and E. W. Larsen, The transversely integrated scalar flux of a narrowly focused particle beam, SIAM J. Appl. Math., 55 (1995), pp. 1–22.

[9] J. Boyd, Chebyshev and Fourier Spectral Methods, Dover, New York, 2001.

[10] S. Campbell, A. O'Connell, G. Rutherford, and R. Grobe, Impact of large-angle scattering on diffusively backscattered halos, Opt. Lett., 32(5) (2007), pp. 560–562.

[11] C. Canuto, M. Hussaini, A. Quarteroni, and T. Zang, Spectral Methods in Fluid Dynamics, Springer, New York, 1988.

[12] ——, Spectral Methods: Fundamentals in Single Domains, Springer, New York, 2006.

[13] ——, Spectral Methods. Evolution to Complex Domains and Applications to Fluid Dynamics, Springer, New York, 2007.

[14] K. M. Case and P. Zweifel, Linear Transport Theory, Addison-Wesley, Reading, Massachusetts, 1967.

[15] C. Cercignani, The Boltzmann Equations and Its Applications, Springer, New York, 1988.

[16] S. Chandrasekhar, Radiative Transfer, Dover, New York, 1960.

[17] W. F. Cheong, S. A. Prahl, and A. J. Welch, A review of the optical properties of biological tissues, IEEE J. Quantum Electron., 26 (1990), pp. 2166–2185.

[18] B. Das, F. Liu, and R. Alfano, Time-resolved fluorescence and photon migration studies in biomedical and model random media, Reports on Progress in Physics, 60(2) (1996), pp. 227–292.

[19] ——, Time-resolved fluorescence and photon migration studies in biomedical and model random media, Reports on Progress in Physics, 60(2) (1997), pp. 227–292.

[20] R. Dautray and J.-L. Lions, Mathematical Analysis and Numerical Methods for Science and Technology, Vol. 6, Springer-Verlag, Berlin, 1993.

[21] B. Davison, Neutron Transport Theory, Oxford University Press, London, 1957.

[22] L. C. Evans, Partial Differential Equations, American Math. Society, Providence, Rhode Island, 2002.

[23] R. Garcia, C. Siewert, and J. J.R. Thomas, The classical spherical-harmonics method in transport theory, Trans. Amer. Nucl. Soc., 71 (1994), pp. 212–213.

[24] S. Gayen and R. Alfano, Sensing lesions in tissues with light, Op. Exp., 4(11) (1999), pp. 475–480.

[25] G. Goertzel and N. Tralli, Some Mathematical Methods of Physics, McGraw-Hill, New York, 1960.

[26] D. J. Higham and N. J. Higham, The Matlab Guide, SIAM, Philadelphia, 2005.

[27] A. Ishimaru, Wave propagation and scattering in random media I,II, Academic, New York, 1978.

[28] S. Jacques, C. Alter, and S. Prahl, Angular dependence of hene laser light scattering by human dermis, Lasers in the Life Sciences, 1(4) (1987), pp. 309–334.

[29] J. Jeans, Mon. Not. Royal Aston. Soc., 78 (1917), p. 28.

[30] H. B. Keller, On the pointwise convergence of the discrete ordinates method, SIAM J. Appl. Math., 8(4) (1960), pp. 560–567.

[31] A. D. Kim, Backscattering by tissues near the source, unpublished, (2004).

[32] A. D. Kim and J. B. Keller, Light propagation in biological tissue, J. Opt. Soc. Am. A, 20 (2003), pp. 92–98.

[33] A. D. Kim and M. Moscoso, Chebyshev spectral method for radiative transfer, SIAM J. Sci. Comput., 23 (6) (2002), pp. 2074–2094.

[34] ——, Backscattering of beams by forward-peaked scattering media, Opt. Lett., 29 (2004), pp. 74–76.

[35] ——, Beam propagation in sharply peaked forward scattering media, J. Opt. Soc. Am. A, 21 (2004), pp. 797–803.

[36] E. Larsen and J. Keller, Asymptotic solution of neutron transport problems for small mean free paths, J. Math. Phys., 15 (1974), pp. 75–81.

[37] E. W. Larsen, The linear boltzmann equation in optically thick systems with forward-peaked scattering, Prog. Nucl. Energy, 34 (1999), pp. 413–423.

[38] C. L. Leakeas and E. W. Larsen, Generalized fokker-planck approximations of particle transport with forward-peaked scattering, Nuc. Sci. Eng., 137 (2001), pp. 236–250.

[39] E. Lewis and W. Miller, Computational Methods of Neutron Transport, John Wiley & Sons, New York, 1984.

[40] C. Meyer, Matrix Analysis and Applied Linear Algebra, SIAM, Philadelphia, 2001.

[41] C. Moler and C. V. Loan, Nineteen dubious ways to compute the exponential of a matrix, twenty five years later, SIAM Review, 45(1) (2003), pp. 3–43.

[42] J. Morel, An improved fokker-planck angular differencing scheme, Nucl. Sci. Eng., 89 (1985), pp. 131–136.

[43] A. W. Naylor and G. R. Sell, Linear Operator Theory in Engineering and Science, Springer-Verlag, New York, 1982.

[44] K. G. Phillips and C. Lancellotti, A universal numerical treatment of radiative transport equations with differential and integral scattering operators, in Biomedical Applications of Light Scattering II, A. Wax and V. Beckman, eds., vol. 6864 of Proceedings of SPIE, 2008, pp. ??–??

[45] K. G. Phillips, M.Xu, S. Gayen, and R. Alfano, Time-resolved ring structure of backscattered circularly polarized beams from forward scattering media, Op. Exp., 13 (2005), pp. 7954–7969.

[46] K. G. Phillips, M. Xu, S. Gayen, and R. Alfano, Time-resolved ring structure of backscattered circularly polarized beams from forward scattering layered structures, in Three-Dimensional and Multidimensional Microscopy: Image Acquisition and Processing XIII, T. W. Jose-Angel Conchello, Carol J. Cogswell, ed., vol. 6091 of Proceedings of SPIE, 2006, pp. 42–48.

[47] G. Pomraning, The fokker-planck equation as an asymptotic limit, Math. Models Meth. Appl. Sci., 2 (1992), pp. 21–36.

[48] ——, Higher order fokker-planck operators, Nucl. Sci. Eng., 124 (1996), pp. 390–397.

[49] ——, A non-gaussian treatment of radiation pencil beams, Nucl. Sci. Eng., 127 (1997), p. 182.

[50] K. Ren and G.Bal, Generalized diffusion model in optical tomography with clear layers, J. Opt. Soc. Am. A, 20(12) (2003), pp. 2355–2364.

[51] K. Rinzema, L. Murrer, and W. Star, Direct experimental verification of light transport theory in an optical phantom, J. Opt. Soc. Am. A, 15 (1998), pp. 2078–2088.

[52] H. Risken and T. Frank, The Fokker Planck Equation Method of Solution and Applications, 2nd Ed., Springer-Verlag, New York, 1996.

[53] L. Ryzhik, G. Papanicolaou, and J. Keller, Transport equations for elastic and other waves in random media, Wave Motion, 24 (1996), pp. 327–370.

[54] A. Schuster, Radiation through a foggy atmosphere, Astrophys. J., 21 (1905), pp. 1–23.

[55] C. Siewert, The f_n method for solving radiative transfer problems in plane geometry, Astrophysics and Space Science, 58 (1978), pp. 131–137.

[56] H. Spohn, Derivation of the transport equation for electrons moving through random impurities, J. Stat. Phys., 17 (1977), pp. 385–412.

[57] L. Trefethen, Finite Difference and Spectral Methods for Ordianry and Partial Differential Equations, unpublished text, http://web.comlab.ox.ac.uk/oucl/work/nick.trefethen/pdetext.html, 1996.

[58] A. Welch and M. van Gemert, Optical-Thermal Response of Laser-Irradiated Tissue, Plenum Press, New York, 1995.

[59] G. Wick, Zs. f. Physik, 120 (1943), p. 702.

[60] M. Xu, Electric field monte carlo simulation of polarized light propagation in turbid media, Opt. Exp., 12 (2004), pp. 6530–6539.

[61] K. Yoo, F. Liu, and R. Alfano, When does the diffusion approximation fail to describe photon transport in random media?, Phys. Rev. Lett., 64 (1990), pp. 2647–2650.